

Probing nucleosome arrays
with magnetic tweezers force spectroscopy and AFM imaging

Dissertation der Fakultät für Biologie
der Ludwig-Maximilians-Universität München

Yi-Yun Lin
Utrecht, 2024

Diese Dissertation wurde angefertigt unter der Leitung von
Prof. Dr. Jan Lipfert im Bereich von Fakultät für Physik an der
Ludwig-Maximilians-Universität München

Erstgutachter: Prof. Dr. Thorben Cordes

Zweitgutachter: Prof. Dr. Jan Lipfert

Tag der Abgabe: 25.06.2024

Tag der mündlichen Prüfung: 26.11.2024

Eidesstattliche Erklärung

Ich versichere hiermit an Eides statt, dass die vorgelegte Dissertation von mir selbständig und ohne unerlaubte Hilfe angefertigt ist.

I declare that I have authored this thesis independently and that I have not used other than the declared sources.

Utrecht, den 10.06.2024 Yi-Yun Lin

Erklärung

Hiermit erkläre Ich, dass ich zuvor nicht versucht habe, anderweitig eine Dissertation einzureichen oder mich einer Doktorprüfung zu unterziehen. Die vorliegende Dissertation wurde keiner weiteren Prüfungskommission weder in Teilen noch als Ganzes vorgelegt.

I declare that I have not submitted or defended a dissertation previously without success. The present dissertation has not been presented to another examination board, neither entirely nor in parts.

Utrecht, den 10.06.2024 Yi-Yun Lin

Table of Contents

Abstract	6
Abbreviation	8
1. Introduction	10
1.1 DNA structure	11
1.1.1 The characteristic of the DNA double helix	11
1.1.2 High-order structure: DNA topology	12
1.2 Nucleosome structure	14
1.2.1 Nucleosome assembly	17
1.2.2 Nucleosome dynamic	17
1.3 From nucleosome to chromatin	18
1.3.1 Regulation of higher order chromatin structures: 10 and 30 nm fibers	20
1.3.2 Co-factors and modifications can influence chromatin structure	20
1.4 Single molecule force spectroscopy for studying chromatin	22
1.5 Introduction for MT	25
1.5.1 Mechanical properties of a stretched and supercoiled DNA	26
1.5.2 Attachment of DNA to the surface	27
1.6 Outline of this thesis	29
2. Results	31
2.1 The calibration of magnetic tweezers	31
2.2 High-yield, ligation-free assembly of DNA constructs with nucleosome positioning sequence repeats for single molecule manipulation assays	32
2.2.1 Generation of labeled megaprimer constructs by PCR	32
2.2.2 Megaprimer PCR reaction to generate labeled DNA constructs for single-molecule measurements	32
2.2.3 Force response of megaprimer DNA constructs in magnetic tweezers	35
2.2.4 Torsional response of megaprimer DNA constructs in magnetic tweezers	37
2.2.5 Estimation of labeling efficiency from magnetic tweezers rupture time traces	37
2.3 Epigenetic histone modifications H3K36me3 and H4K5/8/12/16ac induce open polynucleosome conformations via different mechanisms	39
2.3.1 Magnetic tweezers force spectroscopy probes unmodified, H4K5/8/12/16ac, and H3K36me3 tri-nucleosome constructs	39
2.3.2 Repeated stretching and release cycles indicate that mechanical forces disrupt some but not all nucleosome interactions	41
2.3.3 Force spectroscopy suggests a reduction of stacking and outer turn wrapping interactions in H4K5/8/12/16ac and H3K36me3 compared to unmodified nucleosomes	42
2.3.4 Force spectroscopy finds no influence of the investigated PTMs on inner turn unwrapping of nucleosomes	44
2.3.5 Assembly and AFM imaging of tri-nucleosome arrays	45
2.3.6 AFM imaging reveals conformational changes of tri-nucleosome arrays induced by epigenetic modifications	48
2.3.7 Effect of the ion atmosphere on tri-nucleosome conformations	52

3.	Material and Methods	54
3.1	DNA constructs preparations	54
3.2	Magnetic tweezers setup	56
3.3	Flow cell preparation for magnetic tweezers force spectroscopy calibration	56
3.4	Measurement of drift correction and Allan deviation	57
3.5	20.6 kbp DNA measurement preparation	58
3.6	Magnetic tweezers force calibration	58
3.7	Nucleosome reconstitution	59
3.8	DNA or polynucleosome anchoring for magnetic tweezers experiments	60
3.9	AFM sample preparation, imaging, and analysis	60
3.10	Model for the step size distributions	61
4.	Discussion	63
5.	Supporting Information	67
5.1.1	Force calibration for magnetic tweezers	67
5.1.2	Spatiotemporal resolution by Allan deviation computing.....	67
5.1.3	Force calibration results	69
6.	Bibliography	85
	List of publications	99
	Acknowledgements	100
	Curriculum Vitae	101

Abstract

Nucleosomes are the fundamental unit of chromatin. They control eukaryotic genome accessibility and can regulate expression, replication, and repair of the genome by organizing chromatin. Canonical nucleosome core particles consist of two copies each of four histone proteins H2A, H2B, H3, and H4. The histone proteins are assembled into an octamer wrapped by ~147 base pairs (bp) of DNA. Nucleosomes interact with each other to form a higher-order structure – chromatin. Post-translational modifications (PTMs), which are epigenetic marks, play an important role in regulating chromatin accessibility. Recently, several studies have employed single-molecule force spectroscopy to unravel chromatin folding. Magnetic tweezers are a powerful tool to characterize biological macromolecules and their complexes both structurally and dynamically. The technique can measure the mechanical properties in terms of extension, elastic properties, and torque by manipulating several molecules in parallel with (sub-)piconewton (pN) force sensitivity and (sub-)nanometer spatial resolution. However, reliable single-molecule manipulation measurements require specific and stable attachment chemistries to tether the molecules of interest. Here, I present a functionalization strategy for DNA that enables high-yield production of constructs for torsionally constrained and very stable attachment. The method is based on “megaprimers” to amplify DNA with multiple DBCO and biotin modifications, respectively, at the opposite ends of the DNA constructs. DBCO-based click chemistry for covalent attachment to the surface and biotin-streptavidin coupling to the bead yield DNA tethers that withstand high forces (lifetime = 70 ± 3 hours at 45 pN). My optimized protocol provides a high-yield of correctly assembled DNA constructs, which makes it suitable for subsequent *in vitro* reconstitution of nucleosomes on the DNA.

Many post-translational modifications alter nucleosome dynamics, nucleosome-nucleosome interactions, and ultimately chromatin structure and gene expression. Here, I utilize single-molecule techniques to investigate small arrays of nucleosomes with post-translational modifications. I compare unmodified nucleosomes to ones that are methylated at histone 3 on lysine 36 (H3K36me3) and constructs that are tetra-acetylated on histone 4 (H4K5/8/12/16ac). I reconstitute the three types of tri-nucleosome arrays and perform magnetic tweezers force spectroscopy. I find a reduction in DNA outer turn wrapping and nucleosome-nucleosome interactions for the modified nucleosomes, H3K36me3 and

H4K5/8/12/16ac nucleosomes. We also visualize them by high-throughput AFM image in the second set of experiments. We find that H3K36me3 and in particular H4K5/8/12/16ac nucleosomes adopt significantly more open and loose conformations than unmodified nucleosomes. The results suggest that for H3K36me3 the increased breathing and outer turn DNA unwrapping seen in mononucleosomes propagates to more open conformations in tri-nucleosome arrays. In contrast, H4K5/8/12/16ac mononucleosomes exhibit similar conformations as their unmodified counterparts, suggesting that the more open conformations seen for H4K5/8/12/16ac tri-nucleosomes are driven by reduced nucleosome-nucleosome interactions.

In summary, I mainly focus on the properties of variant nucleosome arrays by using AFM and MT. I successfully develop a new single-molecule manipulation assay to benefit the research of nucleoprotein complexes and I use the approach to obtain new findings about the effect of post-translational modifications on nucleosome arrays.

Abbreviation

DNA	Deoxyribonucleic acid
PTM	Post-translational modification
bp	base pair
pN	pico Newton
AFM	Atomic force microscopy
MT	Magnetic tweezers
A	Adenine
T	Thymine
C	Cytosine
G	Guanine
Lk	Linker number
Tw	Twist
Wr	Writhe
SC	Supercoil
NCP	Nucleosome core particle
SHL	Superhelical location
W601	Widom 601
SAXS	Small angle X-ray scattering
FRET	Förster resonance energy transfer
EM	Electron microscopy
STORM	Stochastic optical reconstruction microscopy
TAD	Topological associating domain
SMC	Structural maintenance of chromosomes
OT	Optical tweezers
NRL	Nucleosome Repeat Length
CCD	Charge-coupled device
L_p	Persistence length
WLC	Worm-like chain
L_c	contour length
LED	Light-Emitting Diode
dig	digoxigenin
PCR	Polymerase chain reaction
anti-dig	anti-digoxigenin
nN	nanoNewton
DBCO	Dibenzocyclooctyne
AD	Allan deviation
dNTP	Deoxynucleotide triphosphates (dNTP)
DMSO	Dimethylsulfoxide
RNA	Ribonucleic acid
R_g	Radius of gyration

Abbreviation

LUT	Look-up table
PBS	Phosphate-buffered saline
AV	Allan Variance
PSD	Power spectrum density
EDTA	Ethylenediaminetetraacetic acid
HEPES	4-(2-hydroxyethyl)-1-piperazineethanesulfonic acid
LLPS	Liquid-liquid phase separation

1. Introduction

The genomes of eukaryotic organisms are stored in a cell nucleus. Their genetic information is encoded in billions of DNA base pairs. It is estimated that each human cell contains about 2 meters of DNA. To accommodate the long DNA into a cell nucleus, which is typically 10 to 20 microns in diameter, DNA is packed into 23 chromosomes by proteins called histones and other associated proteins, and the resulting DNA-protein complex is called chromatin. Thus, as a result of histones folding DNA, chromatin is packed into a much smaller volume than DNA alone. The structure of chromatin has been extensively studied over the last decades and especially the development of single-molecule techniques provides high spatial and temporal resolution to explore the structural dynamics of nucleosomes and chromatin fibers. Yet, many features of nucleosome dynamics remain unknown or poorly understood.

This dissertation is focused on using single-molecule methods, in particular magnetic tweezers and atomic force microscopy to probe the conformations and interactions in (arrays of) nucleosomes. Magnetic tweezers provide useful information by exerting mechanical stress induced by force and monitoring the extension response. The first chapter of the thesis introduces the concepts and background of the main structural features of DNA, nucleosomes, and chromatin fibers. In addition, I introduce the theoretical background of the single molecule technique I applied to my research. Finally, I provide a brief overview of the following chapters.

1.1 DNA structure

DNA, or deoxyribonucleic acid, is a polymer that carries the genetic information in all cellular life. DNA is composed of simple monomeric units called nucleotides. Each nucleotide consists of a nucleobase with four different types adenine (A), guanine (G), cytosine (C), and thymine (T), a phosphate group, and a pentose sugar, furanose (Figure 1.1). The four different bases arrange the order of DNA to give rise to different genetic codes. In 1950, the Chargaff rule was published by Austrian-American biochemist, Erwin Chargaff [1]. The rule is a principle stating that in the DNA of any species, the amount of guanine equals the amount of cytosine, and adenine equals the amount of thymine. These rules apply to double-strand DNA. This finding turned out to be crucial to Watson and Click's model of DNA double helix.

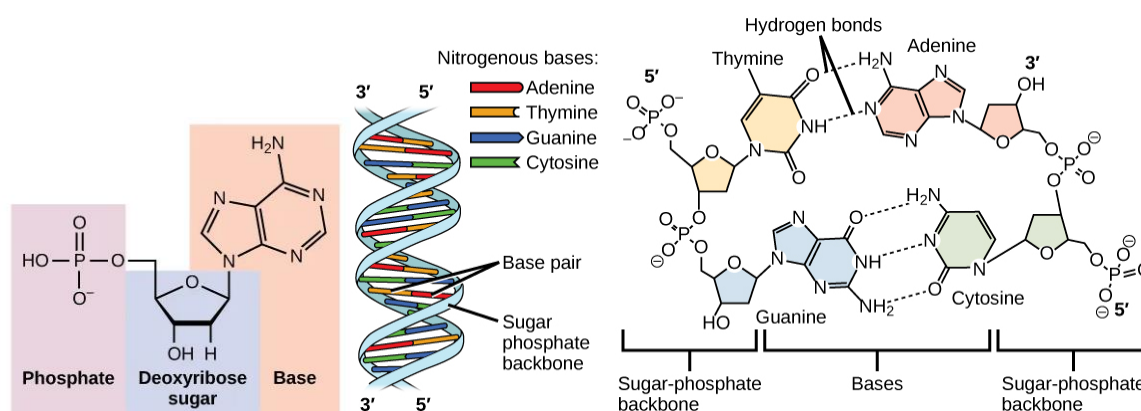


Figure 1.1: Monomeric unit of DNA structure. The basic unit of DNA is called a nucleotide, composed of phosphate (pink block), deoxyribose sugar (blue block), and base (Orange block). There are four different types of bases: cytosine, thymine, adenine, and guanine. Each phosphate group attached to 5' carbon is joined by a bond called phosphodiester linkage by attaching to the hydroxyl group at 3' end sugar of an incoming nucleotide to form the polymer structure: DNA. Adapt from OpenStax College, Biology, licensed under (CC BY 4.0).

1.1.1 The characteristic of the DNA double helix

In 1953, James Watson and Francis Click discovered the chemical structure of DNA and revealed the arrangement of the bases connecting pairs (A+T, C+G) that stack on each other to form the characteristic DNA double helix. The sugar-phosphate backbones of DNA shape the outside of the helix and the bases form hydrogen-bonded pairs that hold two DNA strands together. During that time, Maurice Wilkins and Rosalind Franklin from Kings College in

London succeeded in probing the DNA structure by X-ray crystallography, which gave Watson and Crick clues to the structure of DNA [2-4]. In 1962, Crick, Watson, and Wilkins received the Nobel Prize in Medicine. Unfortunately, Franklin died in 1958 and Nobel prizes are not awarded posthumously.

The findings revealed the structure of DNA as a double helix, with two strands antiparallelly to each other, which means that single strands intertwine each other in opposite directions. The 5' end (phosphate group) of nucleotides ligate to the 3' end (hydroxyl group) of the subsequent nucleotide via a phosphodiester bond to form 5'-3' orientation. The two strands twist around each other to form a right-handed helix. Alongside the helical structure, the bases create wider gaps (major groove) and narrow gaps (minor groove), which is important for protein binding to DNA (Figure 1.2).

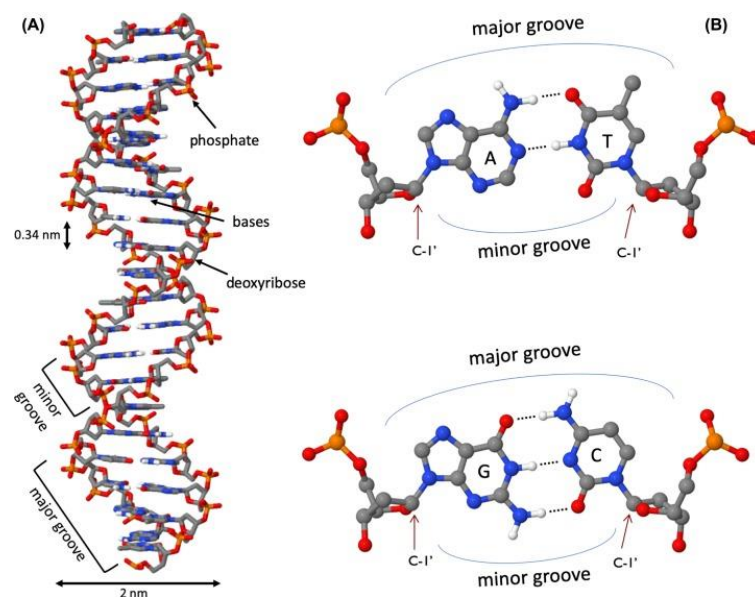


Figure 1.2: DNA structure. (A) DNA double helix structure, sugar phosphate backbone on the outside and nitrogenous bases inside. (B) A-T and C-G base pair, C1' of deoxyribose indicated by the arrow facing lower edge is minor groove and those facing upper edge of the base pair is major groove. Hydrogen bonds, indicated by the dotted line. Adapted from [5] and licensed under (CC BY 4.0).

1.1.2 High-order structure: DNA topology

In cellular life, DNA can adopt more complicated structures, in particular due to the strain exerted by multiple enzymes in the cell. Those enzyme machines perform “mechanical”

functions and change DNA topology to control cell behavior and development. DNA supercoiling is a higher-order DNA structure, where DNA strands are intertwined or linked together. DNA topological properties facilitate the regulation of DNA replication and transcription. The topology of DNA is characterized by the degree of supercoiling of DNA and it can be described by linking numbers [6, 7].

The linking number is an integer value to describe the number of times that two strands of DNA wind around each other. We can describe the linker number as the sum of twist and writhe. “Twist” refers to the number of times the single strands of DNA turn around the other. “Writhe” refers to the number of times of double-stranded DNA cross each other to present supercoil properties. These three parameters are related by [7]:

$$Lk = Tw + Wr$$

For relaxed and circular DNA, which means DNA with no torsional stress, the linking number is given by $Lk_0 = N/\gamma$, with N the number of base pairs and γ the number of base pairs per helical turn ($\gamma \approx 10.5$ base pairs for B-form DNA). DNA underwinding or overwinding induces torsional stress within the molecule and results in negative (-) or positive (+) supercoils (SC), respectively. One of the remarkable functions of DNA supercoiling is to package genetic material into cell or nucleus. In eukaryotic cells, double-stranded DNA is wrapped around histone octamers to form basic units of chromatin: nucleosomes. Supercoiling and wrapping of DNA around histones helps to compact linear genome (with a length of ~2 m for the human genome) into cell nucleus on a scale of micrometers. Nucleosomes can form a higher-order structure and assemble into chromatin.

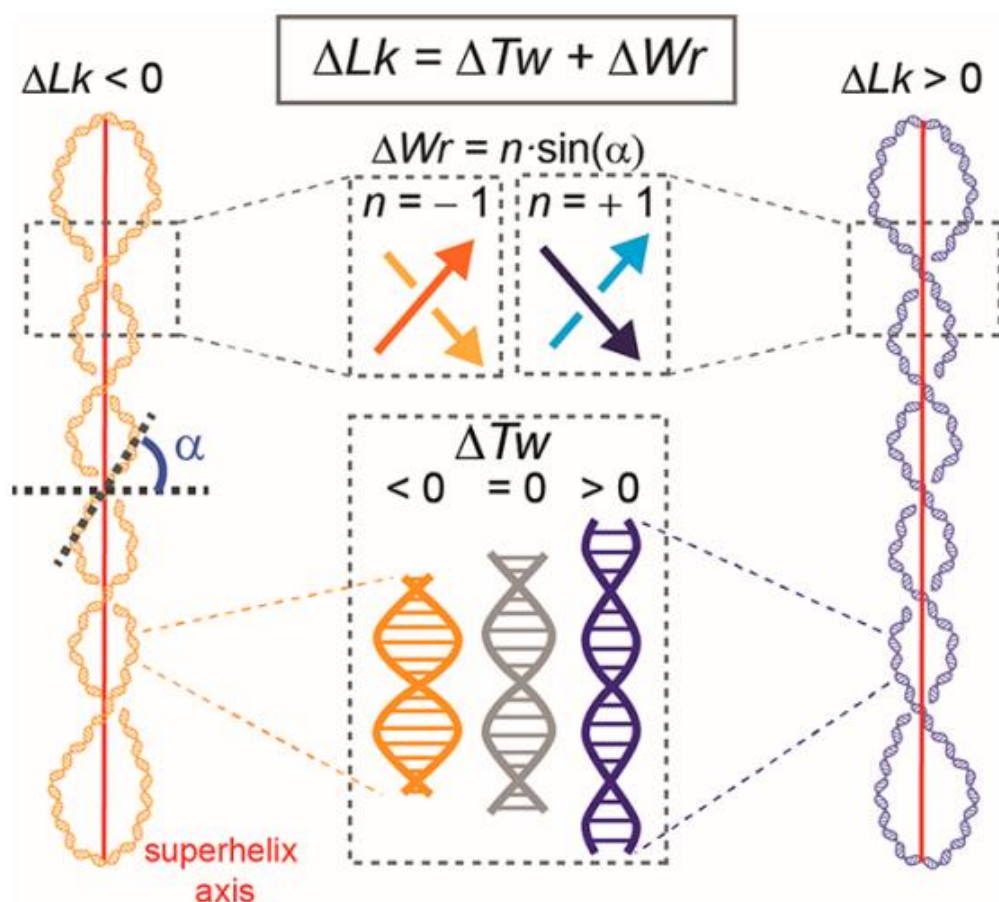


Figure 1.3: Supercoiling: its handedness and sign. The linking difference ΔLk is composed of twist ΔTw and writhe ΔWr . Local DNA unwinding by twisting DNA in the opposite direction to the nature helicity to form right-handed in supercoil (-) molecule ($\Delta Lk < 0$, plasmid on the left). Overwinding by twisting DNA to the nature helicity to form left-handed in supercoil (+) molecule ($\Delta Lk > 0$, plasmid on the right). Topological convention of sign assignment of perceived crossings. In a (-) crossing, with turning the overlying direction clockwise. In a (+) crossing, with turning the overlying direction in counterclockwise way. Reprinted with permission from [8] American Chemical Society.

1.2 Nucleosome structure

The fundamental units of chromatin are nucleosomes. In 1997, nucleosome core particle (NCP) structure was determined at atomic scale by X-ray crystallography with a resolution of 2.8 Å [9]. This structure showed that 146 bp DNA wrap 1.65 turns around core histones (Figure 1.4a). The core histones organize into an octameric scaffold. In 1991, a 3.1 Å crystal structure of histone octamer revealed that the core histones are the assembly of 4 types of histone proteins in pairs for each, H2A, H2B, H3, and H4 [10]. Each histone contains core

histone and N- and C- terminal extensions. Each core histone is composed of three α helices with two intervening loops [9-11]. H2A/H2B and H3/H4 form heterodimers and tetramers respectively (Figure 1.4b,c). These complexes assemble to form histone octamers. The octamer surface carries positive charges that electrostatically interact with negative charge of DNA's phosphate groups so that DNA wraps around histone octamer to form approximately 100 Å diameter nucleosome. In addition, histone tails contain strong net positive charge due to many arginine and lysine residues. H2A/H2B dimer surface features negative charges that are referred to as H2A/H2B acidic patch and the acidic patch has a shape of a narrow groove and it provides a common binding site for H4-tail and many nucleosome binding proteins.

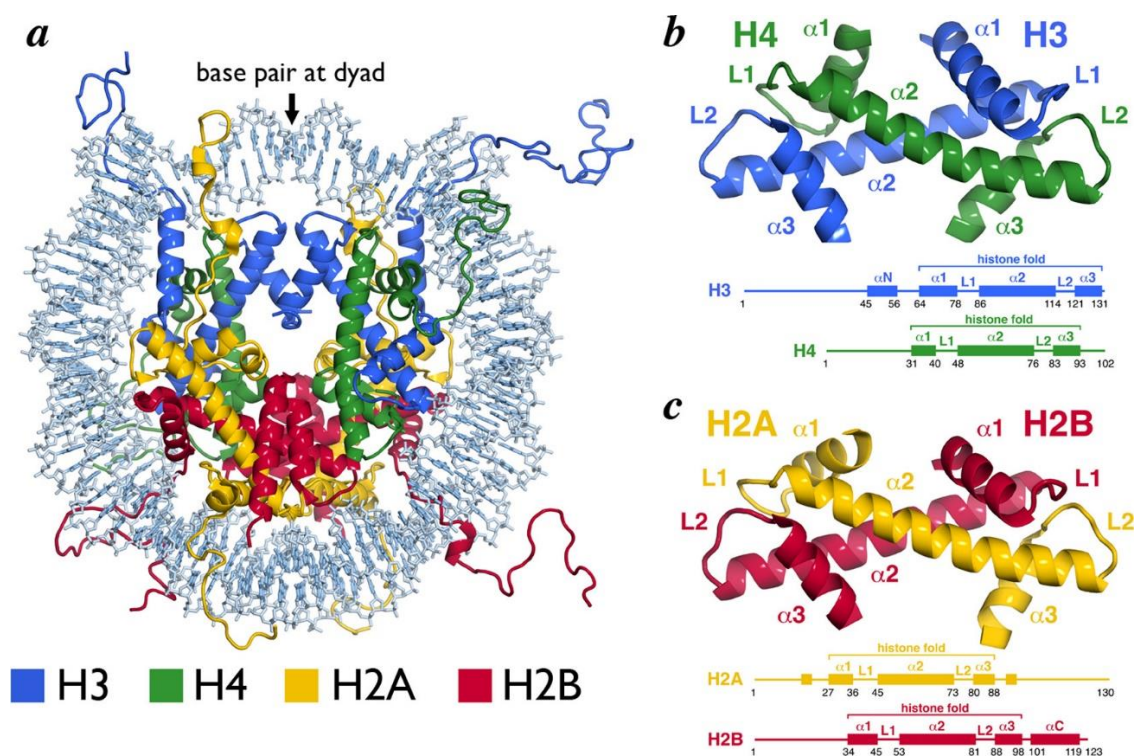


Figure 1.4: Nucleosome core particle structure and the histone-fold heterodimers. (a) Nucleosome core particle structure (PDB ID 1KX5). (b) H3/H4 histone-fold heterodimer. (c) H2A/H2B histone-fold heterodimer. Structures (top) and schemes (bottom) with secondary structure elements indicated. Reprinted with permission from [12] Copyright © 2014 American Chemical Society (ACS).

To describe DNA locations in the nucleosome, we describe DNA positions around the nucleosome with respect to the position of the dyad (Figure 1.5). DNA wraps around histone proteins in a left-handed superhelix. The superhelical locations (SHL) are used to describe DNA positions of superhelical turns from dyad (SHL 0), which is the middle of DNA fragment. Along the outer wrap of DNA on the nucleosome to the inner wrap of DNA, SHL

ranges from -7 to $+7$. The predominant contacts between DNA and histone octamer are located around $\pm x.5$ locations of SHL ($\pm 0.5, \pm 1.5, \dots$) where the minor grooves of DNA face octamer. For biophysical or structural studies of nucleosomes, frequently DNA sequences are used that are known to position nucleosomes: mixed sequence genomic DNA [13, 14], human α -satellite repeats [9, 15], 5s RNA coding sequence [16], and Widom 601 nucleosome positioning sequence [17, 18]. Widom 601 is the most popular DNA positioning sequence in chromatin biochemical studies. Lowary and Widom isolate synthetic random DNA sequences with high affinity for the histone octamer and called the highest affinity DNA sequence Widom 601 [17]. Widom 601 (W601) is the tightest binding sequence and results in high yield of nucleosomes in reconstitution experiments. W601 sequence has TA base steps with a 10 bp sequence periodicity (at SHL $-0.5, \pm 1.5, -2.5, -3.5$). The locations of TA make the minor groove face the histone octamer and have minimal base stacking so that W601 is flexible and can easily accommodate the distortion stress in the DNA upon assembling in the nucleosome [18, 19].

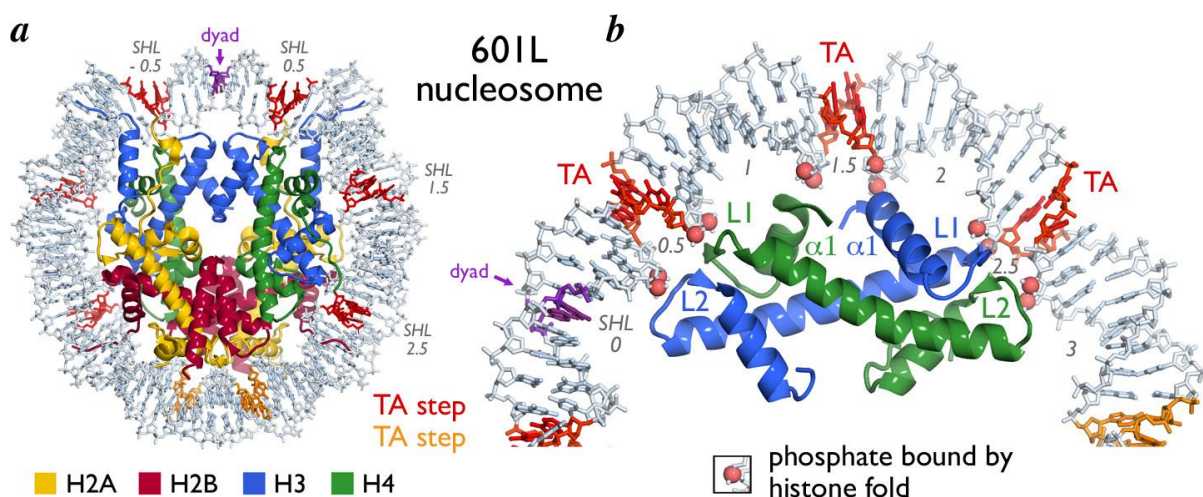


Figure 1.5: SHL describing location of TA steps in 601L nucleosome core particle structure. (a) The DNA superhelical axis in 601L NCP structure with TA steps interacting with histones. 601L is Widom 601 with symmetric sequence of TA steps at SHL $\pm 0.5, \pm 1.5, \pm 2.5, \pm 3.5$ [19]. The dyad is indicated (purple). (b) Zoom in one H3/H4 heterodimer bound to DNA containing three TA steps. Backbone phosphates of DNA bound to the H3/H4 histone folds. Reprinted with permission from [12] Copyright © 2014 American Chemical Society (ACS).

1.2.1 Nucleosome assembly

Nucleosome assembly involves the depositions of $(H3-H4)_2$ tetramers onto DNA and then followed by the addition of H2A-H2B heterodimers and DNA wrapping [20]. DNA is stably packed on histones by electrostatic interactions and hydrogen bonds between DNA and histone octamer [9]. Therefore, the reconstitution of nucleosomes is electrostatically driven and sensitive to the concentration and type of mono- and divalent cations [21]. Previous research on NaCl-induced disassembly pathway for NCP containing the 601-DNA by SAXS and FRET show that (Figure 1.6), at physiological ionic strength, NCP adopts an open intermediate configuration with unwrapping and rewrapping on a millisecond time scale [22]. Above 0.5 M NaCl, H2A-H2B dimers begin to dissociate to form hexasomes and tetrasomes. Above 1.2 M NaCl, $(H3-H4)_2$ tetramers begin to dissociate and cause the complete disassembly of NCP [22].

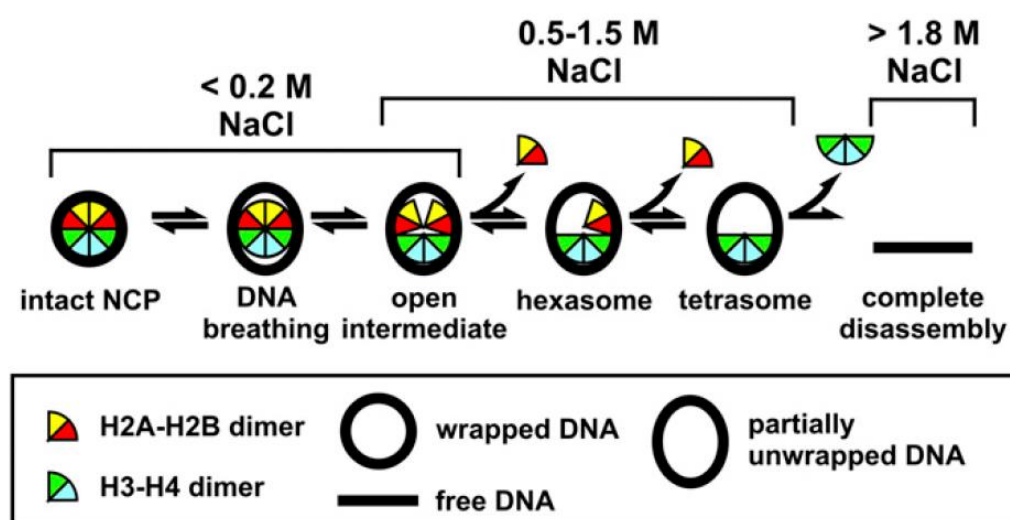


Figure 1.6: A schematic of NaCl-dependent disassembly for NCPs containing the 601-DNA. At physiological ionic strength, NCP configure local dynamics as DNA breathing and even form an open intermediate structure. As $[NaCl] \geq 0.5$ M, H2A-H2B dimers begin to dissociate to form a hexasome and texasome. As $[NaCl] \geq 1.4$ M, $(H3-H4)_2$ tetramers begin to dissociate to cause the complete disassembly. Adapted from [22] PNAS December 27, 2016 114 (2) 334-339 under CC by PDM 1.0 DEED.

1.2.2 Nucleosome dynamic

The nucleosome structural dynamics has been extensively studied. A previous study had presented a detailed map of histone-DNA interactions along the DNA sequence to near base pair accuracy by using a high-resolution force-induced unwrapping [23]. The results reveal

that the strength of histone-DNA interactions is not the same for each position (Figure 1.7). Nucleosomes make strong interactions at ± 40 bp upstream and downstream of the dyad and nucleosome dyad. The location near the DNA entry/exit region of nucleosome is the weakest location of histone-DNA interaction. In addition, the unwrapping events occur in a ~ 5 bp periodicity, which is in agreement with the DNA major/minor groove periodicity [24].

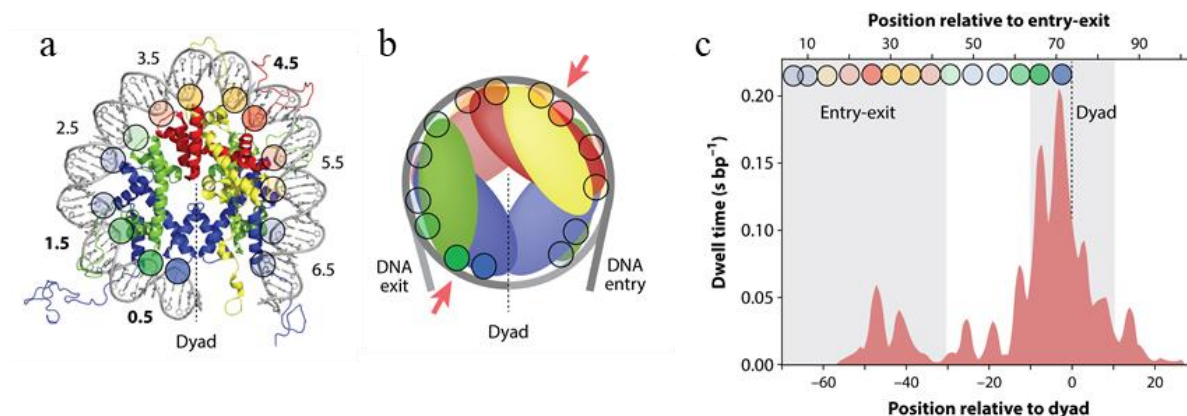


Figure 1.7: Nucleosome structural dynamics. (a) The nucleosome crystal structure with one half of the DNA, (H3-H4)₂ tetramer, and one of the H2A-H2B dimers. The colorful circles indicate locations of DNA-histone interactions. The numbers indicate the SHL. (c) The dwell time of DNA unwrapping as reported by Reference [23]. Reprinted with permission from [25]. Copyright by Annual Reviews.

1.3 From nucleosome to chromatin

The N-terminal tail domains of each histone protein that protrude from the nucleosome are disordered and highly positively charged. The tails can be extensively posttranslationally modified and cause conformational changes of nucleosome [26]. The tails interact with nucleosomal DNA to influence the stability of nucleosome and accessibility. Within chromatin, those tails further interact with adjacent nucleosomes to form higher-order structures [27, 28]. However, the exact organization of nucleosomes into compact chromatin is controversial, in part due to the structural complexity [29]. Nucleosomes connected by about 20-90 bp of linker DNA *in vivo* [30], which is the length between neighboring nucleosomes, form a 10-nm “beads on a string” array. The orientation between two adjacent nucleosomes depends strongly on the length of DNA linker. The shorter the DNA linkers, the more constrained the internucleosomal flexibility. In the earlier reports related to the structure of higher-order organization of chromatin, line arrays of nucleosomes form solenoidal filament, which look like a supercoiled fiber [31-34]. This structure adopts a hand-to-hand orientation by the consecutive nucleosomes, which means nucleosome-stacking interactions

occur between nearest neighbor nucleosome (Figure 1.8). Another alternative configuration of stacked nucleosomes is the zig-zag geometry. The architecture of this zig-zag structure is referred to as two-start folding of nucleosome arrays. In this model, the helix stacks with nucleosomes across from one another (Figure 1.8) [35, 36]. Moreover, due to helical twist of DNA, every bp of linker DNA changes the relative orientation between two nucleosome by 36° . Therefore, DNA linker length corresponding to $10n$ bp has a preference for the linker to retain the same orientation. When DNA linker length corresponds to $10n+5$ bp, the orientation turns 180° [37-39]. Besides, ionic environment and histone tails also regulate chromatin structure. In the presence of divalent ions, the shielding of negative charge allows for favorable inter-nucleosome interaction as well. It is shown that, the higher the Mg^{2+} concentration, the more compact the chromatin structure [31, 40, 41]. Histone tails can interact with neighbor nucleosome or recruit other proteins. Histone tails are flexible chains at the terminal domains of histones. Histone tails are positive charged and protrude from the nucleosome. The acidic patch can bind the N-terminal H4 tail of the nucleosome to form higher-order nucleosome structures [28]. The tails also feature wide range of post-translational modifications (PTM) [26]. Those could change the interaction between tails and acidic patch and further influence the staking of nucleosomes.

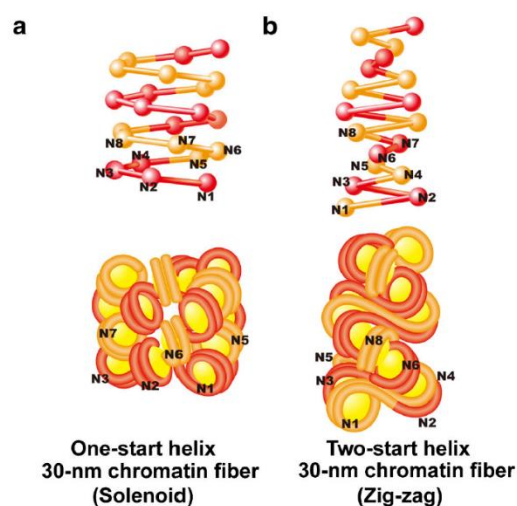


Figure 1.8: The schematics of two classic models of 30-nm chromatin fibers. The one-start helix (A, solenoid) and two-start helix (B, zigzag) [42]. Positions from the first (N1) to eight (N8) nucleosome are labeled. In the one-start helix, the 30-nm chromatin exhibited interdigitated solenoid, that nucleosome interact neighbors. In the two-start model proposed by Schalch et al [35]. A nucleosome in the fiber binds to second-neighbor nucleosome. (Red and orange). Adapt from [40] licensed under (CC BY).

1.3.1 Regulation of higher order chromatin structures: 10 and 30 nm fibers

From early electron microscopy (EM), the purified 10-nm fiber with linker histone H1 can easily form a regular fiber with 30-nm diameter, which is known as '30-nm' chromatin fiber. Since then, 30-nm fiber has been assumed to be the basic structural unit of chromatin [42, 43]. However, several *in vivo* studies show evidence that chromatin structure is not regular [44, 45]. Chromatin in cells can be observed directly by cryo-electron microscopy (EM). The data show that 30-nm chromatin fibres were not recognized in cell, but highly dispersed 10-nm mesh fibers in pluripotent mouse cells [46]. Super-resolution imaging (STORM) found that irregular groups of nucleosome clutches form chromatin conformations [47]. Taken together, the evidence suggests that the chromatin structure in cells has distinct features from the structure found *in vitro*. Nucleosome arrays, for example in the beads on a string model with 10-nm width fiber, form the core of genomic chromatin [48, 49]. The classical view is that 10 nm fibers further organize into 30 nm fiber. 30-nm chromatin fiber fold into hierarchical helical folding to form a highly compact structure [31, 44, 50]. However, research within recent decades found that 30 nm fibers remain absent from interphase nucleic [45, 51, 52]. In addition current views reveal that native chromatin formed as variable nucleosome arrangements without regular fiber structure [40, 53, 54]. Regular 30 nm fibers were found in the presence of low cation conditions since nucleosomal fibers repel each other gently due to insufficient screening of negative charges [31-33, 35, 42, 53, 55-57]. Therefore, nucleosome selectively bind to close neighbor nucleosome to form 30 nm fibers. However, the physiological ion condition has higher cation concentrations, which weaken the electrostatic repulsion between adjacent nucleosomes, to force the fibers form large condensates lacking the 30 nm structure [53, 56, 57].

1.3.2 Co-factors and modifications can influence chromatin structure

Different PTMs, nucleosome variants, and non-histone proteins binding in native chromatin are also the factors to change the arrangement of chromatin fiber at different levels (Figure 1.9). For instance, (1) PTMs at nucleosome tails affect the compaction of nucleosomes in chromatin fiber [26, 58, 59]. PTMs often modulate electrostatic or structural properties to change the interaction between histones and DNA. One of the typical PTMs is adding marks on lysine residues by acetylation, methylation, succinylation, and so on. PTMs can also provide signal which then are recognized by associated proteins, to initiate downstream signaling cascade and turn on or off the gene expression. (2) Cohesin mediates loop extrusion

so that chromatin regions form loops [60]. Hi-C, a genomic technique used to map the contact frequency of random two DNA fragments, shows that within chromatin, some regions has higher contact frequency [61]. Those regions as enriched introchromosomal contacts are organized into Topological Associating Domains (TADs) [62]. Both chromatin loops and TADs depend on the SMC complex cohesion to reel flanking regions of a DNA into a loop. Also, (3) the formation of compartments: Euchromatin, a loose structure; facultative heterochromatin, reversibly silenced gene regions; and constitutive heterochromatin, never transcribed chromatin region, segregate radially in nucleus [61, 63]. The compartmentalization exhibits contacts both within and between chromosomes [61]. It shows that active and inactive chromatin separate spatially in the nucleus [64]. (4) Nuclear bodies formation driven by liquid-liquid phase separation [65]. (5) Chromosome territories: chromosomes take separate, nonoverlapping positions in nucleus [66]. It is found that transcriptionally active chromosomes prefer to occupy nuclear center while inactive chromosomes locate at more peripheral in mammalian cells [67, 68].

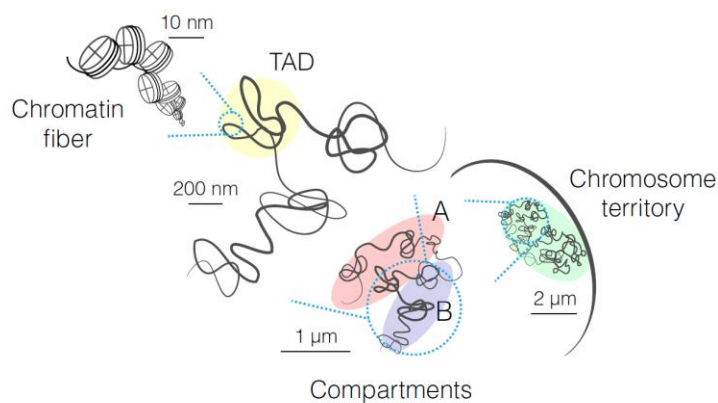


Figure 1.9: Schematic view of chromosome folding inside nucleus. DNA-histone assembly form nucleosomes into ~11-nm chromatin fiber. The compaction density is variable at different region depending on gene regulation. Chromatin folds at submegabase scale into higher-order domains referred to as TADs. At the chromosomal scale, chromatin is segregated into compartment A and B, indicating active gene region and repressed gene region irrespectively. Furthermore, individual chromosomes occupy their own space without overlapping to form chromosome territories. Adapted from [69] licensed under (CC BY 4.0).

Post-translational modification as a factor to regulate chromatin dynamics

Epigenetic modifications, or post-translational modifications (PTMs), a diverse array of covalent chemical marks that modulate gene expression without altering the DNA sequence, have emerged as critical regulators of chromatin architecture and function [70-74]. In eukaryotic cells, histones are subject to hundreds of PTMs including acetylation, methylation,

ubiquitination, phosphorylation, and sumoylation [75]. Histones PTMs are widely distributed throughout the whole genome. They can control the accessibility of DNA or recruit chromatin remodelers to regulate gene expression [58, 70-74, 76, 77]. Histone PTMs are present both in the tails of histones and their globular core domains [26, 59]. By introducing additional charge, neutralizing existing charge, or by adding steric constraints, different modifications affect the compaction of chromatin and also modulate the stability of nucleosomes. In particular, methylation and acetylation have been intensively studied as marks of chromatin status involving active or silenced transcription [73, 75]. For acetylation (“ac”), histone acetylation neutralizes the positive charge of lysine, which reduces interactions with DNA and has been shown to e.g., enable transcription factor binding within nucleosomes [78-80]. Acetylation of H4 tail has a strong effect on weakening chromatin packing *in vivo* and *in vitro* [78, 81-83]. H3 acetylation also reduces the charge of the tails but the effect on folding propensity of nucleosome arrays is less clear [80, 84].

Histone methylation (“me”) occurs on the side chains of lysines or arginines [85] and, unlike acetylation, does not alter the charge of histone protein and is thought to act mainly via “reader” enzymes that specifically recognize the methylated site and then activate or repress transcription [86]. For example, H3K9 and H3K27 methylation are often related to silenced chromatin states [86]. Examples of chromatin readers that recognize methylation and are involved in gene repression are HP1 that binds to H3K9me3 and contributes to heterochromatin formation [87, 88] and the methyltransferase PRC2 that acts on H3K27 [89] and recruits other accessory protein to propagate the H3K27me3 mark resulting in gene silencing [90-92]. In contrast, H3K36 methylation is associated with actively transcribed regions [93, 94].

1.4 Single molecule force spectroscopy for studying chromatin

Single molecule force spectroscopy techniques such as optical tweezers (OT), magnetic tweezers (MT), or atomic force microscopy (AFM) can be used to manipulate individual nucleosome, nucleosome assemblies, or chromatin fibers with piconewton (pN) force sensitivity and nanometer resolution (Figure 1.10). Force spectroscopy can be used to directly measure nanomechanical properties in terms of extensions, elastic properties, and force and torque dependence. In OT, polystyrene beads are trapped by laser beams to generate force. In MT, forces are exerted by magnetic fields and act on a paramagnetic beads tethered to

biomolecules. In AFM, a cantilever stretches biomolecule samples attached between the surface and the cantilever tip [95, 96].

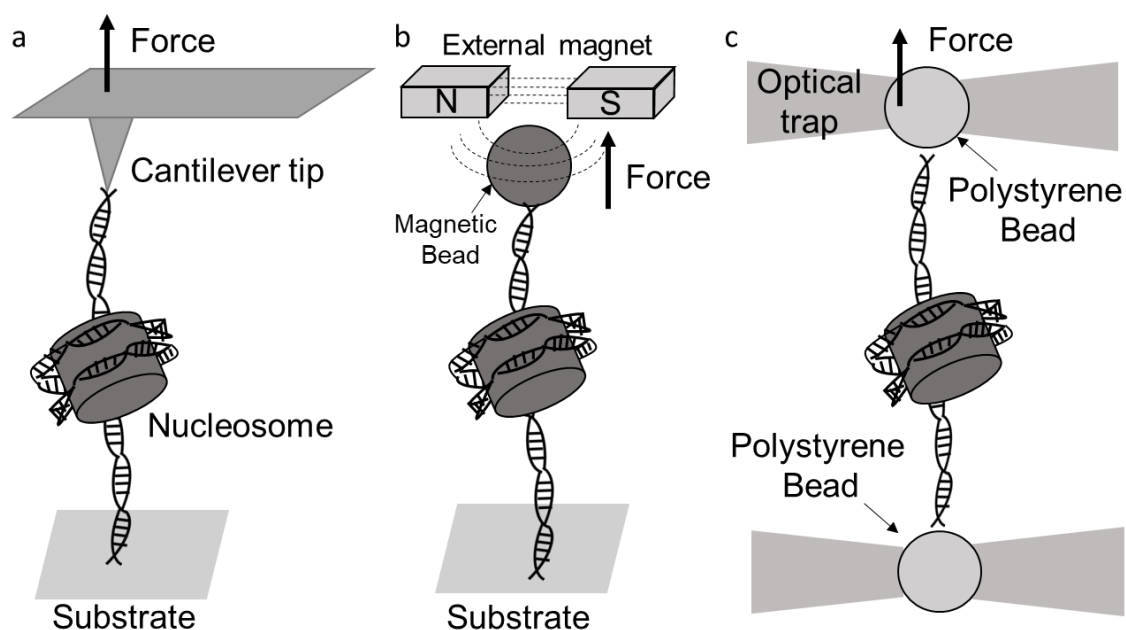


Figure 1.10: Schematic representation of atomic force microscopy, magnetic tweezers, and optical tweezers. (a) In atomic force microscopy, flexible cantilevers apply direct forces to a mononucleosome with the movement of the substrate controlled by a piezoelectric device. (b) In magnetic tweezers, forces are applied by a magnetic field to pull mononucleosome tethered to a magnetic bead. (c) In optical tweezers, beads binding to two ends of mononucleosome are trapped in focused laser beams.

The stretching behavior of mononucleosome –studied using OT– reveals 2 separate stages of DNA unwrapping from the histone octamer [97]. In 50 mM Kac and 10 mM Mg^{2+} , the first reversible transition, occurring around 3 pN with a step size length of 21 nm, is referred to as outer turn DNA unwrapping. The next second rupture step with size of 22 nm at force above ~8-9 pN refers to the inner turn DNA unwrapping and the second unwrapping step is irreversible. Wang and colleagues design an alternative force spectroscopy approach to unpeel DNA from one side of nucleosome by unzipping the DNA double-strand in single-base pairs steps so that nucleosome is in a highly controlled fashion [23]. The results show that the longest dwell times are around 30 to 40 bp and 70 to 80 bp into nucleosome, which refer to the strongest DNA-histone interactions. Single-molecule force spectroscopy also provides a method to determine the strength of internucleosomes stacking in chromatin fibers. Cui & Bustamante used optical tweezers to stretch single chromatin fibers extracted from chicken erythrocytes and found a distinctive condensation-decondensation transition

that appears between 5 and 6 pN [98]. Similar results from magnetic tweezers by pulling reconstituted chromatin determined that nucleosome stacking is disrupted at around 4 pN pulling force [99]. The transition to a large extension of chromatin from force-extension curves in the low force at ~ 3 pN is localized at the force regime for DNA unwrapping as observed in mononucleosomes [97, 100]. Meng *et al.* aimed to disentangle unfolding transitions in chromatin fibers by using a magnetic tweezers and build a quantitative model for all aspects of unwrapping of a chromatin fiber [101, 102]. They showed that the pulling force for the unstacking of chromatin fiber co-exists with the unwrapping of the outer turn of a single nucleosome between 3 and 7 pN. In addition, chromatin fibers with 20- and 50-bp linker DNA demonstrate different folding topologies [103]. Chromatin with 197 bp Nucleosome repeat length (NRL) fibers closely follows independent transitions for all rupture events, which shows that nucleosome interactions form between neighbors. For chromatin arrays with 20 bp linker DNA, the crystal structure of tetranucleosomes shows interactions between non-neighboring nucleosomes and form zig-zag folding. Therefore, experimental data feature two times smaller extension, higher stiffness and less independence of rupture events compared to chromatin array with 50 bp linker DNA (197 bp NRL).

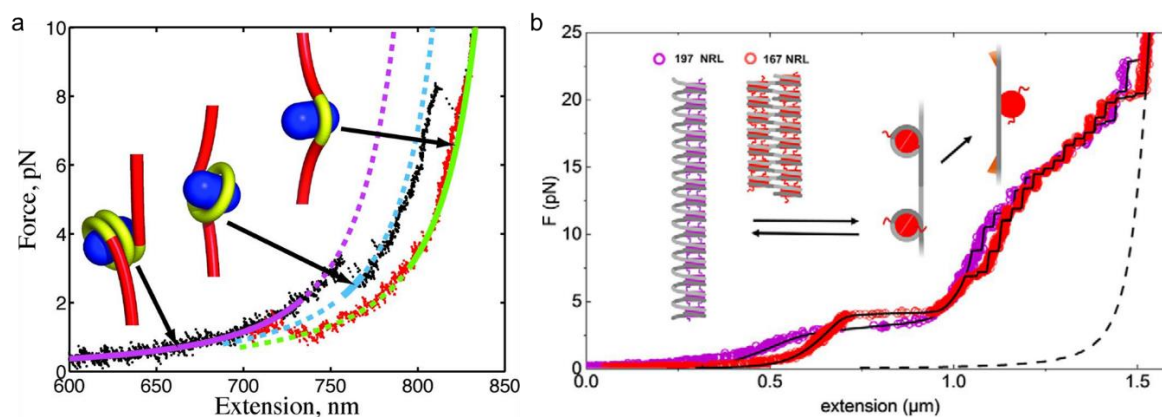


Figure 1.11: Force-induced mononucleosome and chromatin disruption. (a) The force-extension curve (F-D curve) shows two distinct steps referring to DNA unwrapping. 878 nm DNA construct with one W601 sequence to reconstitute to mononucleosome with octamer histones. Adapted from [97] Copyright © 2006 by The National Academy of Sciences of the USA. (b) Wild-type histone chromatin fibers with 167- and 197-bp NRLs show different response to applied force. F-E curve represents both Chromatin reconstitutions with different NRLs unfolding traces. Both traces show that low force regime (at 3-4 pN) referred to nucleosome unstacking and outer turn unwrapping presents lengthening plateau, while high force regime (≥ 7 pN) referred to nucleosome inner turn unwrapping presents stepping events. Adapt from [104] Licensed under (CC BY 4.0).

1.5 Introduction for MT

Magnetic tweezers rely on the manipulation of superparamagnetic beads using a gradient of magnetic field. One of the major advantages of MT is the possibility of multiplexing so that within a single measurement, multiple individual molecules can be tracked and manipulated in real-time. In addition, the method can not only stretch biomolecular samples but also twist and apply torques to multiple tethers.

The first magnetic tweezers were assembled in 1996 by Strick, Bensimon, and Croquette [105, 106]. They used this setup to explore the elasticity of supercoiled DNA. In magnetic tweezers, DNA molecules are tethered in a flow cell between a glass surface and a paramagnetic bead by means of non-covalent bonds. The flow cell is exposed to a magnetic field B generated by a pair of permanent magnets (or electromagnets, in some cases [107]) suspended on a motorized stage. The magnetic field exerts an upward stretching force F on the bead. The force exerted by the tweezers is given by:

$$\vec{F} = \frac{1}{2} \vec{\nabla}(\vec{m} \cdot \vec{B})$$

Where \vec{m} is the induced magnetic moment of the bead in the external magnetic field \vec{B} . The force F can be controlled by moving the permanent magnets up or down. LED illumination from above the flow cell and the magnet is employed to illuminate the beads. The interference of the illuminating light with the light scattered by the bead produces diffraction patterns in the focal plane. The exact profile of those patterns is correlated with the distance of the bead to the focal plane of the objective. The image of the diffraction pattern is recorded through an objective with a charge-coupled device (CCD) camera. Tracking is achieved by analysis of the image of the bead (Figure 1.12).

The applied force can be calculated from the horizontal bead fluctuations $\langle \delta x^2 \rangle$. For the known extension of DNA nucleic acid, l , tethered to the surface. The average potential energy by the expression:

$$\langle E_p \rangle = \frac{1}{2} \frac{F}{l} \langle \delta x^2 \rangle$$

F / l represents an effective trap stiffness in the x direction. According to the equipartition theorem $F/l \cdot \langle \delta x^2 \rangle = k_B T$, where T is the temperature and k_B is the Boltzmann constant, leading to the following relationship:

$$F = \frac{k_B T l}{\langle \delta x^2 \rangle}$$

Instead of calibrating the force by directly computing the variance of the fluctuations $\langle \delta x^2 \rangle$, calibration typically uses analysis of the power spectrum or the Allan variance, which allows to (partially) correct for the finite acquisition frequency of the camera and mechanical drift [108, 109].

1.5.1 Mechanical properties of a stretched and supercoiled DNA

DNA stretching by force –at least at low forces– is mainly defined by its polymeric properties. The persistence length (L_p) is the primary parameter to quantify the (bending) stiffness of DNA. DNA is thought of as a semi-flexible polymer in the so-called worm-like chain (WLC) model [110]. In particular, Bustamante *et al.* have shown that the force-extension diagram of a DNA molecule is well described by a WLC model [111-113]. The WLC model considers the polymer as a continuously flexible chain with a quadratic elastic bending energy. It also shows that the chain is subjected to thermal fluctuations, which result in an entropic force to resist the attempt to stretch the polymer to its full contour length (L_c). Therefore, by incorporating a force along the axis of DNA extension, the stretching energy E^{WLC} is:

$$E_{\alpha}^{\text{WLC}} = \int_0^{L_c} ds \left(\frac{A}{2} \left| \frac{dt(s)}{ds} \right|^2 - F \cos \theta(s) \right)$$

The first term $\frac{A}{2} \left| \frac{dt(s)}{ds} \right|^2$ describes the resistance of the chain to bending. The resistance is proportional to the inverse square of the radius of curvature, R . R^{-2} is with respect to the arc length, s , of the unit tangent vector $t(s)$. The second term $-F \cos \theta(s)$ given the stretching energy from force and $\cos \theta(s)$ is the angle between $t(s)$ and the z axis. The quantity A is related to L_p by $L_p = A * 1/k_B T$. In 1994, an interpolation formula for the WLC to describe the force-extension relationship was given [113]:

$$F = \frac{k_B T}{L_p} \left[\frac{1}{4(1-z/L_c)^2} - \frac{1}{4} + \frac{z}{L_c} \right]$$

To fit the above equation to the experimental data more accurately, Bouchiat *et al.* subtracted the interpolation formula from the exact numerical solution of the WLC and expressed the residuals as a seventh-order polynomial to provide correction terms [114]. The more accurate approximation to the WLC is written as:

$$F = \frac{k_B T}{L_p} \left[\frac{1}{4(1-z/L_c)^2} - \frac{1}{4} + \frac{z}{L_c} + \sum_{i=2}^{i \leq 7} \alpha_i \left(\frac{z}{L_c} \right)^i \right]$$

where $a_2 = -0.5164228$, $a_3 = -2.737418$, $a_4 = 16.07497$, $a_5 = -38.87607$, $a_6 = 39.49944$, $a_7 = -14.17718$. This refined WLC model provides a better approximation and is used here to fit the experimental nucleic acid stretching data.

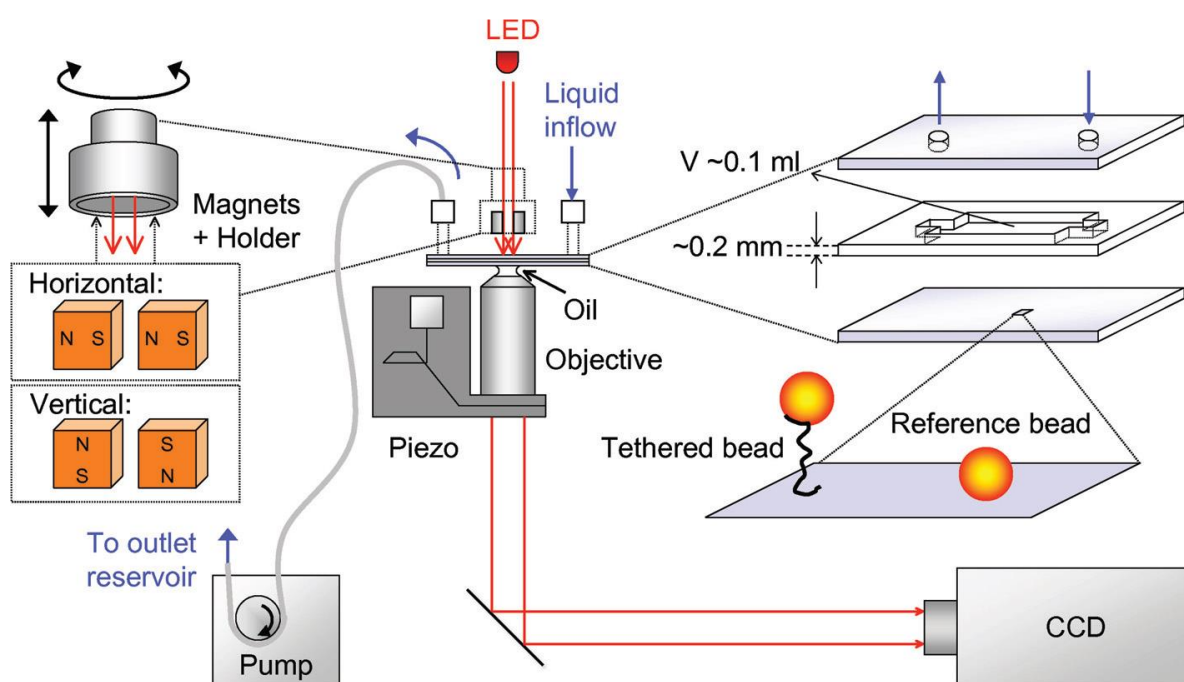


Figure 1.12: Schematic representation of a magnetic tweezers (MT) set-up. A flow cell is prepared to be as measurement chamber. Two cover slides are separated at the edges by a thin layer of ~0.2 mm thin parafilm. The top cover slip with two holes are connected to an inlet and an outlet reservoir, allowing solutions to be flushed in and out of the cell using a pump. One end of polymers will be immobilized to the bottom surface while the other end to a paramagnetic bead. Reference beads are located to the bottom surface with polymers together. Laser light source is located above the cell to illuminate the field of view as well as a pair of permanent magnets, that can be moved vertically and rotated to vary force and torque on magnetic bead. An objective is below the flow cell. An outgoing laser beam passed through flowcell and objective was deflected by a mirror into a charge coupled device (CCD) camera to record the image from the objective focal plane. LED, light-emitting diode. Reprinted with permission from [115]. Copyright by Springer Nature.

1.5.2 Attachment of DNA to the surface

Preparation of DNA constructs with multiple attachment sites for single-molecule torque and twist assays requires several biochemical reactions. The most frequently used protocol involves PCR, restriction reactions, and final ligation to assemble three different DNA

fragments into the final construct [105, 115-117]. The central segment of the DNA molecule is unlabeled, while the two ends of the molecular construct are labeled with different moieties that enable attachment, with multiple biotin and digoxigenin (dig) labels, respectively, being a popular choice. The products of the ligation reactions are a mixture involving off-target DNA and unligated strands. Therefore, subsequent gel purification is often required to obtain the specific DNA construct. Unfortunately, these procedures lead to low yield and are prone to introduce nicks into the DNA.

To overcome the inefficiency of generating DNA through ligation-based protocols, improved methods are needed to simplify the process and increase the yield. Recently, new methods have been developed to generate high-yield DNA constructs for force and torque spectroscopy experiments [118]. In particular, a ligation-free method has been reported that achieves high yield of torsionally constrained DNA and efficiently incorporates different labels at the end of DNA [119]. The strategy is based on two PCR-synthesized DNA constructs that are used as “megaprimers” with biotin and digoxigenin labels, respectively, to amplify the target DNA in a final PCR step. The megaprimer-based PCR reaction can create torsionally constrained DNA without ligation and restriction reactions. However, an additional requirement for biomechanical characterization at the single-molecule level is efficient and stable tethering of the biomolecules of interest. The commonly used attachment strategy relying on the binding of biotin to streptavidin-coated beads and the binding of dig labeled nucleotides to a surface coated with antibodies against dig (anti-dig) is rapid and reliable. The biotin-streptavidin interaction exhibits good force stability, despite being non-covalent, and can be optimized through engineered streptavidin variants [120-122]. Unfortunately, the anti-dig/dig interaction has much lower stability under forces > 10 pN [123, 124]. Therefore, it is desirable to go beyond non-covalent attachment and introduce one or more covalent linkages, which can provide force stabilities up to nN [125]. Several approaches for covalent attachment have been developed [125-128] and provide stability for long measurements and experiments over a broad force spectrum [129-134]. For DNA attachment via dibenzocyclooctyne (DBCO), covalent binding to an azide-functionalized surface has been developed. This copper-free click chemistry method is specific, highly efficient and yields tethers that are able to withstand very high forces (>100 pN) [128].

1.6 Outline of this thesis

This thesis mainly focuses on probing the mechanical properties and responses to forces of nucleosomes using magnetic tweezers. Multiplexed magnetic tweezers provide a detailed view of structural transitions in nucleosome fibers under force. In addition to force, magnetic tweezers can apply torque, to look into the influence of small molecules on DNA helicity. The other application is by applying force to look into the detail nucleosomal arrays structure states at different forces. Force spectroscopy measurements require suitable and robust molecular attachment strategies. To build a robust anchoring strategy for pulling nucleosome fibers, I developed a new DNA attachment strategy to improve the stability of bare DNA and nucleosome fiber tethering. I then leveraged the new approach and applied it to study different variant nucleosome arrays. Therefore, by applying the new methods, I reconstituted nucleosomal arrays with unmodified, acetylated, or trimethylated histone octamers and pulled them by magnetic tweezers.

Here, I present a novel attachment protocol that combines the high-yield enabled by the megaprimer approach with the supreme force stability afforded by covalent DBCO/azide coupling for anchoring DNA in tweezers experiments. My strategy is based on DNA constructs with multiple biotin and DBCO labels at each end, respectively, and assembly via ligation-free PCR. The constructs enable torsionally constrained coupling and excellent force stability. The high yield of the approach enables us to obtain sufficient material for downstream biochemical preparation, in particular for nucleosome reconstitution.

By applying the developed new methods, I investigate the mechanisms of different nucleosome PTMs on DNA compaction. I employ tri-nucleosome constructs, which are intermediate in complexity between mononucleosome and higher-order nucleosome fibers or chromatin. I employ two highly complementary single-molecule techniques: atomic force microscopy and magnetic tweezers. Our results on higher-order compaction are compared to mononucleosome AFM data published previously and help to explain the function of PTMs on different hierarchical structures. Our magnetic tweezers measurements follow the workflow presented in Chapter 2.2 and provide a better understanding of PTMs structural differences by gradually disrupting nucleosomal array.

Finally, a discussion of the findings of this work will be given in Chapter 4.

2. Results

2.1 The calibration of magnetic tweezers

Single-molecule MT enables us to control stretching forces and rotational orientation of molecules tethered between a surface and magnetic beads. Before doing measurements to probe molecules and their interactions of interest, it is crucial to determine the spatiotemporal resolution and to test the limitations of our home-built setup. In addition, force calibration is necessary to obtain the forces corresponding to different magnet positions. Allan deviation (AD) is a tool commonly used for testing the resolution of tracking beads (see Materials and Methods). By incubating different sizes of reference beads: 1 or 3 μm diameters, to stick to the surface, irrespectively, I tracked the z-signal of the reference beads (see Materials and Methods) and it shows that the resolution achieves the highest (i.e. lowest σ_z) when $\tau \sim 10$ s for both 3 μm and 1 μm reference beads. Comparing bead sizes, the 3 μm reference bead achieves higher resolution than 1 μm reference beads, consistent with a simple model based on Mie scattering [135]. 3 μm bead shows the lowest Allan deviation at ~ 0.03 nm while 1 μm bead shows Allan deviation ~ 0.06 nm (Supporting Information & Supplementary Figure 5.1). The results confirm that our home-built setup achieves spatiotemporal resolution similar to previously published results [109, 135, 136] and can sensitively detect changes in bead height caused by the changes in sample structure. In addition, I performed force calibration by analysis of the horizontal fluctuations due to Brownian motion. The results of force-extension measurements using the long 20.6 kbp DNA used for force calibration are well described by the worm-like chain model [113, 114, 137], with values in good agreement with previous literature (Supporting Information & Supplementary Figure 5.2). The results show that our home-built setup is ready for the study of biomechanical properties of biopolymers.

2.2 High-yield, ligation-free assembly of DNA constructs with nucleosome positioning sequence repeats for single molecule manipulation assays

My protocol for the construction of end-labeled DNA constructs for single-molecule experiments has two key PCR steps (Figure 2.1a). In the first step, regular primers are used in PCR reactions that include modified nucleotides to generate ~380 bp labeled DNA constructs. These labeled DNA constructs are used as “megaprimers” in a second PCR reaction with regular nucleotides to generate the final ~kbp DNA constructs with labeled ends.

2.2.1 Generation of labeled megaprimer constructs by PCR

I assembled 380 bp dsDNA labeled megaprimer constructs by PCR. In the PCR reaction to assemble functionalized megaprimers, I used 20 nt forward and reverse primer, pFMP218 as template, and a non-proofreading Taq polymerase or KOD Hot Start polymerase (see Materials and Methods). I added biotin-16-dUTP or DBCO-(PEG)₄-dUTP to the PCR reaction, up to 50% of modified dUTP. Gel analysis shows that the PCR reactions with labeled nucleotides yield single bands (Supplementary Figure 5.3). As the percentage of modified dNTPs increases, a decrease in amplicon mobility is observed. This is consistent with the previously observed change in mobility due to the bulky side chains introduced by biotin-dUTP derivatives [138]. I similarly attribute the mobility shift of the DBCO-(PEG)₄-dUTP substitution to the bulky side chain. I find that amongst the tested conditions, the mobility of the amplicons is lowest (and thus the number of incorporated labels the highest) for KOD Hot Start polymerase with 50% dTTP substitution (Supplementary Figure 5.3). I, therefore, used the megaprimers generated using the combination of KOD polymerase and 50% dTTP substitution in the subsequent steps.

2.2.2 Megaprimer PCR reaction to generate labeled DNA constructs for single-molecule measurements

The megaprimer approach has originally been used for site-direct mutagenesis. More recently, the approach has been expanded by using biotin-labeled and dig-labeled megaprimers to generate DNA constructs with multiple labels at both ends by PCR amplification [119]. I optimized conditions to assemble labeled DNA construct with arrays

of nucleosome positioning sequences by PCR. A biotin-labeled megaprimer is used in this second PCR step as the forward primer and a DBCO-labeled megaprimer is used as reverse primer, to generate final DNA constructs with functionalized ends (Figure 2.1a). To suppress off-target products, I prepared a linear template by PCR amplification. As the template, I used a 2823 bp plasmid DNA comprising three Widom 601 sequences. I followed the megaprimer method described previously [119] as a starting point, which uses KOD Hot Start polymerase, which is thermostable and designed to amplify difficult amplicons. I optimized PCR reaction conditions by adding DMSO and decreasing the polymerase concentration (Supplementary Figure 5.4a and 5.4b and Materials and Methods). To test the applicability of the customized protocol, I combined different substitutions of megaprimers to process PCR reactions. In my final protocol, I use megaprimers prepared with 50% biotin-dUTP and 50% DBCO-dUTP substitution (Supplementary Figure 5.4).

To test the reproducibility of our protocol, I performed 5 repeats of the PCR amplification for different megaprimer combinations. I find that each repeat of the experiments successfully amplified the target products (Supplementary Figure 5.4c,d). To assess the purity from the PCR amplifications, I quantified the target product intensity relative to the integrated lane intensity (Supplementary Figure 5.4e). The average purities from different combinations of megaprimers show similar values for different megaprimers used and are >50% in all cases tested. In summary, my optimized megaprimer PCR approach enables reproducible amplification of high purity DNA constructs with specific modifications at both ends. The yield and purity are considerably higher than what is achieved in previous, ligation-based protocols, which is critical in particular for nucleosome assembly on the functionalized DNA. In addition to the DNA constructs with three Widom 601 nucleosome positioning sequences, I also generated a functionalized DNA construct with one Widom 601 (Supplementary Figure 5.6) and my colleague, Dr. Pauline Kolbeck, generated a longer 6.6 kbp DNA without nucleosome positioning sequences (Supplementary Figure 5.7) under my instruction, using the megaprimer approach with biotin and DBCO labels. In both cases we obtained torsionally constrained DNA tethers suitable for magnetic tweezers experiments (Supplementary Figure 5.6 and 5.7), demonstrating the versatility of the approach.

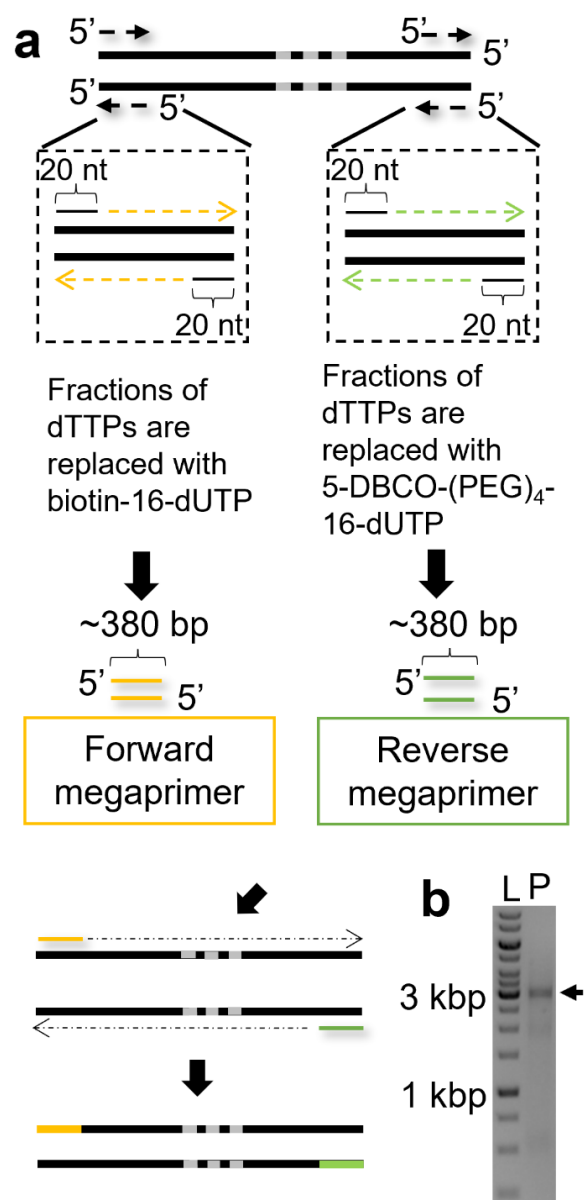


Figure 2.1: Ligation-free megaprimers PCR-based DNA assembly method. (a) Schematic of the ligation-free method to synthesize torsionally constrained DNA. Briefly, two sets of 20-bp ssDNA primers and linearized templates are used in PCR reactions to make two multi-labeled ~380 bp DNAs that become the megaprimers. The two megaprimers are labeled with biotin and DBCO, respectively. A linearized template with three repeats of the Widom 601 sequence (shown schematically as grey bars) is used for subsequent PCR to get the final 2823 bp PCR construct. (b) Visualization of the PCR result by gel electrophoresis. The left lane (“L”) has a DNA size ladder (1 kb PLUS, NE Biolabs). The black arrow in the left lane (“P”) indicates the position of PCR product.

2.2.3 Force response of megaprimer DNA constructs in magnetic tweezers

To obtain a high density of labels on the DNA, I used 50% Biotin-dUTP and 50% DBCO-dUTP megaprimers for amplification and tested the resulting labeled DNA construct in our single-molecule magnetic tweezers set up (Figure 2.2a and Materials and Methods). In the magnetic tweezers flow cell, the 2823 bp DNA tethers were anchored with copper-free click chemistry [128] to the surface and via biotin-streptavidin coupling to magnetic beads. I tracked the position of the magnetic beads while applying calibrated forces [108, 139]. From the mean extension as a function of applied force, I obtained force-extension curves (Figure 2.2b). As expected, the force-extension behavior of DNA closely follows the extensible worm-like chain (WLC) model until ~ 40 pN. At forces > 60 pN, the force-extension response of the DNA tethers exhibits two different behaviors: some molecules still behave similarly to the worm-like chain model, while others exhibit overstretching behavior at about 65 pN, which corresponds to the characteristic signature of stretching torsionally unconstrained double-stranded DNA [111, 140, 141]. The absence of an overstretching transition in our force range for some DNA tethers is consistent with the expectation for fully torsionally constrained DNA, for which the overstretching transition is suppressed at forces below 110 pN [111, 141].

To determine the lifetime of our DNA tethers under mechanical load, I subjected them to a constant force of 45 pN and recorded the position traces of the beads until rupture of the molecular tethers. I analyzed the lifetimes until rupture and find an approximately exponential lifetime distribution with a fitted mean lifetime of 70 ± 3 h (Figure 2.2c). The DNA construct is modified with multiple biotin and DBCO labels at the opposite ends. The DBCO based coupling has been reported to provide force stability up to nN [125, 128]. In contrast, while the streptavidin-biotin bond has an extraordinarily high affinity ($K_d \sim 10^{-14}$ M), the interaction is non-covalent and can be broken under external forces well below 1 nN [120, 122, 142]. The tetrameric structure of streptavidin and its non-specific coupling for commercially available beads means that different force-loading geometries are possible, which gives rise to a broad range of multi-exponential lifetimes [120-122]. Previous work has shown that an engineered monovalent variant of streptavidin in the most stable geometry (1SA) exhibits a lifetime $\tau_1 = 11.2 \pm 0.4$ h at 45 pN for a single biotin-streptavidin bond. I attribute the fact that I observed an even longer lifetime than what was found for the single, engineered streptavidin at the same force, despite using commercially available beads without the optimized streptavidin, to the fact that our tethers feature multiple biotin labels

that can bind to the bead and, therefore, significantly increase the overall lifetime under force. Similarly, Janissen *et al.* have investigated different DNA constructs by using magnetic tweezers [124]. They found that the lifetime under a force of 45 pN for traditional biotin and digoxigenin-based DNA anchoring is only ~ 7 min. If the digoxigenin is replaced by covalent anchoring while retaining

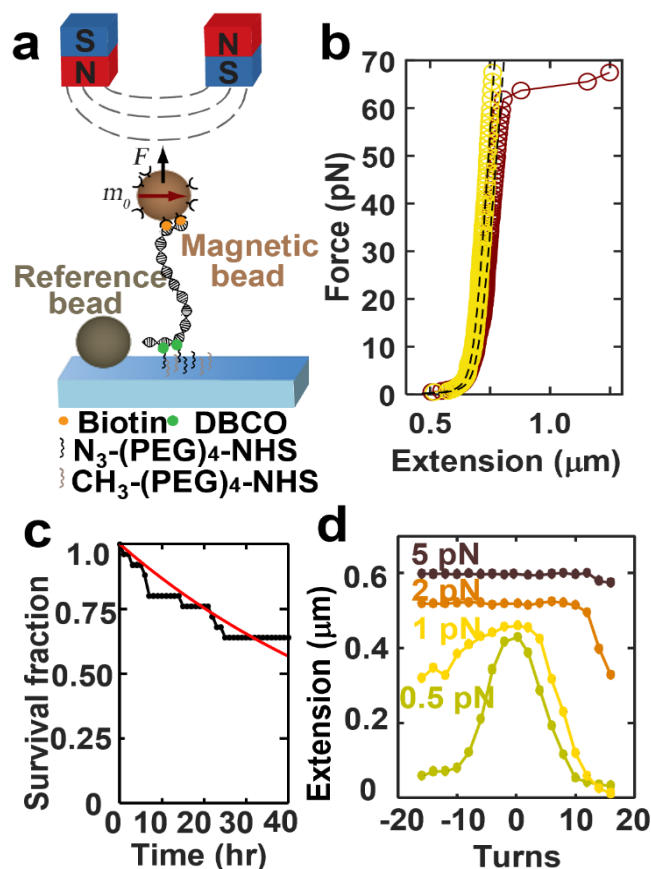


Figure 2.2: Force spectroscopy experiments on megaprimer generated DNA constructs in magnetic tweezers. (a) Schematic of the magnetic tweezers set-up. The flow cell surface is functionalized with azide-(PEG)₄-NHS. The DNA construct has two handles, one labeled with multiple biotins and the other with multiple DBCOs. The biotins bind to multiple streptavidins that coat the magnetic bead and DBCOs at the other end form the covalent bond with the azide group. (b) Force-extension curves of DNA molecules anchored as shown in panel a. Representative force-extension measurements of torsionally constrained (yellow), unconstrained DNA molecules (brown), and co-plot of the extensible WLC model with a bending persistence length of 45 nm (black dashed line). Torsionally unconstrained DNA exhibits the overstretching transition near 65 pN; the torsionally constrained molecule does not overstretch at 65 pN. (c) Fraction of DNA tethers remaining as a function of time when subjected to a constant force of 45 pN. The red line is an exponential fit to the data with a mean lifetime of (70 ± 3) h. Analyzing the torsionally constrained and unconstrained tethers separately, I find very similar lifetimes of 68 ± 2 h and 76 ± 3 h. (d) Extension-rotation curves at constant forces of 0.5, 1, 2, 5 pN indicate that the DNA construct is torsionally constrained and shows the well-known response of double-stranded DNA [105, 143].

the single biotin-streptavidin linkage at the other end, the lifetime increases to ~3 h, highlighting the dramatic increase in force stability afforded by replacing the dig-antidig coupling to the surface with a covalent attachment approach. The fact that I achieve an approximately 20-fold longer lifetime compared to Janissen *et al.* might be due to their lower label density or the fact that they used neutravidin instead of streptavidin [116, 124].

2.2.4 Torsional response of megaprimer DNA constructs in magnetic tweezers

To determine whether the attachment protocol with multiple labels at both ends enables supercoiling experiments on DNA tethers, I systematically under- and overwound the DNA by rotating the magnets from -16 to 16 turns at forces of 0.5, 1, 2, and 5 pN (Figure 2.2d). Below 1 pN, the rotation curve of DNA behaves symmetrically and the extension of DNA decreases on overwinding or underwinding past the buckling point [105, 116, 143]. At 1 and 2 pN, the extension-rotation response of the DNA is asymmetric, due to torque-induced melting of the DNA [144]. Overall, the measurements recapitulate the well-known extension-rotation response of double-stranded DNA. I typically obtain 50% of supercoilable (i.e. fully torsionally constrained) DNA tethers (27 of 57 tethers), comparable to previous protocols [118, 119]. For the 6.6 kbp DNA construct without nucleosome positioning sequences, Pauline Kolbeck performed additional experiments using high-speed tracking at 1 kHz and recapitulate also the known behavior of the variance of the extension fluctuations upon over- and underwinding [145] (Supplementary Figure 5.7c,d).

2.2.5 Estimation of labeling efficiency from magnetic tweezers rupture time traces

Examining the extension time traces prior to tether rupture carefully, I find occasional steps in the tether extension (Figure 2.3a). Increases in tether extension prior to tether rupture are consistent with the disruption of biotin-streptavidin bonds, where the final rupture corresponds to the last biotin-streptavidin pair. Prof. Jan Lipfert quantified the observed steps and find a rather broad distribution with a mean step size of $13.0 \text{ nm} \pm 14.8 \text{ nm}$ (mean \pm standard deviation). We then compared the experimental step size distributions (Figure 2.3b, grey bars) to a simple model for step sizes based on the experimentally used megaprimer sequences

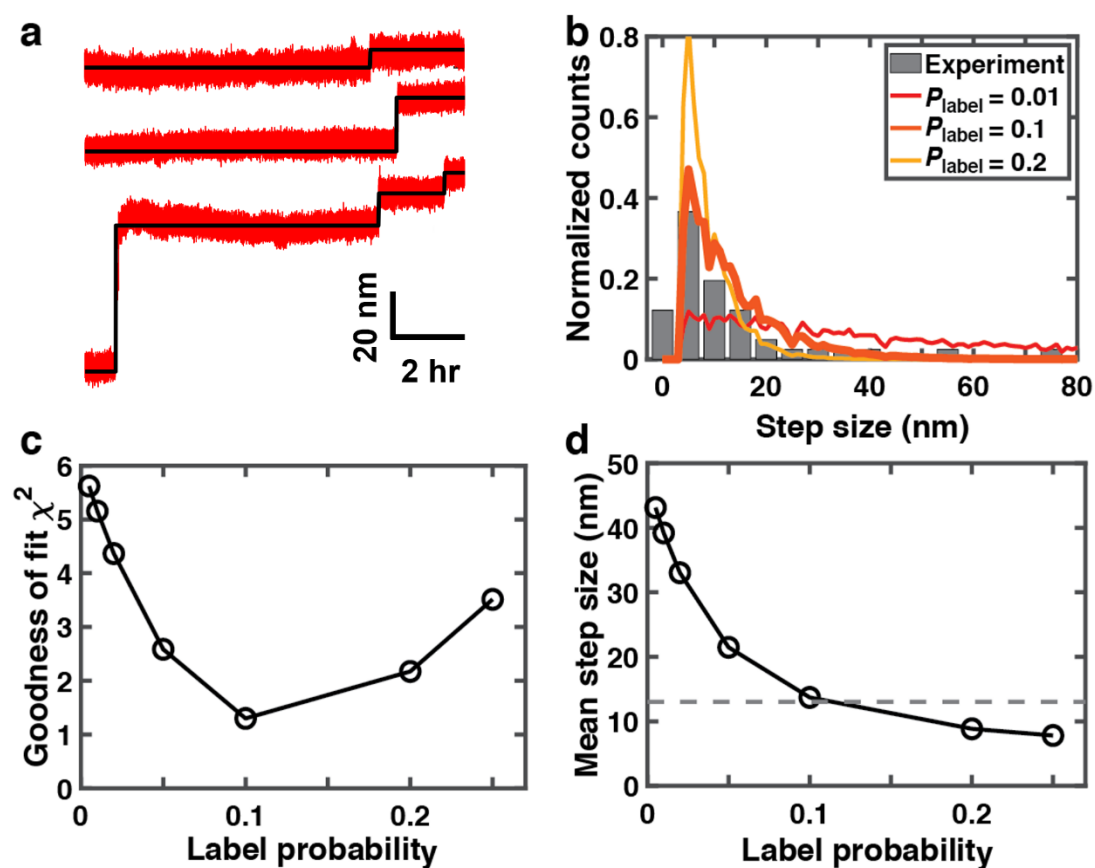


Figure 2.3: Analysis of tether rupture steps to estimate the labeling efficiency for DNA tethers. (a) Examples of the rupture steps in extension time traces under an applied force of 45 pN (red lines). The black lines are steps in the traces as determined by a step-finding algorithm [146]. (b) Experimentally observed step sizes in extension time traces before tether dissociation (gray bars; $N = 41$ steps). Co-plotted are the step size distribution predicted by our simple model (see “Model for the step size distributions” in Materials and Methods) that takes into account stochastic label incorporation for three selected values of the label probability P_{label} (color lines; P_{label} values are indicated in the legend; simulation results are for 100,000 simulated tethers for each condition). (c) Goodness of fit comparing simulated step size distribution with the experimental data. The goodness of fit is computed as the sum of squared differences of normalized counts in each bin for simulated and experimentally observed data. (d) Mean step size from simulated step size distributions vs. P_{label} . The horizontal dashed line corresponds to the experimentally determined value. Standard errors of the mean are not shown, as they are smaller than symbols sizes.

and simulated label incorporation (see the section “Model for the step size distributions” in Materials and Methods). This simple model can account for the overall shape of the observed step size distribution, with an initial sharp increase and subsequent slow decay of the probability of steps with their size. The predicted step size distribution shifts to smaller step sizes for higher label efficiencies P_{label} (Figure 2.3b, colored lines), where P_{label}

represents a combined effective probability of incorporating a label and binding to an available streptavidin. We find good agreement both of the mean step size and overall distribution (Figure 2.3c,d) for $P_{\text{label}} = 0.1$. The best fitting value of $P_{\text{label}} = 0.1$ is 5-fold lower than the ratio of labeled nucleotides in the PCR mix (which is 50%), which suggests that the KOD polymerase used in our experiments preferentially incorporates unlabeled nucleotides, similar to what has been reported for other polymerases [147-152] and/or that not all incorporated biotin labels attach to a streptavidin binding site, likely due to steric constraints. These observations are also consistent with the finding that, while in principle torsionally constrained attachment of DNA or RNA tethers only requires two attachment sites at each end, in practice at least ~10 potential attachment sites should be incorporated at the respective ends to ensure a high number of stable and torsionally constrained tethers [140].

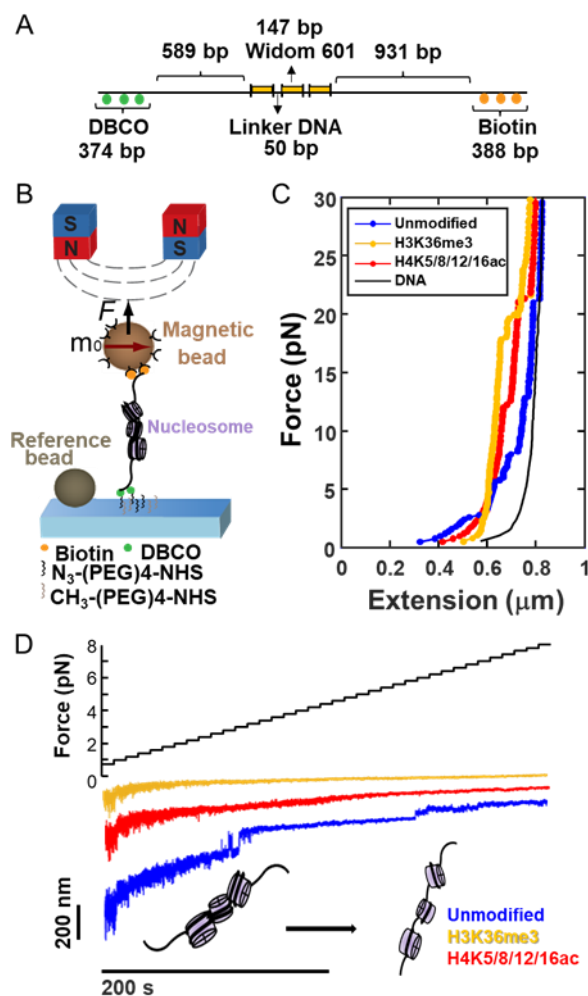
2.3 Epigenetic histone modifications H3K36me3 and H4K5/8/12/16ac induce open polynucleosome conformations via different mechanisms

My megaprimer assembly-based DNA construct shows proof-of-concept results. That means the approach can facilitate the study of DNA interactions with nucleoprotein complexes. I utilize the protocol to investigate the influences of epigenetic histone modifications on structural dynamics by using magnetic tweezers force spectroscopy and provide complementary results from AFM imaging.

2.3.1 Magnetic tweezers force spectroscopy probes unmodified, H4K5/8/12/16ac, and H3K36me3 tri-nucleosome constructs

To test whether my megaprimer assembly-based DNA construct can be used to assemble and measure nucleosomes, and also further study the behavior of variants nucleosomes under controlled stretching forces by using multiplexed magnetic tweezers, I assembled different variants nucleosomes on a 2823 bp DNA construct with biotin labels on one and DBCO labels at the other end, separated by unmodified DNA from a central segment containing 3x W601 and 50 bp of linker DNA each (Figure 2.4a) to reconstituted unmodified, H3K36me3, and H4K5/8/12/16ac tri-nucleosomes. The biotin labels enable attachment to streptavidin-

coated magnetic beads (M270, 2.7 μm diameter), while the DBCO labeled-end provides covalent attachment to azide-functionalized glass slide surface via copper-free click



chemistry [153] (Figure 2.4a). To confirm the assembly of nucleosomes and to quantify the

Figure 2.4: Probing tri-nucleosomes in magnetic tweezers (a) Schematic of the DNA construct used for magnetic tweezers. The 2823 bp DNA consists of three 147 bp Widom 601 nucleosome positioning sequences that are flanked by a 589 bp short arm and extra 374 bp fragment with DBCO labeled, and a 931 bp long arm and extra 388 bp fragment with biotin labeled, respectively. (b) Schematic of the magnetic tweezer set-up. Nucleosomes are reconstituted on DNA with two functionalized ends, one labeled with multiple biotins and the other with multiple DBCOs. The DNA construct is amplified by using the ligation free “megaprimer” method described previously [153]. The flow cell surface is functionalized with azide-(PEG)₄-NHS. The magnetic beads are labeled with streptavidin. (c) Force-extension curves of different variant nucleosomes and bare DNA anchored as shown in panel A. Nucleosome samples were stretched under applied forces from 0.5 to 30 pN. (d) Force ramp at low force (Force \leq 8 pN; top) of different variants of nucleosome. The extension time traces (color curves; bottom) show different length plateaus at forces \leq 8 pN that indicate outer turn unwrapping and unstacking of polynucleosomes. Same color code as in panel c.

different polynucleosome populations, I used AFM imaging to count the number of successfully assembled bare DNA, and DNA with mono-, di-, tri-nucleosomes (Supplementary Figure 5.8). The population distributions for unmodified, H3K36me3, and H4K5/8/12/16ac within experimental errors, show a simple binomial distribution. We also performed the same analysis on assembled DNA with variants nucleosomes used for AFM measurement (see Materials and Methods) as discussed in Chapter 2.3.4 with a simple binomial distribution (Supplementary Figure 5.11). Both results imply that nucleosome assembly on three Widom 601 sites is relatively uncooperative under the conditions of our experiments, consistent with previous observations [154].

I performed force-extension experiments on polynucleosome arrays by applying constant forces in the magnetic tweezers from 0.5 to 30 pN in 0.2 pN increments, each for 5 s (for forces > 8 pN) or 10 s (\leq 8 pN). My master's student, Evdoxia Karagianni, assisted me force-extension experiments on DNA. The raw extension traces reveal considerable variability for all variant polynucleosomes (Figure 2.4d and Supplementary Figure 5.9), showing the heterogeneity and complexity of our reconstituted samples. The time traces also reveal that, superimposed on the expected force-extension stretching response of double-stranded DNA, there are jumps and hopping events visible in the data, qualitatively in line with nucleosomes unwrapping and unstacking. I compared the different tri-nucleosome constructs by taking the mean extension for each force plateau to obtain force-extension curves (Figure 2.4c). I find that at low forces (\leq 8 pN), the unmodified nucleosome tethers tend to have a shorter extension compared to H3K36me3 and H4K5/8/12/16ac. In addition, the raw extension vs. time traces below for forces \leq 8 pN show that unmodified nucleosomes exhibit larger fluctuations due to hopping or stepping contributions compared to H3K36me3 and H4K5/8/12/16ac constructs (Figure 2.4d and Supplementary Figure 5.9). At high forces (> 8 pN) all types of nucleosomes show steps with comparable properties.

2.3.2 Repeated stretching and release cycles indicate that mechanical forces disrupt some but not all nucleosome interactions

I observe clear differences in the tether responses between the first stretching cycle (going from 0.5 to 30 pN) and the first release or second stretching cycle (Supplementary Figure 5.10). After the first stretching cycle, the tether lengths at a given force are increased compared to the initial stretching cycle for all nucleosome variants investigated, suggesting that at least some of the nucleosome structures are permanently disrupted by applying forces,

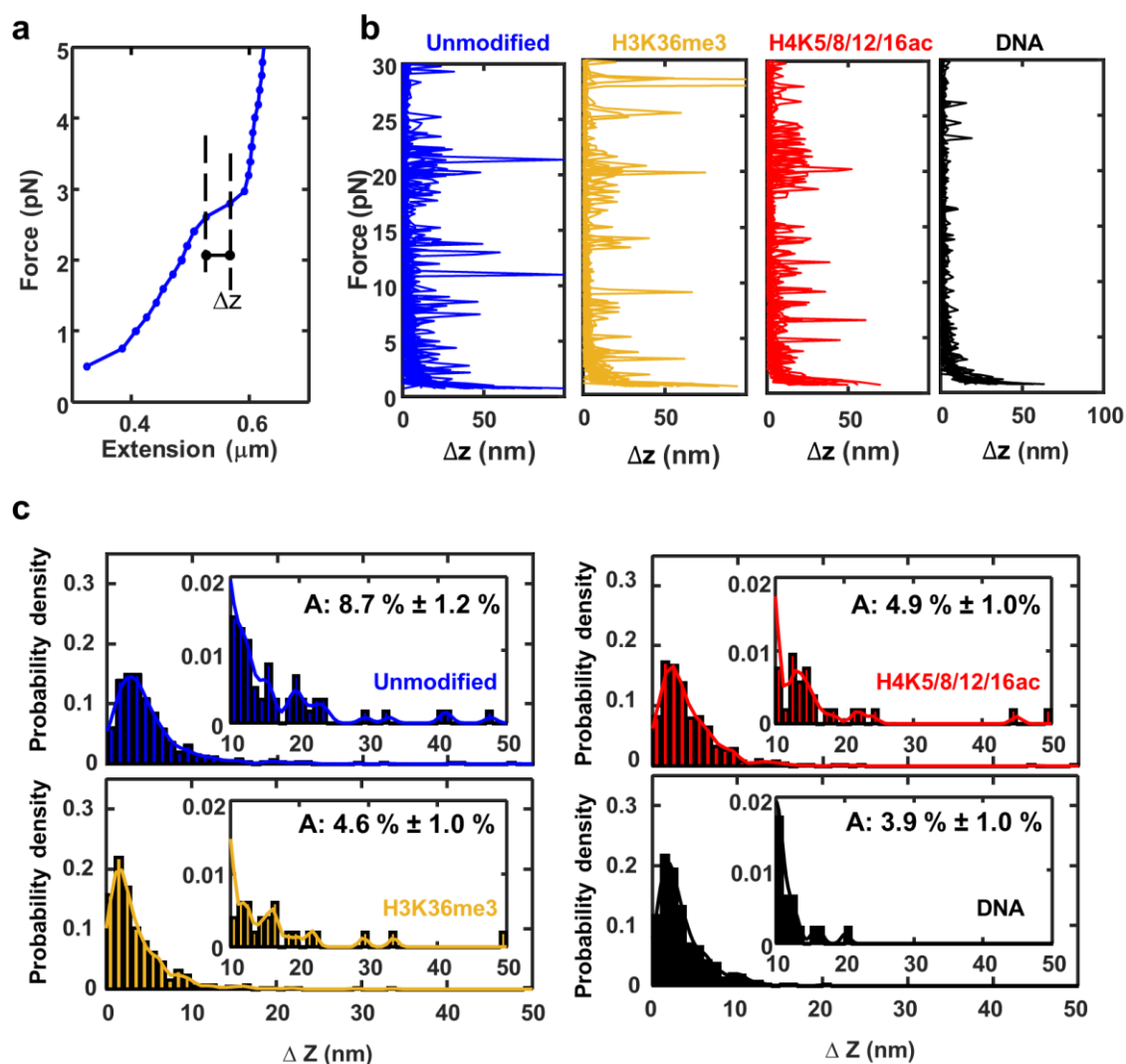
in agreement with previous literature [98, 155]. Nonetheless, repeated force-extension cycles still show steps and a decreased extension, compared to bare DNA, at low forces, implying that some nucleosomes remain bound or can rebind even after stretching to 30 pN, consistent with previous observations that the core particle may reassemble upon relaxation after peeling off the inner turn DNA [98, 156-159].

2.3.3 Force spectroscopy suggests a reduction of stacking and outer turn wrapping interactions in H4K5/8/12/16ac and H3K36me3 compared to unmodified nucleosomes

The time traces in the low force regime (≤ 8 pN) exhibit a broad range of steps, hopping behavior, and gradual changes in extension, while the traces at higher forces show more clearly defined steps. I attribute the changes in the range of 2-8 pN to unwrapping of the outer turn of DNA from nucleosomes and the disruption of nucleosome-nucleosome interactions. In contrast, the defined steps at high forces (> 8 pN) agree with previous reports [97, 100, 101, 155, 157, 160-166] of non-equilibrium peeling of the inner ~ 75 bp of DNA from the core of the octamer. Here, I first discuss the behavior at low forces (≤ 8 pN) and in the next section I analyze the steps at higher forces.

To compare the different variant nucleosomes in force-extension measurements, I computed the mean extension in z for each force plateau and calculated the difference in z between adjacent force steps (Figure 2.5a), defined as Δz . Spikes in Δz correspond to abrupt jumps in tether lengths (Figure 2.5b). The computed Δz values show that all types of nucleosomes demonstrate multiple spikes from low to high forces (Figure 2.5b). Unmodified nucleosomes have higher density of spikes, and the spikes are distributed over a broader range of forces. For both H3K36me3 and H4K5/8/12/16ac, the spikes are less dense at low force regime (≤ 8 pN) compared to the unmodified condition. I analyzed the Δz distribution at forces ranging from 2 to 8 pN. The result shows that H3K36me3 and H4K5/8/12/16ac have narrower distributions and a reduced population of events with $\Delta z \geq 10$ nm compared to unmodified nucleosomes (Figure 2.5c). By calculating the relative population for $\Delta z \geq 10$ nm, I find that H3K36me3 ($4.6\% \pm 1.0\%$) and H4K5/8/12/16ac ($4.9\% \pm 1.0\%$) exhibit significantly fewer large steps than unmodified nucleosomes ($8.7\% \pm 1.2\%$). The reduced number of stepping events in the force range 2-8 pN for H3K36me3 and H4K5/8/12/16ac compared to unmodified tri-nucleosomes suggests that these PTMs disrupt nucleosome-nucleosome

stacking and outer turn wrapping. The magnetic tweezers observations indicate more open and diverse conformations for H3K36me3 and H4K5/8/12/16ac.



Fig

ure 2.5: Analysis of force-extension reveals nucleosome unstacking and unwrapping. (a) Schematic of the Δz analysis, using the unmodified nucleosome force-extension curve from Figure 2.4b. I analyzed the force-extension data for polynucleosomes by averaging each force plateau's z positions and subtracting the average z position from the previous force plateau to obtain Δz . (b) Δz vs. force data for unmodified ($N=20$), H3K36me3 ($N=16$), H4K5/8/12/16 ($N=17$), and DNA ($N=15$). (c) Histograms of Δz values with kernel density estimates (solid lines) using the data in the force range 2-8 pN for different variant nucleosomes and bare DNA. The insets show histograms of Δz from 10 – 50 nm with kernel density estimates and the fractions of counts for $\Delta z \geq 10$ nm. A indicates the area under the curve for Δz from 10-50 nm. The indicated error is the counting error. The fraction of events with $\Delta z \geq 10$ nm is significantly lower for H3K36me3 or H4K5/8/12/16ac compared to unmodified nucleosomes ($p = 0.013982$ and $p = 0.021895$, respectively), while the difference between the two PTMs is not significant ($p = 0.93985$), based on two-sample two-tailed proportion tests.

2.3.4 Force spectroscopy finds no influence of the investigated PTMs on inner turn unwrapping of nucleosomes

The Δz vs. force plots from variant nucleosomes also show that at higher forces (> 8 pN), there are multiple spikes regardless of nucleosome types (Figure 2.5b). The corresponding steps are consistent with inner turn nucleosome unwrapping. To quantify the effects of the investigated PTMs on inner turn unwrapping, I analyzed the extension steps at high forces (> 8 pN) with the step-finding algorithm by Kerssemakers *et al.* [146] to identify unwrapping steps in our extension vs. time traces (Figure 2.6a). From the fits, I determine the differences between average extensions before and after the steps to obtain step sizes. The distributions of step sizes from the three different types of nucleosomes show very similar peaks with mean step sizes between 21-24 nm (Figure 2.6b), in excellent agreement with previous reports for step sizes of inner turn unmodified nucleosome unwrapping in the range of 20-30 nm [97, 100, 101, 155, 157, 160-166]. In addition, I analyzed the forces at which the high-force steps occur to quantify the force range of inner turn unwrapping. I again find remarkably similar force distributions for all types of nucleosomes studied, with mean forces well within experimental error, at 19-20 pN (Figure 2.6c). The results suggest that the H3K36me3 and H4K5/8/12/16ac PTMs have no significant effects on inner turn nucleosome disassembly. Inner turn nucleosome unwrapping is sudden due to the strong interactions near to positions ± 40 bp of DNA from the dyad axis [23]. Overall, the interactions between the inner turn DNA wrap and the histone octamer involve both electrostatic and non-electrostatic interactions, while the outer DNA wrap interactions with the histone octamer are dominated by electrostatic interactions [23, 97]. Consequently, the changes at the N-tail due to H4K5/8/12/16ac or H3K36me3 are unlikely to affect the inner turn nucleosomal DNA unwrapping, consistent with our experimental findings.

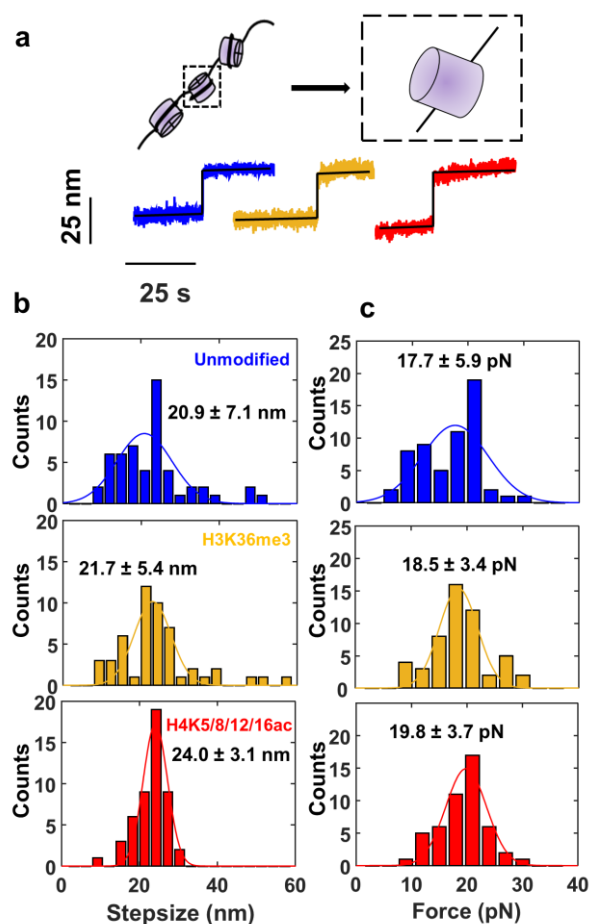


Figure 2.6: Analysis of inner turn DNA unwrapping in tri-nucleosome constructs under force. (a) Example of discrete steps in time traces (colored data) at forces > 8 pN, characteristic of the unwrapping of the inner DNA turn from nucleosomes. Black lines are fitted steps using algorithm by Kerssemakers *et al.* [146]. Unmodified nucleosome, blue line; H3K36me3 nucleosome, yellow line; and H4K5/8/12/16ac nucleosome, red line. (b) Histograms of the step sizes for inner turn unwrapping as determined in panel A. Solid lines are Gaussian fits and the means are indicated in the panels. (c) Histogram of the forces for inner turn unwrapping corresponding to the steps in panel b. Solid lines are Gaussian fits and the means and standard deviations are indicated in the panels. The step sizes and forces are not significantly different for any of the pairwise comparisons as determined by two-sample *t*-tests.

2.3.5 Assembly and AFM imaging of tri-nucleosome arrays

To prepare nucleosome samples for AFM imaging, My master's student, Peter Müller, and I assembled different variant nucleosomes by salt gradient dialysis on 895 bp DNA constructs. I designed and prepared DNA construct featuring three Widom 601 (W601) sequences [17] partitioned by 50 bp of linker DNA and flanked by a short arm 120 bp and long arm 232 bp (Figure 2.7). The same DNA construct was used for the different nucleosome variants. Peter Müller deposited nucleosome samples on poly-L-lysine coated mica and recorded high-

resolution AFM images (see Materials and Methods for details). AFM images (Figure 2.7) are obtained by amplitude modulation AFM in air and further analyzed to dissect the influences of PTMs on structural dynamics and geometry. The AFM images show populations of naked DNA, mono-, di-, and tri-nucleosomes (Supplementary Figure 5.11). I designed the DNA construct with two different length arms flanking the region with the W601 sequences to be able to determine nucleosome positioning. To quantify the positioning, we first evaluated the length of the two arms for individual tri-nucleosome particles (see Materials and Methods for details) (Figure 2.7e). The length of the short arm and long arm are 37.3 ± 8.4 nm and 71.6 ± 6.4 nm, respectively. These results are in excellent agreement with the expected values of 38 nm and 73 nm for short and long arm, assuming a DNA length per base pair of 3.14 ± 0.13 Å found previously by AFM imaging under similar conditions [24], fully consistent with the positioning of the nucleosomes on the W601 sequences.

We used AFM imaging to confirm the assembly of different variant nucleosomes and quantify the different polynucleosome populations, by counting the number of mono-, di-, tri-, and even occasional tetra-nucleosomes (requiring nucleosome loading to DNA outside of the W601 sequences) that are successfully assembled (Supplementary Figure 5.11). The populations for bare DNA, and DNA with one, two, three, and four nucleosomes are consistent, within experimental errors, with a simple binomial distribution (Supplementary Figure 5.11), which implies that the assembly of the different variant nucleosomes on the three W601 sites are all relatively uncooperative under the conditions of our experiments, consistent with previous observations [153, 154]. We find similar probabilities P for sites being occupied for the different variants, with nearly identical values for unmodified ($P = 0.418 \pm 0.010$) and H4K5/8/12/16ac ($P = 0.415 \pm 0.008$). H3K36me3 exhibits a slightly lower occupation probability of $P = 0.344 \pm 0.008$, which might be due to minor differences in the protein concentration due to experimental variability or due to a slightly lower affinity of the tri-methylated variant. Overall, AFM imaging confirms that nucleosomes of all three variants are assembled robustly on our DNA construct, with similar affinities and relatively low cooperativity between positioning sites.

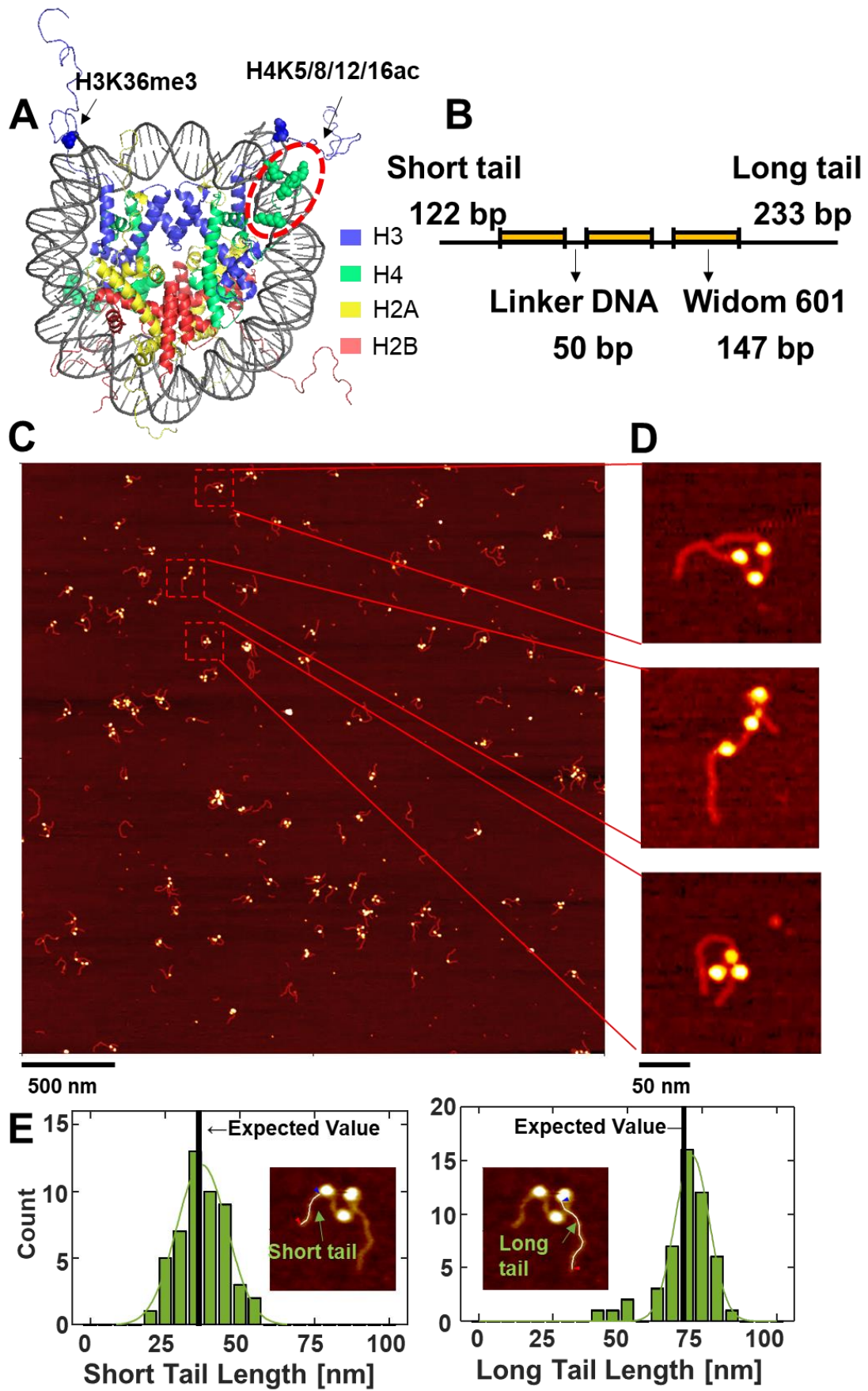


Figure 2.7: Analysis of tri-nucleosome conformations by AFM imaging. (a) Crystal structure of a canonical nucleosome (PDB 1KX5). Colored spheres represent the positions of the modified amino acids in the histone tail. Residues involved in H3K36me3 (i.e. three additional methyl groups at lysine 36 of histone H3) are shown as a blue sphere and in H4K5/8/12/16 ac (i.e. acetylation of H4 histones at lysines 5, 8, 12 and 16) as green spheres) (b) Schematic of the DNA construct used for AFM imaging. The 896 bp DNA consists of three 147 bp Widom 601 nucleosome positioning sequences that are flanked by a short and a long arm of 122 bp and 233 bp, respectively. (c) AFM image of DNA and tri-nucleosome sample with a field of view of $3\ \mu\text{m} \times 3\ \mu\text{m}$ (recorded with 2048×2048 pixels). (d) Zooms of selected tri-nucleosomes in the AFM image in panel c. e) Histograms of short and long arm length of unmodified tri-nucleosomes, with a Gaussian fitted to each distribution (green solid line). Insets show example image of tri-nucleosomes with the poly-line profile indicated that was used to measure the arm lengths. Vertical lines are the expected arm length computed from the number of base pairs in the short and long arm, respectively, and assuming 0.314 ± 0.13 nm/bp.

2.3.6 AFM imaging reveals conformational changes of tri-nucleosome arrays induced by epigenetic modifications

To study the effect of selected PTMs on nucleosome structure, we analyzed the configuration of tri-nucleosomes by extracting several structure parameters from AFM images. In first step, we used process images in SPIP and identified the tri-nucleosome samples (Supplementary Figure 5.12). Nucleosome positions are ordered from the nucleosome closest to the short tail to the one closest to long tail (referred to as N_1 , N_2 , N_3) and we extract the x and y positions of the nucleosome centers (Supplementary Figure 5.12). As a first geometric parameter to quantify tri-nucleosome conformations, we calculated the distance between the first nucleosome and the third, which we call the N_1N_3 -distance. In addition, we computed the inner angle α , defined as the angle between the lines connecting N_2 to N_1 and N_3 , using the formula $\alpha = \cos^{-1}\left(\frac{a \cdot b}{|a| \cdot |b|}\right)$ with a and b are two dimensional vectors of the nucleosome particles (Supplementary Figure 4.2D, $a = \overrightarrow{N_2N_1}$, $b = \overrightarrow{N_2N_3}$). Finally, we determine the radius of gyration defined by $R_g = \left(\frac{d_1^2 + d_2^2 + d_3^2}{3}\right)^{\frac{1}{2}}$, where (d_1 , d_2 , d_3) are the distances from the nucleosome positions to their center of mass (Supplementary Figure 5.12).

Peter Müller applied AFM imaging and image analysis to obtain distributions of the geometric parameters to quantify and compare the impact of the different PTMs (Figure 2.8). For each modification, we measured the radii of gyration as a parameter describing the overall nucleosome distances in the tri-nucleosome complex (Figure 2.8a,d,g), the distance

between the outer two nucleosomes (Figure 2.8b,e,h), and the angle at the inner nucleosome (Figure 2.8c,f,i). To facilitate a direct comparison of the impact of the nucleosome types, we smoothed histograms for a given parameter using a kernel density estimate (Figure 2.8a-i) and co-plot the resulting probability densities (Figure 2.8j-l).

We find that the radii of gyration, N_1N_3 -distances, and inner angles provide a highly consistent picture: The unmodified nucleosomes exhibit the most compact conformations, exhibiting narrow distributions, with the smallest mean values for all three parameters. Conversely, H4K5/8/12/16ac nucleosomes present the broadest range and largest average values, while H3K36me3 nucleosomes exhibit distributions for radii of gyration, N_1N_3 -distances, and inner angles that are intermediate between the other two nucleosome types (Figure 2.8j-l). Together, these data suggest that H4K5/8/12/16ac nucleosomes exhibit the least compact and most open conformations, while unmodified nucleosomes exhibit the most compact structures and H3K36me3 nucleosomes take on intermediate conformations. Comparing the mean values for radii of gyration, N_1N_3 -distances, and inner angles, we find statistically significant differences (assessed by two-sample *t*-tests) with unmodified nucleosomes being most compact and H4K5/8/12/16ac taking on the largest values, except for the radii of gyrations comparison between H3K36me3 and H4K5/8/12/16ac and the inner angle comparison between unmodified and H3K36me3, which are not significant (Figure 2.8p-r). In addition to comparing the overall distributions and their means, we looked at the subpopulations with open conformations, defined as having R_g , N_1N_3 -distance, or inner angle α values above a manually determined threshold (Figure 2.8m-o). The fraction of particularly open conformations increases, in almost all cases statistically significantly, in going from unmodified, to H3K36me3, and further to H4K5/8/12/16ac nucleosomes, further confirming the observations from the overall distributions (Figure 2.8m-o). In addition to comparing the means, we also compared the full distribution using Kolmogorov–Smirnov tests to compare the full distribution of R_g , N_1N_3 -distance, and inner angle α between the different variant nucleosomes (Table 2.1). We find statistically significant differences for all parameters (N_1N_3 -distance, R_g , and inner angle α) and for each pairwise comparison, except for the inner angle comparison between unmodified and H3K36me3. The AFM results are in line with magnetic tweezers observations that indicate more open and diverse conformations for H3K36me3 and H4K5/8/12/16ac. Interestingly, while the AFM results suggest that H4K5/8/12/16ac tri-nucleosomes adopt the most open conformations (Figure 2.5), the magnetic tweezers measurements see the difference in Δz steps > 10 nm between H3K36me3

and H4K5/8/12/16ac is within experimental error (Figure 2.5). The more open configurations for H3K36me3 compared to unmodified tri-nucleosome arrays are in line with the behavior of the constituent mononucleosomes. Previous work using a high-throughput AFM analysis approach to probe mononucleosomes found that H3K36me3 mononucleosomes have increased breathing activity, are almost 2-fold less likely to occupy the fully wrapped state and exhibit less anti-cooperativity for unwrapping from the respective ends compared to unmodified nucleosomes [167]. In contrast, the same assay found no difference between the conformations of H4K5/8/12/16ac and unmodified mononucleosomes, in stark contrast to our findings for tri-nucleosomes.

To be able to even more directly compare how mononucleosome conformations vary across the different PTMs under the conditions of our assay, We exploited the fact that in our tri-nucleosome samples there is a sub-population of molecules with only one nucleosome assembled (Supplementary Figure 5.13). Dr. Willem Vanderlinden analyzed this sub-population of mononucleosomes by tracing the DNA entry/exit angles (Supplementary Figure 5.13). From the analysis of the mononucleosome sub-population in our tri-nucleosome data, we find that H3K36me3 nucleosomes have statistically significant larger mean exit angles compared to unmodified and H4K5/8/12/16ac nucleosomes, while there is no significant difference between the unmodified and H4K5/8/12/16ac condition, in excellent agreement with the previous analysis using mononucleome samples assembled on shorter DNA with only one W601 positioning sequence [57].

Type1	Type2	Parameter	P-value
Unmodified	H3K36me3	R_g	1.2815e-06
Unmodified	H3K36me3	N_1N_3 -distances	0.0039
Unmodified	H3K36me3	Inner angle	0.1624
Unmodified	H4K5/8/12/16ac	R_g	5.5441e-15
Unmodified	H4K5/8/12/16ac	N_1N_3 -distances	2.5401e-15
Unmodified	H4K5/8/12/16ac	Inner angle	4.2401e-09
H3K36me3	H4K5/8/12/16ac	R_g	9.9286e-04
H3K36me3	H4K5/8/12/16ac	N_1N_3 -distances	5.6997e-06
H3K36me3	H4K5/8/12/16ac	Inner angle	2.0555e-05

Table 2.1: Pairwise comparisons by a two-sample Kolmogorov–Smirnov test between nucleosome types for radius of gyration (R_g), N_1N_3 -distance, and inner angle.

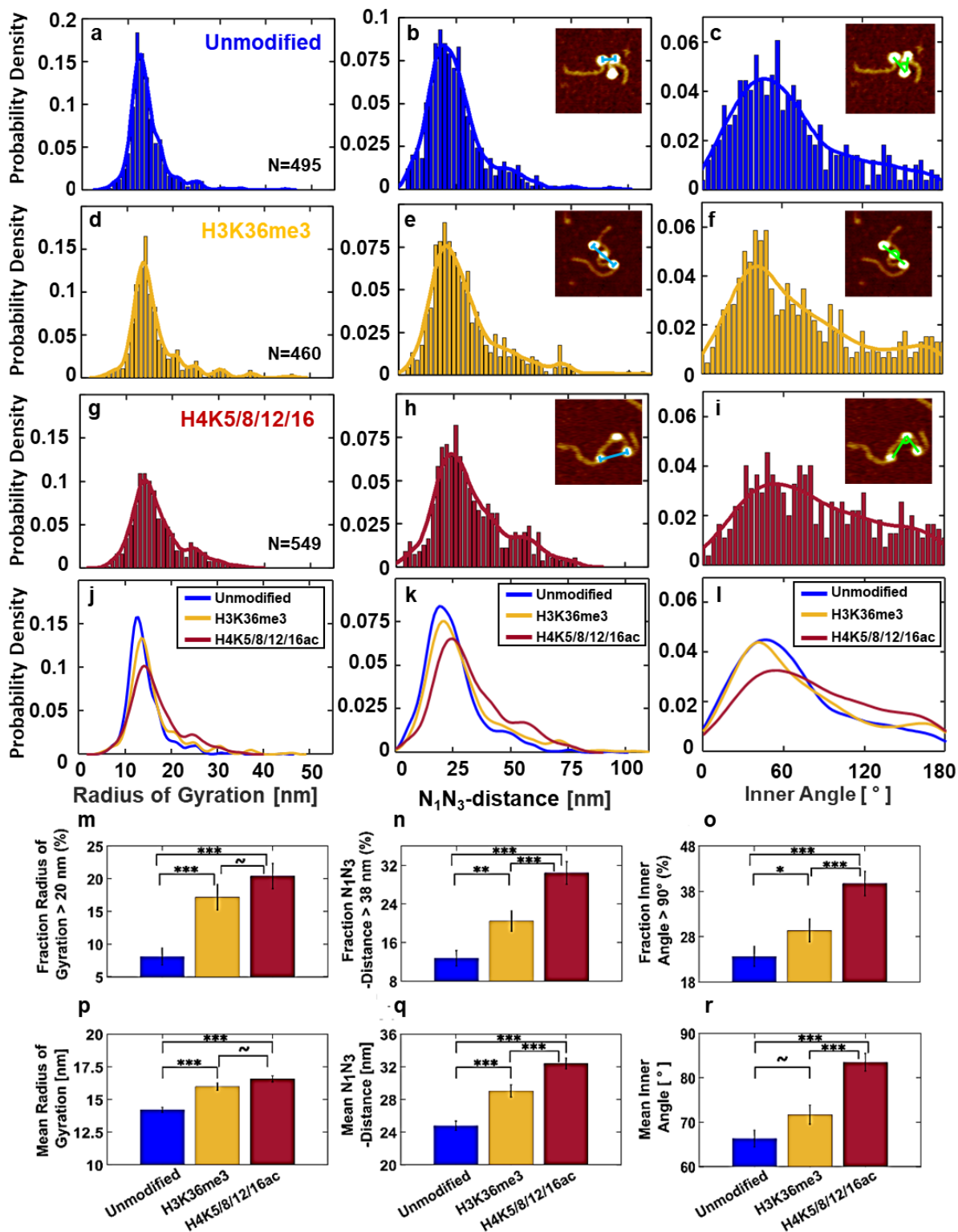


Figure 2.8: AFM imaging reveals the impact of H3K36me3 and H4K5/8/12/16ac PTMs on tri-nucleosome conformations. (a-i) Probability distributions for radii of gyration, N_1N_3 -distances, and inner angles determined from AFM imaging for unmodified (a-c), H3K36me3 (d-f), and H4K5/8/12/16ac (g-i) nucleosomes. Raw data are shown in the histogram. Solids lines are kernel density estimated. (j-l) show the kernel density estimates of the different nucleosome modifications co-plotted for each parameter for ease of comparison. The numbers of molecules analyzed for each condition are indicated in panels a, d, and g. The insets in panels b, c, e, f, h, and i show example AFM images of tri-nucleosome constructs with the N_1N_3 -distances (blue line) and inner angles (green line) indicated. (m-r) Quantitative comparisons of the distributions from panels (a-l). panels m-o show the fraction of particles exhibiting values larger than a given threshold for the different parameters as indicated in the y-axis labels for the different nucleosome types, i.e. the fraction of tri-nucleosomes adopting a more “open” configuration. Error bars indicate the counting error. Bars between the columns indicate the results of a two-tail two-sample proportion-test. (p-r) Mean values of the parameter distribution for the different nucleosome types. The bars between the columns indicate the result of a two-tail two-sample t-test. Error bars indicate the standard error of the mean. ~ not significant, * $p < 0.05$, ** $p < 0.01$, *** $p < 0.001$.

Together, the observations suggest that the acetylation of H4K5/8/12/16ac nucleosomes primarily affects nucleosome-nucleosome interactions and the open, more dynamic conformations of H4K5/8/12/16ac tri-nucleosome mostly occur due to a decrease in stacking and/or binding interactions between the nucleosomes, compared to unmodified and H3K36me3. Our experimental observations for H4K5/8/12/16ac tri-nucleosomes are in good agreement with molecular simulations that investigated histone tail acetylation dependence of the free energy landscape of tri-nucleosome and found that tri-nucleosomes with H4 acetylation have a larger R_g compared to unmodified nucleosomes and also reduce the contact between first and third nucleosomes mediated by the histone tails [168]. Our results support that H4-acetylation opens nucleosome array by reducing the inter-nucleosome interaction [169].

2.3.7 Effect of the ion atmosphere on tri-nucleosome conformations

Since chromatin structure is sensitive to the ionic environment [170-175], we performed control AFM imaging measurements using a different buffer composition and compared the structural parameters in the presence of different types of salt. It is well-known that Mg^{2+} can affect the compaction of chromatin [170, 173, 176, 177]. Mg^{2+} can help chromatin to turn from ‘beads-on-a-string’ into a 30 nm fiber *in vitro* [176] and Mg^{2+} and K^+ mixed environment seems important for the structure of heterochromatin formation [178]. Previous work by sedimentation velocity analytical ultracentrifugation on nucleosome arrays in

different mixed salt solution shows that the additions of Mg^{2+} leads to the precipitation of nucleosome arrays in solution with KCl or NaCl [172]. Therefore, we compared the effect of the mixed ionic Mg^{2+} and K^+ (2 mM $MgCl_2$ and 100 mM KCl; which is approximately the physiological concentration of ions intracellularly) and used as the buffer for the measurements described above, to the 200 mM NaCl buffer condition, the standard deposition buffer employed previously to characterize the effect of PTMs on single nucleosomes [167]. The results show that both unmodified tri-nucleosome and the acetylated tri-nucleosome adopt more compact structures in the presence of Mg^{2+} and K^+ (Supplementary Figure 5.14), in line with previously observed trends for chromatin. However, the effect of the change in ionic conditions is smaller than the effect of the PTMs on structure. In fact, the change induced by changing from the NaCl imaging buffer to the mixed conditions with Mg^{2+} was smaller, for all parameters analyzed, than the difference between unmodified and H4K5/8/12/16ac nucleosomes (Supplementary Figure 5.14). In conclusion, while we find that the addition of Mg^{2+} compacts tri-nucleosome arrays in agreement with previous findings, the observed influence of PTMs on the structure of tri-nucleosome is similar for different salt conditions and dominates under the conditions employed here.

3. Material and Methods

3.1 DNA constructs preparations

To prepare force calibration for MT measurement, we used a ~20.6 kb DNA construct. The preparation of DNA has been described previously [116]. Briefly, the DNA construct is generated by ligation of handles (~600 bp) with fragments labeled with multi-biotin and multi-digoxigenin, respectively, to an unmodified middle DNA segment with 20,666 bp in length.

To prepare DNA constructs for nucleosome array analysis, we prepared two different DNA constructs for the AFM and MT measurements, respectively. We used the plasmid pFMP218 [190] as template to produce DNA constructs with nucleosome positing sequences. pFMP218 is a custom-built plasmid (provided by Prof. Felix Müller-Planitz, TU Dresden, Germany) from a pUC18 backbone with 3 repeats of Widom 601 sequences inserted. [85]. The DNA construct for AFM measurements has a length of 896 bp. We prepared the DNA by PCR with Phusion Hot Start polymerase (follow the vendor's protocol) by using forward primer 5'-TAAGTTGGGTAACGCCAGG-3' and reverse primer 5'-GGCCGATTCATTAATGCAGC-3'. The final PCR product was purified with the QIAquick PCR Purification Kit (Qiagen).

For MT measurement, The final design yields a 2823 bp DNA molecule with a 2055 bp central unlabeled segment, flanked by two ~380 bp labeled regions. I generated the 2823 bp DNA construct from pFMP218 as linear template for subsequent assembly by PCR with Phusion Hot Start polymerase (following the vendor's protocol) using forward primer 5'-GCAGAAGTGGTCCTGCAACT-3' and reverse primer 5'-CCGGATCAAGAGCTACCAAC-3'.

Functionalized handles (the “megaprimers”; Figure 2.1a) were obtained by PCR amplification. I tested both Taq polymerase (New England Biolabs (NEB), Ipswich, MA USA) and KOD Hot Start polymerase (Novagen, Darmstadt, Germany) to prepare the functionalized handles and found both to give good yields of functionalized DNA product (Supplementary Figure 5.3). For both polymerases, I ran PCR reactions with added biotin-16-dUTP or 5-DBCO-(PEG)4-dUTP (Jena Biosciences GmbH, Jena, Germany), respectively.

For Taq polymerase, the PCR reactions used 0.3 μ M forward primer 5'-GCAGAAGTGGTCCTGCAACT-3', 0.3 μ M reverse primer 5'-CGCCGCATACACTATTCTCA-3', 6 ng template DNA, and different amounts of biotin-16-dUTP (0.16, 0.08, or 0.04 mM final concentration) in 20 μ L 1 x Taq Master Mix (which contains a final concentration of 0.2 mM of each unmodified dNTP). The other PCR solution contains 0.3 μ M forward primer 5'-CCGCTTACCGGATACCTGTC-3', 0.3 μ M reverse primer 5'-CCGGATCAAGAGCTACCAAC-3', 6 ng template DNA, and different amounts of 5-DBCO-(PEG)4-dUTP (0.16, 0.08, or 0.04 mM final concentration) in 20 μ L 1 x Taq Master Mix.

For KOD Hot Start polymerase, I followed a previous protocol [148]. I used the same DNA template and primers as for Taq polymerase and incorporated labeled dUTPs by replacing dTTPs in the PCR reaction mix [191] using either 25% or 50% biotin-16-dUTP or DBCO-(PEG)4-dUTP (the final concentrations are 0.05/0.15 and 0.1/0.1 mM modified dUTP/unmodified dTTP), respectively.

The functionalized PCR products are subsequently used as megaprimers to amplify the desired DNA substrate. I used KOD Hot Start polymerase for this PCR reaction. Instead of following the vendor's protocol, I changed the reaction conditions to optimize the purity and yield of the target DNA (Supplementary Figure 5.4). My final protocol uses KOD Hot Start polymerase with a reaction solution containing 1.5 mM MgCl₂, 0.16 mM x 4 dNTP, 1x KOD Hot start buffer, 7.5% DMSO (New England Biolabs), 200 ng forward megaprimer, 200 ng reverse megaprimer, 50 ng linear template from pFMP218, and 0.5 μ L (1 unit/ μ L) KOD Hot start polymerase in 100 μ L reaction volume. I used the following PCR cycling parameters: Initial denaturation at 95 °C for 2 min; 35 cycles of denaturation at 95 °C for 20 s, annealing at 60 °C for 10 s, and elongation at 70 °C for 65 s. The final cycle was followed by extension at 70°C for 1 min. The PCR products were purified with the QIAquick PCR Purification Kit (Qiagen, Hilden, Germany) after each step of PCR amplification. One reaction with a final volume of 100 μ l typically produces 0.6 μ g DNA, of which approximately 70% is the correctly assembled megaprimer DNA (Supplementary Figure 5.4e). This amount of product is similar to a previously described megaprimer protocol using digoxigenin-labeling [148] and significantly higher than previous non-PCR based protocols [123, 147].

I also tested PCR reactions using a 5x smaller reaction volume and 5x higher final concentrations of megaprimers and template DNA, using 10% DMSO and 1x KOD Hot start

polymerase MasterMix (Novagen, Darmstadt, Germany) (Supplementary Figure 5.5). The smaller final volume facilitates downstream processing and the higher megaprimer concentration has been suggested to increase yield [192, 193]. While the PCR reactions at higher concentrations yield functionalized DNA constructs, I find more off-target products (Supplementary Figure 5.5) and greater variability in yield. Therefore, I recommend the reaction described above with a final reaction volume of 100 μ L.

3.2 Magnetic tweezers setup

We experiment on a home-built MT setup as described previously. Two magnets (5 x 5 x 5 mm³; Supermagnete) with a 1 mm gap in vertical configuration [119] are placed in a vertical configuration on a motorized arm. We use a DC- motor (M-126.PD2, P1, Germany) to control the distance between magnets and the flow cell as well as a rotational motor (C-150. PD motor with C-863.11-Mercury controller, Physik Instrumente) to control the magnets' rotation. An LED (69647, Lumitronix LED Technik GmbH, Germany) is used for illumination. We use a 40x oil-immersion objective (UPLFLN 40x, Olympus, Japan) and a CMOS sensor camera with 4096 x 3072 pixels (12M Falcon2, Teledyne Daisa, Canada) to image a field of view of 400 x 300 μ m². The objective is mounted on a piezo stage (Pifoc P726. 1CD, PI Physikinstrumente) to build a look-up table (LUT) for tracking the bead z-position. With a step size of 100 nm, the LUT is generated over a range of 20 μ m. Set up control and bead tracking use Labview routines described previously Cnossen et al. (36). The flow cell outlet is connected to a pump to handle fluid.

3.3 Flow cell preparation for magnetic tweezers force spectroscopy calibration

Two kinds of flow cells are built for force calibration or nucleosome array probing measurements, respectively. The flow cells are built from two coverslips (24 x 60 mm, Carl Roth, Germany). The bottom coverslip is functionalized using (3-Glycidoxypropyl) trimethoxysilane (abcr GmbH, Germany) or treated with 2% APTES to generate an aminosilanized surface. After that, the functionalized coverslip is incubated with 100 ml of a 5000x diluted stock solution of polystyrene beads (Polysciences, USA) in ethanol (Carl Roth, Germany) to serve as reference beads. The top coverslips with two 1 mm radius holes as openings are glued to the bottom functionalized coverslip by a single layer of melted

Parafilm. These immobile surface-bound beads serve as reference beads for drift correction. The bottom coverslip was aligned with a pre-cut parafilm and a top coverslip with two small holes for inlet and outlet. Then the assembled flow cell was baked at 80°C for 1 min.

3.4 Measurement of drift correction and Allan deviation

The preparation of flow cell involves the incubation of 1 μm diameter polystyrene reference beads to attach to the surface of the bottom slide. After preparation of the flow cell with reference beads, I flush the flow cell with PBS buffer. I record the z-positions of surface-attached beads. I then subtract the z-position of one bead from another surface-attached bead, to determine the tracking precision. Traces are recorded for ~ 20 min at 58 Hz acquisition frequency. To understand the tracking limit of MT, I use Allen deviation (AD) to calculate the resolution [109]. The theory of Allen variance technique is closely related to signal averaging. Beads tracking is affected by Gaussian noise (fluctuation) with a variance of σ^2 . Repeating the measurement N times and averaging the measured value help reduce the noise. Thus, by averaging more samples, $\sigma_{avg}^2 = \frac{\sigma^2}{N}$, and the variance can be reduced. However, this application assumes that the noise sample are not correlated with each other. Drift can cause correlation of each signal and then decrease the effectiveness of signal averaging. Therefore, σ_{avg}^2 can even increase above certain value of N. AD is a technique used to determine how many samples should be averaged to minimize the noise and to determine the spatiotemporal resolution of tracking algorithms [135, 179]. To calculate AD, I divide the time series measurements into multiple intervals. Each interval has certain amount of samples and the intervals overlap with each other. The AD of a particle position along the z-axis is defined as follows:

$$\sigma_{AD}(\tau) = \sqrt{\frac{1}{2} \langle (\overline{z_{\tau,j+1}} - \overline{z_{\tau,j}})^2 \rangle} \text{ with } \overline{z_{\tau,j}} = \frac{1}{\tau} \int_{\tau(j-0.5)}^{\tau(j+0.5)} z(t) dt$$

Where τ defines the time between consecutive samples and the time over which the sample is average. Therefore, the AD is one-half the average difference in position between consecutive intervals of duration τ .

3.5 20.6 kbp DNA measurement preparation

To perform the measurements for force calibration, a flow cell functionalized with (3-Glycidoxypropyl) trimethoxysilane (abcr GmbH, Germany) is incubated with 100 μL of 200 mg/mL anti-digoxigenin (abcam, Germany) in 1 x PBS (phosphate-buffered saline, Roche, Switzerland) for at least 1h. After that, the flow cell is rinsed with 800 μL PBS to flush away non-binding anti-digoxigenin. To avoid non-specific interaction, 100 μL 250 mg/mL of bovine serum albumine (Carl Roth, Germany) in PBS is incubated in flow cell for 1 h and followed by the rinse of 800 mL PBS. In the end, the DNA-beads solution is flushed into flow cell. To let ~20.6 kbp DNA attach to magnetic beads, 1 μL picomolar ~20.6 kbp DNA stock solution is mixed with 13 μL 2.8 μm diameter streptavidin-coated M270 in 200 μL PBS buffer (Thermo Fisher Scientific, Germany) beforehand. M270 beads are used for both force calibration and the further measurement of nucleosome arrays. To calibrate the magnet distance-to-force relation, I recorded the transverse fluctuations of the beads at different magnet separations and analyzed the Allan variance (AV) of the transverse fluctuations to quantify the force at each magnet position.

3.6 Magnetic tweezers force calibration

As described in Introduction 1.5, the force exerted by MT is given by $\vec{F} = \frac{1}{2} \vec{\nabla}(\vec{m} \cdot \vec{B})$, where \vec{m} is the induced magnetic moment of the bead in the external magnetic field \vec{B} . The applied force F can be calculated from the horizontal bead fluctuation $\langle \delta x^2 \rangle$. $F = \frac{k_B T l}{\langle \delta x^2 \rangle}$ according to the equipartition theorem: $F/l \cdot \langle \delta x^2 \rangle = k_B T$, where T is the temperature, l as the extension of DNA nucleic acid and k_B is the Boltzmann constant. The horizontal bead fluctuation is related to Brownian motion, which defines a bead's movements in a harmonic trap with associated Langevin equation.

$$m \cdot \ddot{x}(t) + \gamma \cdot \dot{x}(t) + k \cdot x(t) = F_{therm}$$

where $x(t)$ is the position of the particle as a function of time, m is the inertial mass, k is the trap stiffness attribution to applied force F , F_{therm} the thermal force on the particle by random collisions with water molecules, γ the friction coefficient defined as $\gamma = 6\pi\eta R = k_B T/D$, with D as the beads diffusion constant, η the dynamic viscosity. The inertial term is negligible since the loss of kinetic energy through friction takes place on very

small time scale m/γ . Therefore, it yields a well-known Power spectrum density (PSD) of Brownian motion in frequency domain f [180]:

$$P(f) \equiv |X(f)|^2 = \frac{k_B T}{2\pi^2 \gamma (f^2 + f_c^2)}$$

The $f_c = k/2\pi\gamma$ is defined as corner frequency, an indication of the highest frequencies in the system. Fitting this model to the measured PSD yields k and f_c . Those two parameters can be used to calculate the applied force F and bead radius R as a control parameter for the fit which is known beforehand. To get more accurate and precise force, we chose Allan Variance (AV) model approach to find the right forces. AV, as a time-domain measure, it is half of the ensemble-averaged variance of the difference between two consecutive samples of position. AV is defined by the square of AD while a particle positions along x-axis. It plays a role as autocorrelation over averaged points. Wiener-Khinchin theorem can be used to related PSD with autocorrelation and variance. Therefore, previous $P(f)$ can be converted into the following model for the AV [109, 181]:

$$\sigma^2 = \frac{2k_B T \alpha}{k^2 \tau} \left(1 + \frac{2\gamma}{k\tau} e^{-\frac{k\tau}{\gamma}} - \frac{\gamma}{2k\tau} e^{-\frac{2k\tau}{\gamma}} - \frac{3\gamma}{2k\tau} \right)$$

3.7 Nucleosome reconstitution

Nucleosomes were assembled on the labeled DNA construct (2823 bp DNA) obtained using the megaprimer protocol outlined in the previous section for MT measurements. Unlabeled DNA construct (895 bp) obtained by PCR as described in the previous section is used for AFM imaging. Recombinant human histone octamers were purchased from EpiCypher (Durham, North Carolina). Samples were prepared via salt gradient dialysis following the protocol described previously [182]. In brief, containing 2.8 – 3 μg of 2823 bp or 895 bp DNA and histone octamer (ratio of histone octamer to Widom 601 is 1 to 1-1.5) in 30 μL high-salt buffer (10 mM Tris-HCl, pH 7.6, 1 mM EDTA, 0.1% (w/v) Triton-X100, and 2 M NaCl) were incubated in a dialysis chamber (Slide-A-Lyzer MINI Dialysis Devices, 3.5K MWCO, Thermo Scientific) at 4°C. Then, the dialysis chamber was transferred to a glass beaker with 300 mL high-salt buffer and 300 μL β -mercaptoethanol. 3 L low-salt buffer (10 mM Tris-HCl, pH 7.6, 1 mM EDTA, 0.1% (w/v) Triton-X100, and 50 mM NaCl) and 300 μL β -mercaptoethanol were transferred to the high-salt buffer overnight at 4°C (at least 16 h). The buffer exchange was achieved with a peristaltic pump to slowly introduce the low-

salt buffer into the beaker with the dialysis chamber. Finally, we placed the dialysis chamber into 1 L low-salt buffer with 300 μ L β -mercaptoethanol for 1-2 h.

3.8 DNA or polynucleosome anchoring for magnetic tweezers experiments

Following flow cell with aminosilanized surface assembly, 50 mM each of azide-(PEG)₄-NHS (Jena Biosciences GmbH, Jena, Germany) and methyl-(PEG)₄-NHS (Life technologies) in 1 x PBS were introduced and incubated for 1 h [128]. To prepare the solution, 100 mg azide-(PEG)₄-NHS or methyl-(PEG)₄-NHS were dissolved in 100 μ L DMSO, respectively, to prevent hydrolysis of the NHS ester during storage at -20°C . I added 1 x PBS buffer to adjust to a final concentration of 100 mM for both azide-(PEG)₄-NHS and methyl-(PEG)₄-NHS, respectively, and then mix equal volumes. The mixture was quickly filled into the incubation chamber for surface passivation to avoid hydrolysis. We found that the addition of salt in HEPES buffer (10 mM HEPES, pH 7.6) is necessary to immobilize DNA or polynucleosomes on the surface of the flow cell. Therefore, I mixed my DNA or polynucleosome sample in measurement buffer MB1 (MB1; 10 mM HEPES pH 7.6, 100 mM KCl, 2 mM MgCl₂, 0.1% Tween-20). Next, the flow cell was flushed with 500 μ L MB1. DNA or polynucleosomes were dissolved in 100 μ L MB1, flushed into the flow cell and incubated for 1 h. Afterwards, I rinsed with MB2 buffer, which consists of MB1 supplemented with 0.1% (w/v) bovine serum albumin (Carl Roth, Germany). The flow cell was rinsed with MB2 to flush out unbound DNA or nucleosomes. Subsequently, I flowed in 1% casein for nucleosome samples or 1.5% (w/v) bovine serum albumin for DNA samples in MB2 into the flow cell, incubated for 1 h to minimize nonspecific interactions, and then flushed with MB2. Finally, I flushed in streptavidin-coated M270 beads (Dynabeads, Invitrogen) and incubated in the flow cell for 10 min. Subsequently, unbound beads were flushed out with 2 mL MB2.

3.9 AFM sample preparation, imaging, and analysis

We followed the previously published protocol to prepare samples for AFM imaging [24, 167, 183-185]. The reconstituted nucleosomes were incubated in 100 mM KCl, 2 mM MgCl₂, and 10 mM Tris-HCl, pH 7.6, for 1 min on ice and then deposited on poly-L-lysine (0.01% w/v) coated muscovite mica for 30 s, followed by 20 ml Milli-Q water rinsing and

drying with a gentle stream of filtered N₂ gas. AFM imaging was performed on a Nanowizard Ultraspeed 2 (JPK, Berlin, Germany) with AFM cantilevers 240AC-NA (Opus) in air. All AFM images were acquired in tapping mode at room temperature. The scans were recorded at 1 Hz line frequency over a field of view of 3 μm x 3 μm at 2048 x 2048 pixels. For image processing, Scanning Probe Image Processor (SPIP v6.5.1; Image Metrology) was employed. Image processing involved background correction by using global fitting with a third-order polynomial and line-by-line correction through the histogram alignment routine.

3.10 Model for the step size distributions

When subjecting the megaprimer-DNA tethers to constant forces, we observe stepwise increases in the tether length before tether rupture. Here we describe a simple, minimal model to account for the experimentally observed step size distribution. Since the covalent linkages used in our protocol are expected to be very force stable, we assume that only the biotin-streptavidin bonds dissociate under the constant loads exerted in the magnetic tweezers assay and cause the observed steps on the time scale of our experiments [122, 186]. As a starting point, we used the DNA sequence for the biotin megaprimer assembly. In our reaction, a fraction of the thymidine moieties in the DNA sequence is replaced by biotinylated uridine. However, it is important to note that not all thymidine moieties in the sequence will form bonds to the magnetic bead since i) the PCR reaction contains a mix of labeled and unlabeled nucleotides, ii) the polymerase might incorporate labeled and unlabeled nucleotides with different probabilities [152, 187], iii) not all labeled nucleotides will bind to a streptavidin on the bead due to steric constraints, amongst other reasons. We assume that the incorporation and subsequent binding to streptavidin of functionalized nucleotides are random and occurs with probability P_{label} that we treat as a fitting parameter. We used a Monte Carlo approach whereby PCR reactions are simulated by randomly incorporating labels at T positions in the sequence with probability P_{label} . To convert the simulated label positions in the sequence to step sizes, we further assumed that streptavidin can only bind labels that are at least 10 bp apart, corresponding to a minimal physical distance of ~3 nm, since it is unlikely that two streptavidin tetramers [188] would bind within one helical turn. Simulated step size distributions are obtained by converting the distances between subsequent incorporated and streptavidin bound labels from bp to nm using a conversion factor of 0.34 nm/bp, corresponding to the crystallographic length of

double-stranded DNA. The experimentally determined step size distribution is compared to the experimental data using an unweighted χ^2 -criterion. In addition, we compare the mean step sizes of the simulated and experimental data.

4. Discussion

Magnetic tweezers are powerful instruments for a broad range of single-molecule measurements and applications. Over the decades, magnetic tweezers have been developed to provide high-resolution and a large force range to dissect the dynamics and mechanical responses of macromolecules [122, 136, 189]. Besides, we can manipulate macromolecules by stretching or twisting them with magnetic tweezers [106, 140, 179, 190-192]. Furthermore, the tweezers generate a nearly homogenous force field over large distances which, combined with camera-based detection, helps to track and manipulate multiple molecules in real-time [122].

The mechanical properties of DNA have been studied over the past decades. DNA stores the genetic information and the human genome is composed of three billion base pairs with more than one-meter length in a stretched configuration. To compact DNA into a micrometer-sized cell nucleus, DNA forms chromatin by wrapping around histones. Therefore, the thesis mainly focuses on the properties of variant nucleosome arrays.

To study how DNA forms nucleosomes, the basic unit of chromatin, and how post-translational modification affects the dynamics of nucleosomes, a robust tether should provide stability for probing nucleosome array samples. One of the commonly used attachments of nucleosome samples is to synthesize the DNA with multiple biotin and digoxigenin-labeled at both DNA ends respectively. However, the non-covalent bonds forming between digoxigenin (dig) on the DNA and anti-digoxigenin antibodies on the flow cell surface provide weak interactions. Thus, tethers are not stable and easy to rupture under high force. Besides, the preparation of DNA constructs for magnetic tweezers is time-consuming and low-yield. Here, I present a new method for preparing functionalized DNA constructs for single-molecule measurements that combines the benefits of ligation-free, high-yield megaprimer-based assembly and covalent attachment of DNA to the surface for very high force stability. My tethers are torsionally constrained and thus enable torque and twist measurements. In addition, they provide exceptionally high force stability, and I find an average lifetime of (70 ± 3) h at 45 pN using regular, commercially available streptavidin-coated beads. The high yield of correctly labeled DNA enables efficient nucleosome reconstitution by standard salt gradient dialysis. I anticipate

that my methodology will enable a range of measurements on DNA and nucleoprotein complexes that benefit from high yield and force stability.

PTMs are a key factor that affects the structure and dynamics of chromatin fibers in the cell. They can have manifold effects on chromatin structure, such as entry site unwrapping, nucleosome destabilization, formation of active or repressive compartments, and histone-histone destabilization [26, 40, 59]. Here I investigate the conformations of post-translational modified nucleosomes using two single-molecule techniques: atomic force microscopy imaging and magnetic tweezer force spectroscopy. Specifically, I study the effects of the post-translational modifications H3K36me3 and H4K5/8/12/16ac on tri-nucleosome array structure and mechanical stability. I use tri-nucleosomes, which have been reported to be the smallest cluster size found in cells [47], as a tractable model system for comparison of different PTMs on nucleosome arrays that build in complexity on our previous work on mononucleosomes in isolation [167].

H3K36me3 and H4K5/8/12/16ac are known as markers of active regions in chromatin. Previous high-throughput AFM image analysis has shown that H3K36me3 mononucleosomes exhibit partial unwrapping and more open conformations compared to unmodified mononucleosomes, likely due to the position of the H3K36me3 mark at the DNA entry/exit site of the nucleosome [29, 92]. We confirmed this finding by analyzing the mononucleosome sub-population of our tri-nucleosome samples and found significantly higher exit angles for H3K36me3 nucleosomes compared to unmodified and H4K5/8/12/16ac species. It has been found that PTMs at the entry/exit region enhance partial DNA unwrapping [26, 167, 193]. The results here suggest that the increased unwrapping induced by the H3K36me3 seen in mononucleosomes propagates to higher order nucleosome assemblies, as we observe more open and loose conformations for H3K36me3 compared to unmodified nucleosomes both by AFM imaging and magnetic tweezers force spectroscopy. The findings are in line with previous simulations that predict nucleosome breathing to affect their higher order structures, to result in more heterogeneous nucleosome-nucleosome contacts [194].

The H3K36me3 modification is associated with DNA repair, alternative splicing, and transcription. It is enriched in the region of actively transcribed genes [195-197]. The finding that H3K36me3 leads to more open nucleosome array structures highlights a mechanism of how it

can facilitate access to histone-binding proteins, e.g. of protein carrying a PWWP domain [198] that interact with the H3K36me3 mark and regulate gene transcription [195, 197].

Interestingly, the H4K5/8/12/16ac modification causes no significant changes in mononucleosome structure compared to unmodified mononucleosome [167], yet it leads to the most open and extended tri-nucleosome structures as judged by the AFM imaging results, of the three variants studied. This is consistent with the view that the H4K5/8/12/16ac mark, which is known to be associated with open chromatin conformations [78, 199], reduces nucleosome-nucleosome interactions and stacking. The fact that H4K5/8/12/16ac tri-nucleosomes are more open and less compact than the H3K36me3 constructs suggests that nucleosome-nucleosome interactions can be more important and overrule nucleosome breathing and outer turn unwrapping.

In vitro work reveals that H4K5/8/12/16ac inhibits liquid-liquid phase separation, likely due to the decrease of multivalent interaction with other nucleosomes [37]. Our experiments are consistent with this observation of reduced liquid-liquid phase separation by H4K5/8/12/16ac nucleosomes, as we observe reduced nucleosome-nucleosome. In contrast, the inner turn unwrapping appears to not be influenced by the investigated PTMs, consistent with the view that their influence is limited to the entry-exit site and tail regions.

Chromatin architecture is more open at transcriptionally active sites [200]. Here I demonstrate that epigenetic marks associated with active transcription can decrease chromatin compaction directly – not only by reducing nucleosome-nucleosome interactions but also by outer turn wrapping affinity. Taken together, my work suggests that the combination of force spectroscopy and AFM imaging can provide a comprehensive understanding of how different PTMs affect nucleosome assemblies and we anticipate our approach to be powerful to study the effect of other PTMs in the future.

Perspective

I built a robust nucleosomal positioning sequence (with 3 x Widom sequence) DNA tether for magnetic tweezers measurement, which will be useful to apply to the investigation of other DNA binding proteins or enzymes. It could be possible to generate a DNA construct with >3 x Widom sequences or different lengths of linker DNA by using the megaprimer assembly protocol to

build a complex nucleosome array system on magnetic tweezers. Here, I apply the approach to the study of different variant nucleosome structures and the results provide interesting views of H4K5/8/12/16ac and H3K36me3 regulation of nucleosome array. We can build higher-order structures of those different PTMs to look into the mechanism of nucleosome-nucleosome stacking and breathing. Previous research reveals that wild-type histone chromatin fibers with 167- and 197-bp NRLs perform different structure transitions of nucleosome rupture, which have been quantitatively analyzed by magnetic tweezers measurement [101, 103]. We expect to build up a chromatin fiber to further look into the model of nucleosome-nucleosome stacking among different PTMs.

In the nucleus, chromatin is hierarchically organized at different length scales. Over the past year, phase separation has been discussed as a mechanism to form compartmentalization in nucleus [37, 40, 200, 201]. In particular, liquid-liquid phase separation (LLPS) can be driven by various interactions between chromatin and other factors. It is known that H4K5/8/12/16ac is unfavorable to the formation of liquid-liquid phase separation [37, 194, 202]. It will be interesting to look into how H3K36me affects liquid-liquid phase separation in the future.

H1 and H5 are well-known linker histones that cause chromatin structure more compact. Previous studies have applied single molecule force spectroscopy on H1 to chromatin fibers [99, 203, 204]. Different subtypes of H1 link to cell differentiation and cell cycle [205-207]. We can further look into the influence of different subtypes of H1 on our tri-nucleosome array by dissecting nucleosome conformational changes. Besides, PTMs also interact with nucleosome “readers” by providing binding platforms to further regulate transcription. H3K36me3 nucleosome interacts with proteins containing PWWP domain, e.g. LEDGF, HDGF, NDF1, HPR3, and so on to regulate transcription [195-197, 208]. In the future, we can investigate how those associated proteins change nucleosome structural dynamics while binding to the PTMs by using our magnetic tweezers assay.

5. Supporting Information

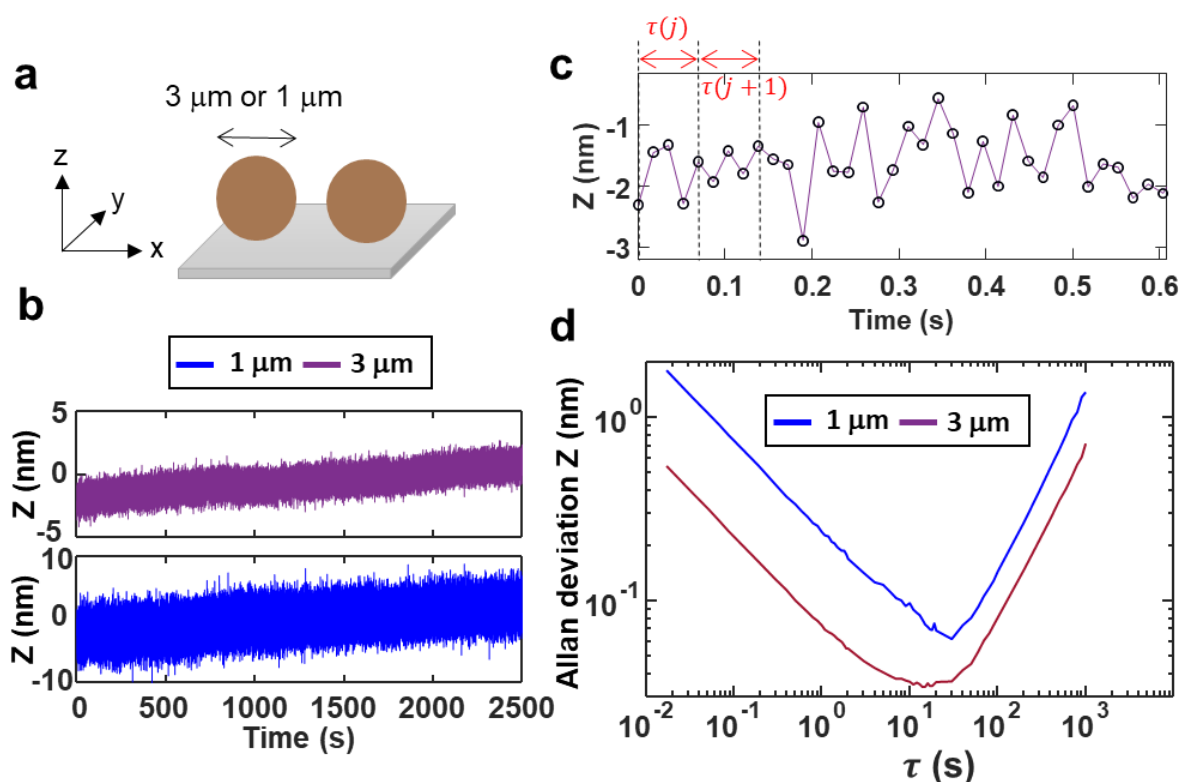
5.1.1 Force calibration for magnetic tweezers

Magnetic tweezers make it possible to investigate the behavior of structural transitions and the dynamics of individual biological molecules in solution in real time. In recent years, magnetic tweezers have been applied widely to the study of different biopolymers with insight into kinetics and the underlying mechanochemistry [105, 209, 210]. Magnetic tweezers can apply both stretching forces and torques to biological molecules by manipulating the movement of magnets [189-191]. To perform MT precisely and accurately, calibration is required to determine the applied force. Force calibration relies on video tracking to measure the position of a bead [139, 143, 211]. By comparing the measured Brownian motion of the bead, we can obtain the related applied force. However, due to temperature fluctuations, electronic noise, mechanical drift, and so on, drift is often a problem and causes the sensitivity and resolution of MT to be limited [109, 212]. Here, I performed experiments to calibrate the forces in magnetic tweezers and also analyzed the drift to estimate the spatiotemporal resolution under the influence of instrumental drift.

5.1.2 Spatiotemporal resolution by Allan deviation computing

Instrument drift is a general problem in high-resolution single-molecule measurements. To compensate for instrument drift, generally, I track at least two different beads, one that is tethered to the molecule of interest and one that is stuck to the surface as a reference bead. By subtracting the reference bead position, I can correct for drift and other noise sources. However, some drift components and other noise sources, in particular tracking noise, are not removed by reference subtraction. I use Allan deviation to quantify the tracking resolution of our setup. Allan deviation (AD) is a statistical analysis tool to identify the various noise types in a signal and provide the spatiotemporal resolution [212]. AD is defined as square root of one-half the average difference in position between adjacent intervals of length τ over all intervals of length τ [109, 135]. We can quantify the magnitude of noise components by tracking reference beads that are attached to the surface without undergoing Brownian

motion. I incubated 3 μm or 1 μm polystyrene beads on the surface of flow cell and track their positions (Supplementary Figure 5.1a). I subtract the position signals of two randomly selected stuck beads and calculate the AD for different intervals of length, τ , from 0.02 s to 1000 s (see Material and Method, Supplementary Figure 5.1a,b). Both reference subtracted traces of 3 μm and 1 μm show that the z-position gradually increases overtime (Supplementary Figure 5.1b) after reference subtraction.



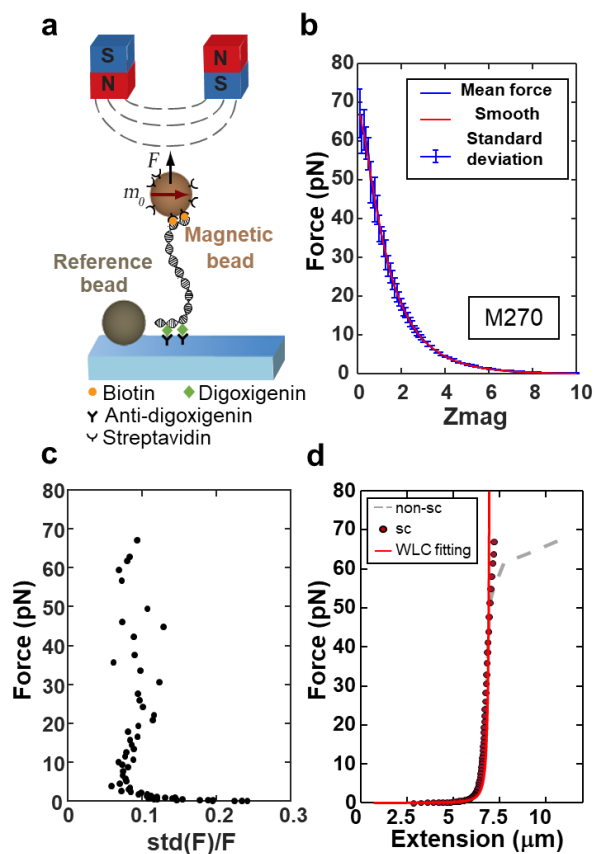
Supplementary Figure 5.1: Allan deviation to analyze the spatiotemporal resolution of different size beads. (a) Schematic of the experiment (b) Time traces of the Z-position of 1 μm and 3 μm surface-attached bead after reference subtracted. (c) Zoom of (b) to illustrate the calculation of Allan deviation (material and method) (d) Allan deviation of the Z axis vs. time of the measurement τ (s).

It becomes apparent that the measurement accuracy is affected both by drift and by the bead sizes. The fluctuations of the 1 μm bead traces are larger than for 3 μm bead. By plotting AD vs. τ , I find that 3 μm beads achieve AD ~ 0.6 nm at the lowest τ . As τ increasing to 10 s, the AD decreases to the lowest value: ~ 0.03 nm, and then increases again (Supplementary Figure 5.1d). This increase at long times is due to slow instrument drift. The results for 1 μm beads

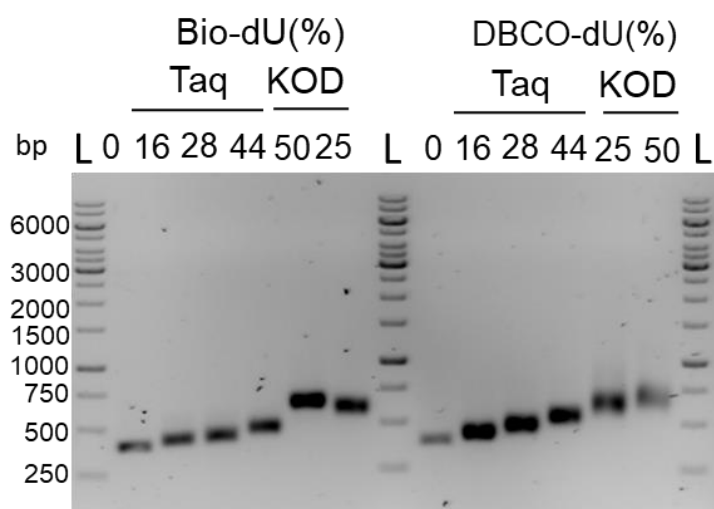
show similar trends, however with a resolution of ~ 2 nm at the lowest τ and the best resolution of ~ 0.07 nm again at $\tau = \sim 10$ s. Our MT set-up can achieve the best resolution of 0.03 nm at 10 sec (Supplementary Figure 5.1d). The data clearly indicate that larger beads provide a higher spatiotemporal resolution indicated by the lower AD for a given averaging time, in agreement with previous work [135, 136] and consistent with Mie theory, where the scattered light intensity is proportional to the bead area ($I_{\text{scatt}} \propto R^2$) and the Allan deviation is proportional $1/\sqrt{I}$ giving reduction of $\text{AD} \propto 1/R_{\text{bead}}$. Consistent with this prediction, the AD is ~ 3 -fold lower for the larger bead in the range $\tau \sim 0.1 - 10$ s, where tracking errors dominate. For $\tau > 10$ s, the AD increases again (Supplementary Figure 5.1d), which is to be expected due to drift at long times that is only imperfectly removed by subtracting a reference bead signal.

5.1.3 Force calibration results

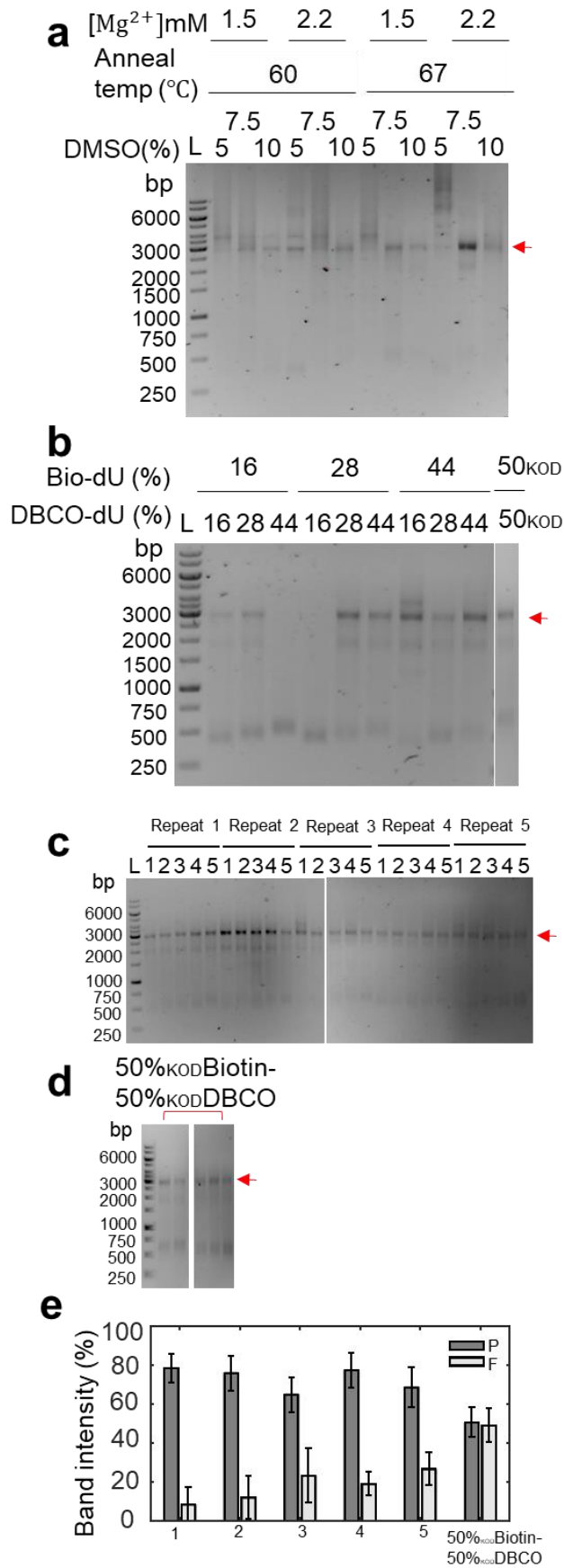
To get the force value corresponding to different magnet position, I attached ~ 21 kbp DNA on M270 and then immobilized the DNA-bead complex to the flow cell (Materials and Methods, (Supplementary Figure 5.2a)). Then I record the traces in x-y-z while moving the magnets to different positions from $Z_{\text{mag}} = 0.1$ mm to 10 mm, defined as the distance between the magnets and the top surface of the flow cell. The two magnets generate a horizontal magnetic field along x-axis above the flow cell. Therefore, I analyze the fluctuation of x-axis: $\langle \delta x^2 \rangle$, with the correction of finite acquisition frequency of the camera and mechanical drift correction by Allan variance. The results show that magnetic force decreases exponentially as Z_{mag} increases (Supplementary Figure 5.2b). The force range achieved using M270 beads is up to ~ 70 pN. I analyze the relative error, i.e. the standard deviation of the forces from the experimental data of different beads divided by the mean force ($\text{std}(F)/F$), and find that the relative error is approximated to 10% (Supplementary Figure 5.2c), consistent with the previously reported bead-to-bead variation of 5-10% [139]. The force extension curves obtained from M270 beads are well described by the extensible worm-like chain model (WLC) [114], with contour length: ~ 7 μm and persistence length 45 nm (Supplementary Figure 5.2d).



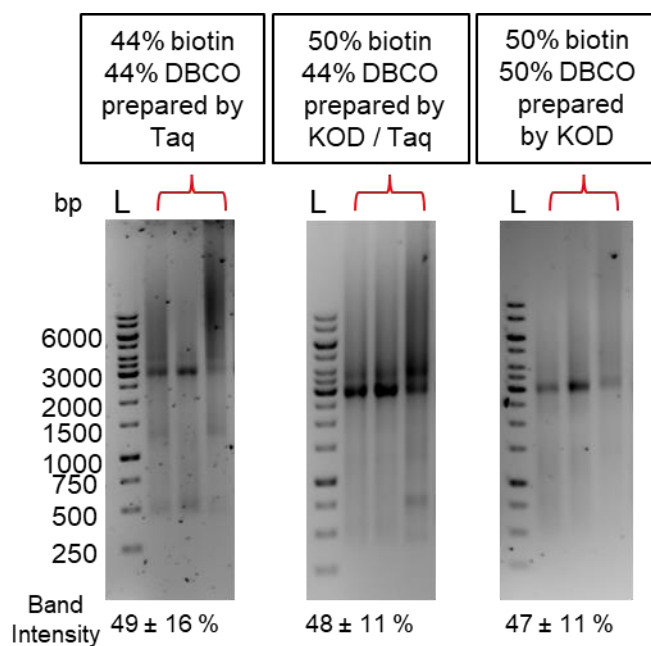
Supplementary Figure 5.2: Force calibration by utilizing ~21 kbp DNA (a) Schematic of the Magnetic Tweezers set-up with two magnets ($5 \times 5 \times 5 \text{ mm}^3$; Supermagnete) with a 1 mm gap in vertical configuration [139] are placed in a vertical configuration on a motorized arm. (b) Force calibration for M270 magnetic beads ($N = 10$) as a function of the distance of the magnets to the flow cell. To get the function of the distance of magnets to the flow cell, we apply spline interpolation to our data. (c) The $std(F)/F$ vs. force, shows that the force calibration has roughly 10% relative error, which is within the range of error that is commonly accepted in force measurements [139, 190, 211, 213]. $std(F)/F$, dividing standard deviation of force by force from panel (b), is defined as relative error. (d) Force extension curve obtained from M270 beads with extensible WLC model fitting [114]. M270 beads can exert forces up to ~70 pN in our setup.



Supplementary Figure 5.3: Megaprimer generation by PCR in the presence of labeled nucleotides. Taq polymerase (“Taq”; NE Biolabs) and KOD Hot Start polymerase (“KOD”; Novagen, Darmstadt, Germany) were used for PCR amplification. Lane L: DNA ladder (1 kb PLUS, NE Biolabs) annotated on the left. DBCO-dU, DBCO-(PEG)₄-dUTP; Bio-dU, Biotin-16-dUTP; Taq, Taq polymerase; KOD, KOD Hot Start polymerase. The numbers indicate the percentages of labeled nucleotides in the PCR reactions.

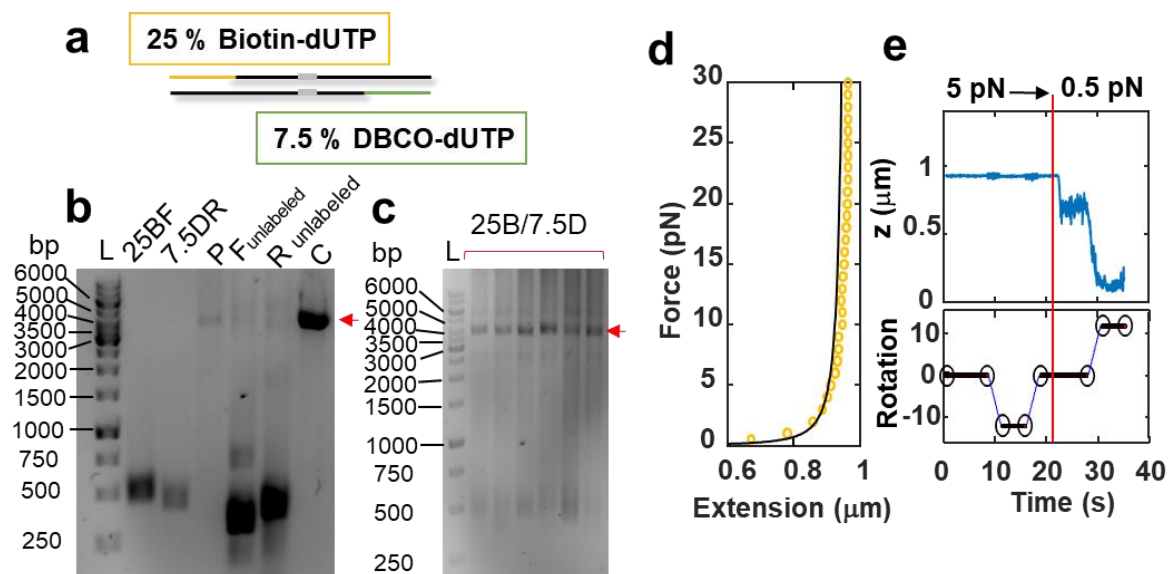


Supplementary Figure 5.4: DNA amplification with megaprimers to produce labeled DNA constructs for single-molecule measurements. (a) Gel analysis of the products of PCR reactions using KOD polymerase to assemble labeled DNA constructs with a linear template with 3 repeats of the Widom 601 sequence and megaprimers generated by Taq polymerase in the previous step. The arrows indicate the expected size of the amplification product. PCR conditions are given in the legend. (b) Products of PCR amplification using KOD polymerase and different ratios of biotin and DBCO labeled megaprimers generated using either Taq and KOD polymerase (rightmost lane). 50KOD; 50% biotin-dU or DBCO-dU labeled prepared using KOD polymerase in the previous step. (c) 5 repeats of PCR experiments using KOD polymerase and Lane 1, 28% Biotin-dU/28% DBCO-dU; 2, 28% Biotin-dU/44% DBCO-dU; 3, 44% Biotin-dU/16% DBCO-dU; 4, 44% Biotin-dU/28% DBCO-dU; 5, 44% Biotin-dU/44% DBCO-dU megaprimers generated using Taq polymerase in the previous step. (d) 5 repeats of PCR experiments using KOD polymerase generated forward and reverse megaprimers. Panels c and d demonstrate the good reproducibility of the megaprimer PCR reactions. (e) Quantification of the target band intensity (labeled as P) and free megaprimer (labeled as F) to the integrated total intensity of all bands in the lane of the gels in panels c and d. Numbers refer to the same conditions as in panel c. Values and error bars are the mean and standard deviation from the 5 repeats. I achieve >50% target band intensity for all tested conditions. Image quantification was carried out in Image Lab (BIO-RAD). I selected the relevant lanes and detected band intensities of each lane. Background intensities were subtracted by specifying the size of a rolling disk (disk size) that determines how closely the background level follows the intensity profile.

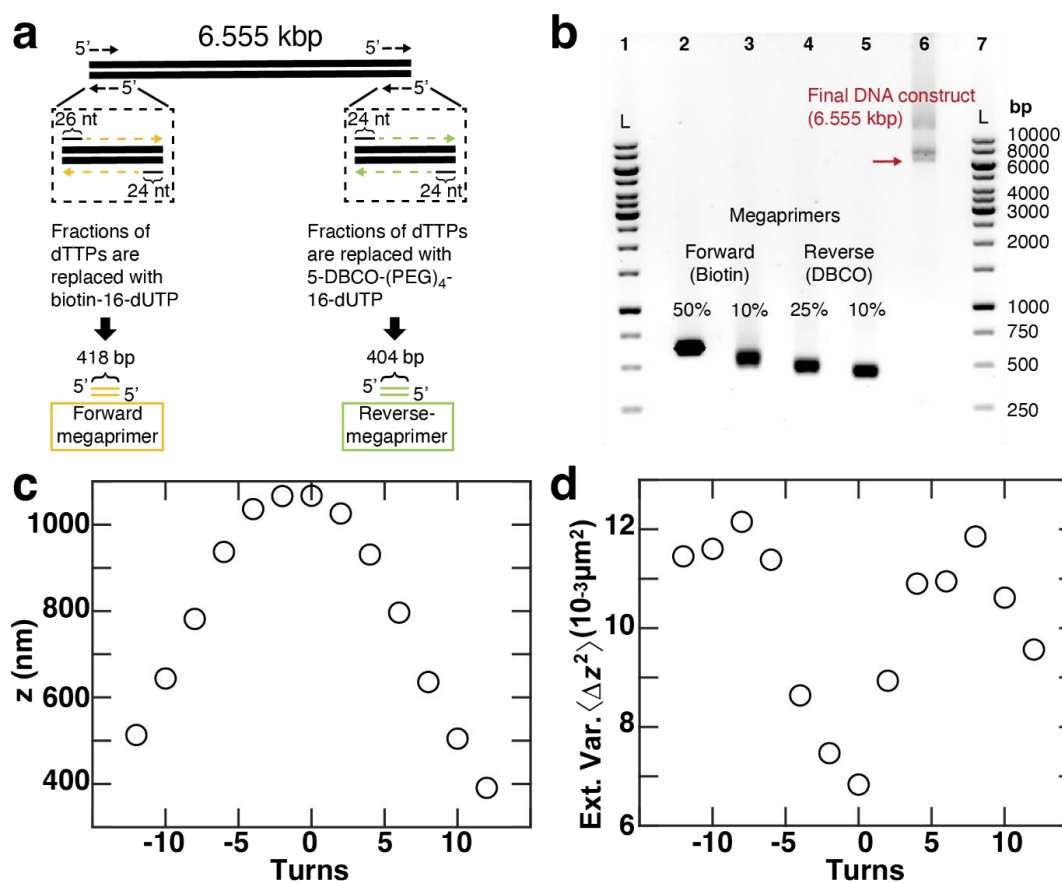


Supplementary Figure 5.5: Analysis of megaprimers PCR products obtained in high concentration PCR reactions. Gel analysis of the products of a modified PCR protocol that uses a smaller final reaction volume and correspondingly higher concentrations of megaprimers and template DNA compared to the protocols described in the main text, to facilitate downstream processing and to test whether this results in a higher yield. Megaprimer conditions are indicated in the panels. “Band intensity” is the intensity of the product band relative to the intensity in the entire lane.

I performed the high concentration/low volume PCR reactions by using 200 ng forward, 200 ng reverse megaprimer, 50 ng linear template, and 10% DMSO in 20 μ L 1 x KOD Hot start polymerase Master mix (compared to 100 μ l final volume for the reactions described in the main text). I used the following PCR cycling parameters: Initial denaturation at 95 $^{\circ}$ C for 2 min; 35 cycles of denaturation at 95 $^{\circ}$ C for 20 s, annealing at 60 $^{\circ}$ C for 10 s, and elongation at 70 $^{\circ}$ C for 65 s. The final cycle was followed by extension at 72 $^{\circ}$ C for 1 min. I carried out 3 repeats of each PCR reaction with a given set of megaprimer conditions and quantified the relative band intensity of the main product band compared to the integral of all band intensities in one lane. The results suggest that the high concentration/low volume reactions achieve a good yield of the correctly labeled product (visible as the main bands in the gels), but also tend to produce a significant number of longer products (visible as a smear above the main band). Previous work has suggested that megaprimer concentrations higher than 0.01 μ M inhibit the PCR reaction[214]. In contrast, others have argued that megaprimer concentration between 0.02 and 0.04 μ M could be advantageous compared to 0.01 μ M [215, 216]. I use 0.008 μ M megaprimers in the protocol described in the main text and 0.04 μ M megaprimer for high concentration / low volume reactions. The results suggest that both protocols are suitable for amplifying the final products, but that the lower concentration/larger volume reactions typically have better purity compared to high concentration/small volume reactions, which might be due to the increased tendency for megaprimer mispriming and nonspecific amplification at high concentration [215, 216]. One advantage of the higher concentration/lower volume reaction is that the subsequent PCR clean up step requires less material and fewer centrifugation steps due to the lower volume.

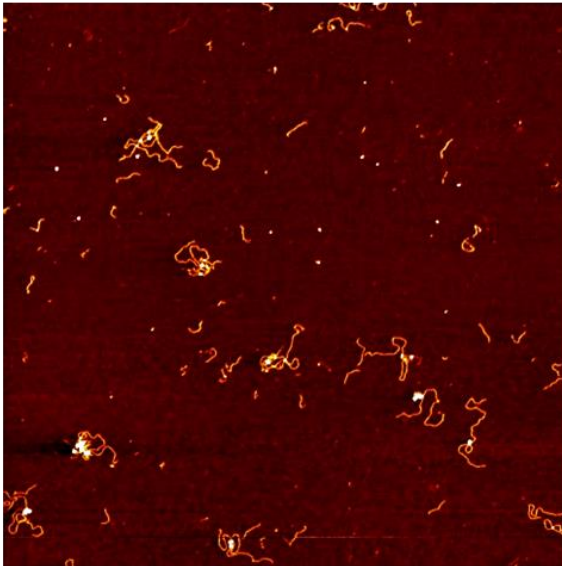


Supplementary Figure 5.6: DNA construct with 1x Widom 601 generated with megaprimer PCR reactions. (a) Schematic of the reaction. The overall approach is the same as in the main text (Figure 2.1a), but the DNA construct has only one Widom 601 sequence. ~300 bp of both forwards and reverse megaprimer are labeled with, in this case, 25% Biotin-16-dUTP and 7.5% DBCO-(PEG)₄-dUTP. I performed PCR reactions with 200 ng forward megaprimers, 200 ng reverse megaprimers, and 50 ng linear template in 20 mL 1x Phusion Hot Start polymerase master mix. I used the following PCR cycling parameters: initial denaturation at 98 °C for 2 min; 35 cycles of denaturation at 98 °C for 30 s, annealing at 67 °C for 30 s, and elongation at 72 °C for 90 s. The final cycle was followed by extension at 72°C for 10 min. PCR products were purified by using the QIAquick PCR Purification Kit (Qiagen, Hilden, Germany) after each step of PCR amplification. (b) Gel analysis of the resulting megaprimers and final products. 25BF, 25% Biotin-16-dUTP labeled forward megaprimer; 7.5DR, DBCO-(PEG)₄-dUTP labeled reverse megaprimer; P, the final 1 x Widom 601 DNA products made from labeled megaprimer; F_{unlabeled}, forward megaprimer without labels; R_{unlabeled}, reverse megaprimer without labels; C, the positive control of 1 x Widom 601 DNA without labeled nucleotides. (c) Gel analysis of six repeats of the megaprimer PCR described above. The reaction achieves good yield and reproducibility. (d) Force extension curve of the 1x Widom 601 DNA construct in magnetic tweezers. The black line is a co-plot of the inextensible WLC model. (e) Coilability test of the 1x Widom 601 DNA construct in magnetic tweezers. The DNA is twisted first at a force of 5 pN to -12 turns; the fact that the extension does not change upon underwinding indicates correct tethering by a single double-stranded DNA. The DNA is then twisted at 0.5 pN to +12 turns; the fact that the extension decreases upon overwinding indicates that the DNA tether is torsionally constrained.

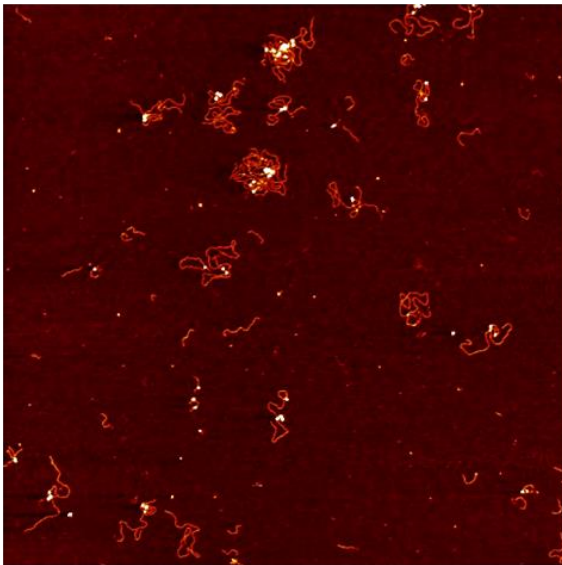


Supplementary Figure 5.7: Megaprimers PCR-based DNA assembly of a 6.6 kbp DNA construct and force spectroscopy experiments in magnetic tweezers. (a) Schematic of the ligation-free megaprimers PCR-based DNA assembly method to synthesize a torsionally constrained 6.6 kbp DNA construct. The overall procedure is the same as what is described in the main text and Figure 2.1a, however, this reaction uses a DNA without nucleosome positioning sequences and different primer sequences. Two sets of 24-bp (or 26-bp) ssDNA primers and linearized templates are used in PCR reactions to produce two multiply-labeled 404 bp (or 418 bp) DNAs that become the megaprimers. The two megaprimers are labeled with biotin and DBCO, respectively. A M13mp18-template (NEB; linearized by BspH1 enzyme (NEB)) is used for subsequent PCR to get the final 6555 bp construct. No DMSO was added. (b) Visualization of the PCR result by gel electrophoresis. The left- and right-most lanes (labeled 1 and 7) contain a DNA size ladder (“L”, 1 kb PLUS ladder, NEB). The megaprimers (lanes 2,3,4,5) were generated in PCR reactions using different amounts of biotin-dUTPs and DBCO-dUTPs, respectively, and appear at higher bp-values than their actual base pair numbers which is due to the biotin and DBCO labelling, which gives them a higher molecular weight. The final DNA construct (lane 6) is indicated by a red arrow. (c) Extension-rotation curve at a constant force of 0.25 pN indicates that the DNA construct is torsionally constrained. Extension data were recorded at 1000 Hz to enable analysis of the variance, in addition to the mean extension [145] (d) Variance of the extension fluctuations of the same bead shown in panel c. The 6.6 kbp DNA construct exhibits the typical response of double-stranded DNA, with decreasing extension and increasing extension fluctuations upon over- and underwinding [145].

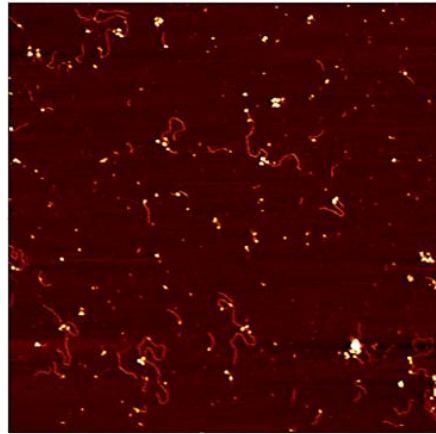
a Unmodified



b H3K36me3

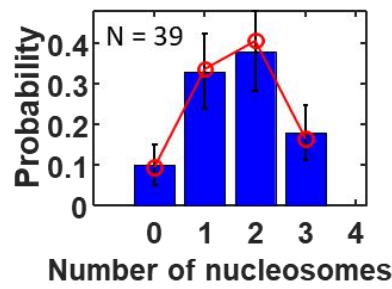


c H4K5/8/12/16ac

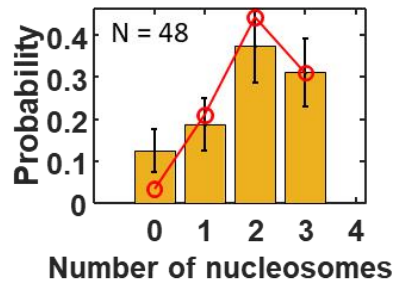


500 nm

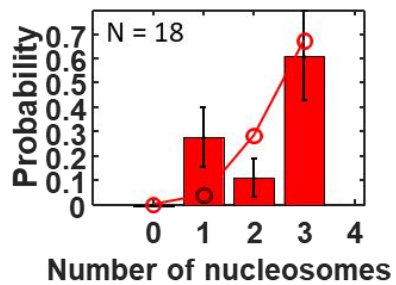
d Unmodified



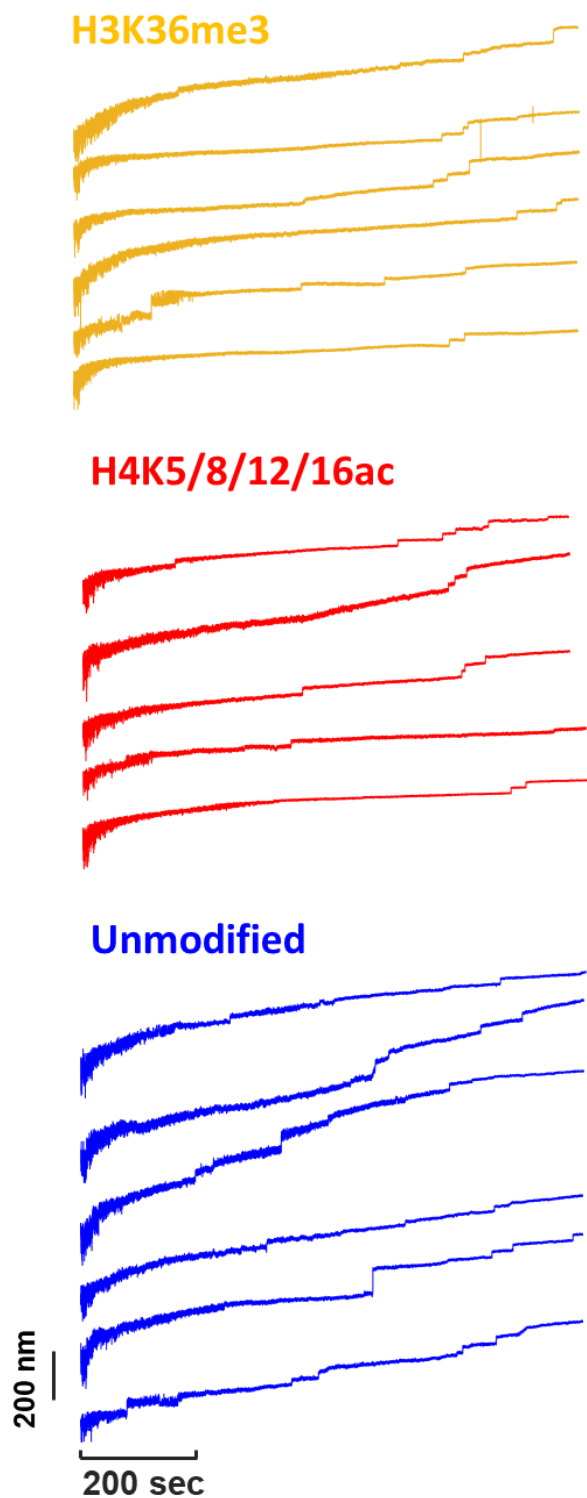
e H3K36me3



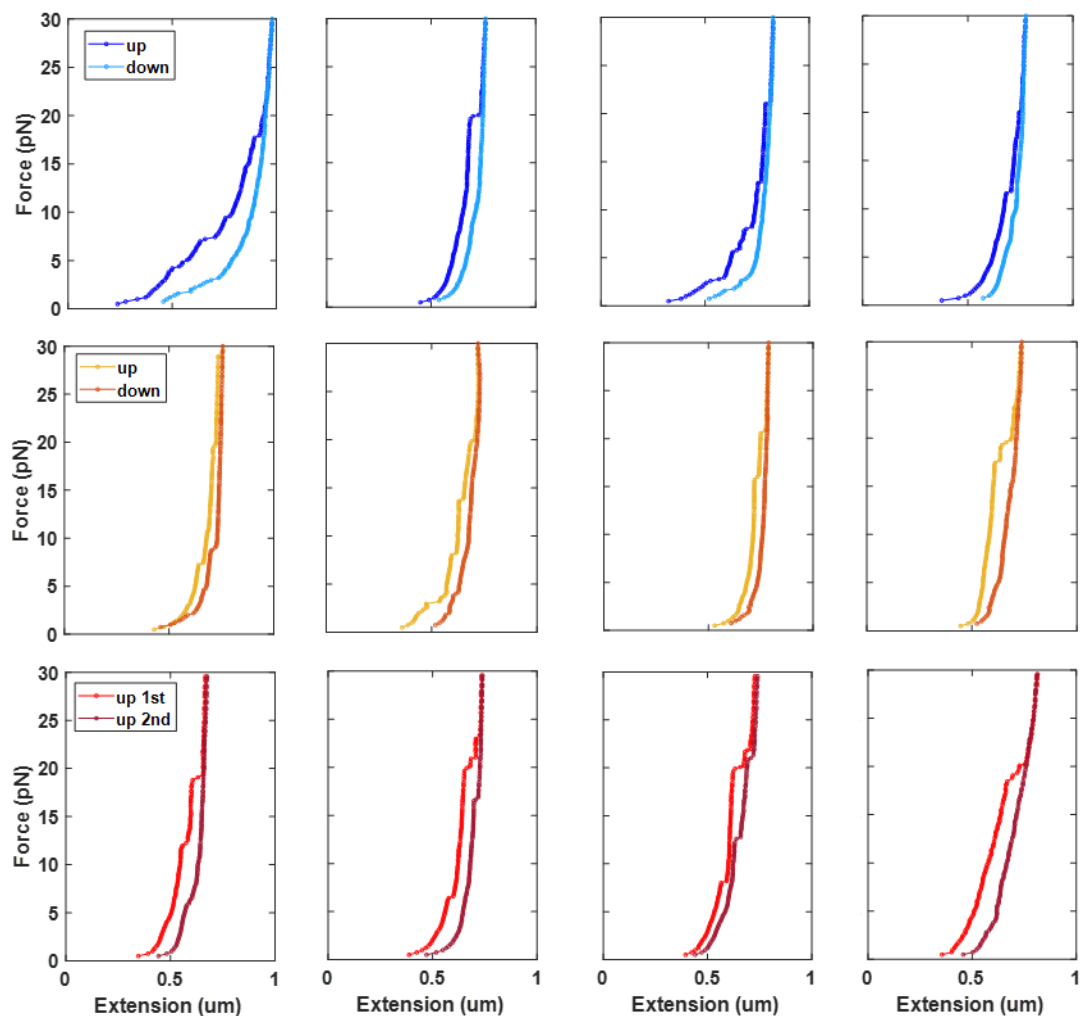
f H4K5/8/12/16ac



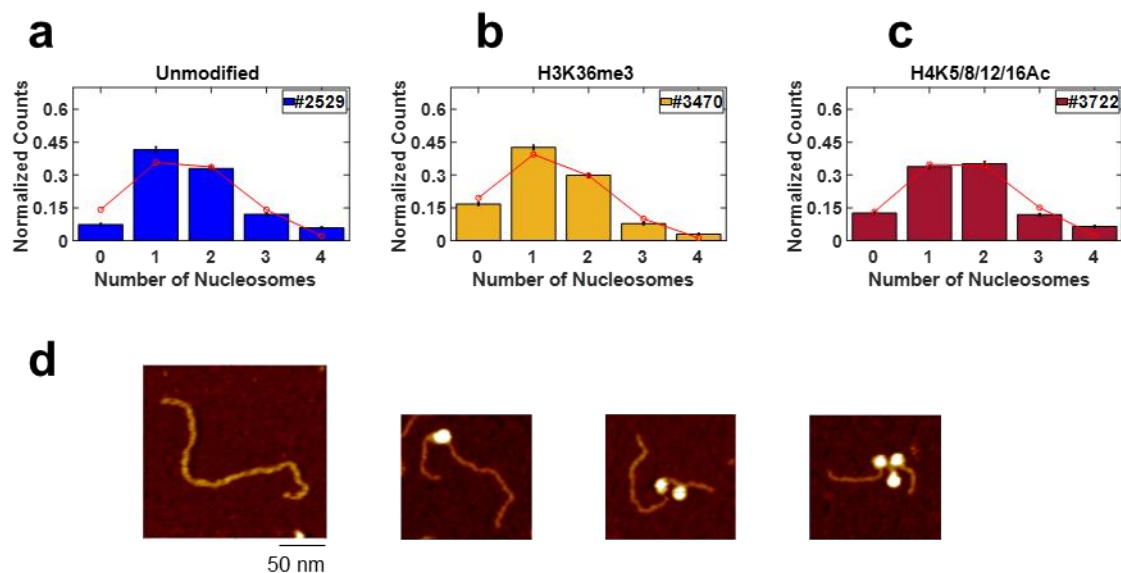
Supplementary Figure 5.8: AFM image shows the heterogeneity of nucleosome population. (a-c) AFM images of unmodified, H3K36me3, and H4K5/8/12/16ac nucleosomes reconstituted on 2823 bp DNA for the MT experiments. (d-f) Histogram of the number of variant nucleosomes assembled on the DNA constructs obtained from AFM images (N, DNA molecules; error bars are from counting statistics). Red points are the best fit of a binomial distribution with fitted assembly probability $P = 0.55$, 0.68 , and 0.88 for unmodified, H3K36me3, and H4K5/8/12/16ac nucleosome reconstitution.



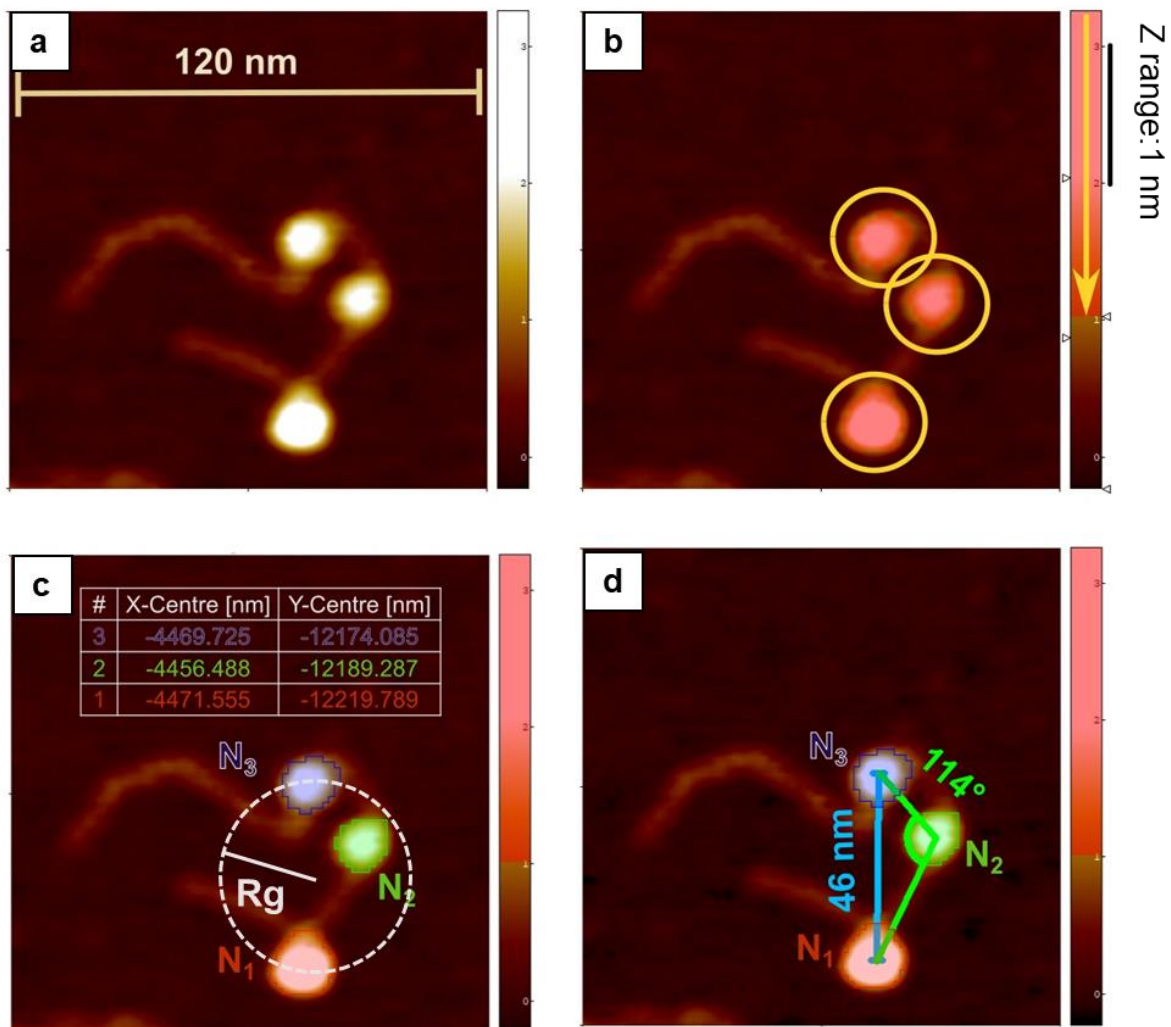
Supplementary Figure 5.9: Extension time traces in magnetic tweezers. Examples of extension time traces under applied force from 0.5 to 30 pN for different variant nucleosomes (Unmodified, blue lines; H3K36me3, orange lines; H4K5/8/12/16ac, red lines).



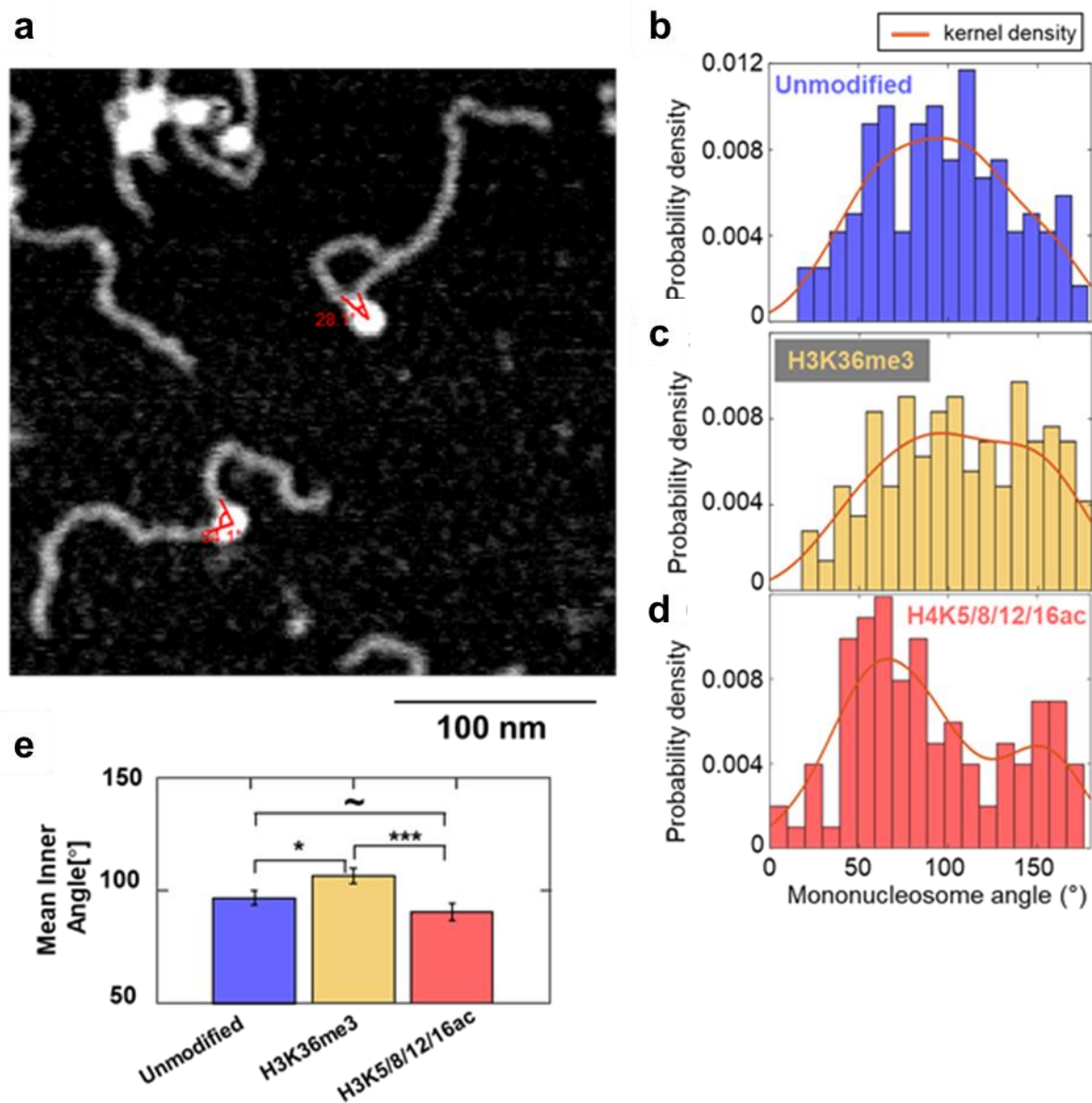
Supplementary Figure 5.10: Repeated force-extension cycles for different nucleosome variants. Examples of force-extension curves for unmodified (top row), H3K36me3 (middle row), and H4K5/8/12/16ac (bottom row) nucleosome constructs. Curves show the first stretch cycle from low to high forces (0.5 – 30 pN; “up”) and either the first release cycle (i.e. returning from high force down to low force; “down”) or, for the H4K5/8/12/16ac condition, the second stretch cycle (“up 2nd”).



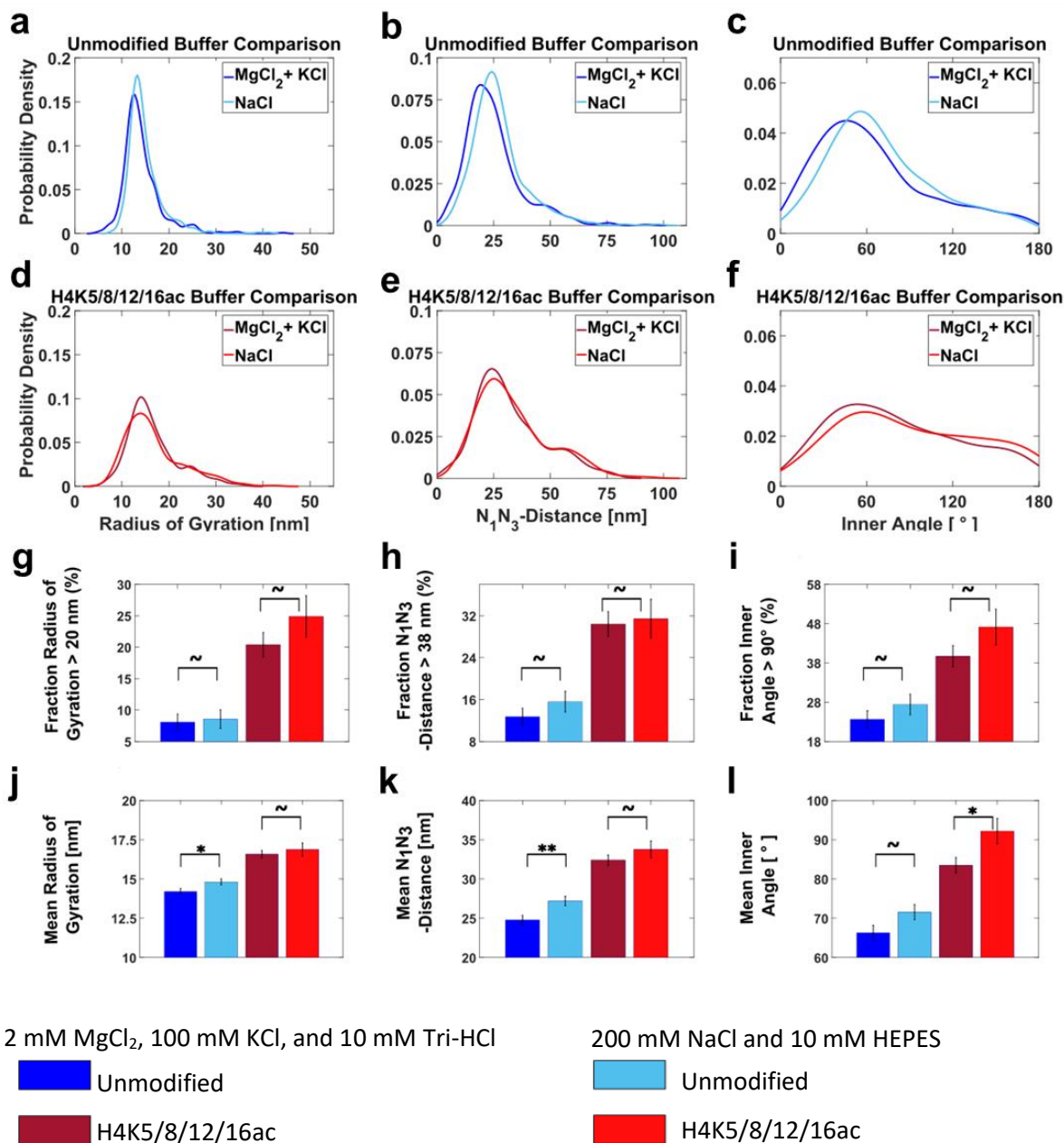
Supplementary Figure 5.11: Quantification of nucleosome assembly on DNA from AFM images. (a-c) Histogram of the number of nucleosomes assembled on DNA strands for (a) unmodified ($N = 2529$), (b) H3K36me3 ($N=3470$), and (c) H4K5/8/12/16Ac ($N = 3722$) obtained from AFM images. The numbers in the legend indicate the number of DNA strands analyzed for each type of nucleosome. Red points are the best fit of a binomial distribution with fitted assembly probability for unmodified ($P = 0.418 \pm 0.010$), H3K36me3 ($P = 0.344 \pm 0.008$), H4K5/8/12/16ac ($P = 0.415 \pm 0.008$). Error bars here indicates the counting error, errors of the fitted P values are the standard error of a binomial distribution. (d) Examples of AFM images of bare DNA, and unmodified type mono-, di-, tri-, and tetra- nucleosomes. The scale bar applies to all AFM images in panel d.



Supplementary Figure 5.12: Determination of geometric parameters from AFM images of tri-nucleosomes. Data analysis was performed in SPIP (Image Metrology). (a) AFM image of a selected tri-nucleosome sample. (b) A height threshold (Z range) is adjusted to detect the nucleosomes as areas of the topographic scan where this height limit is exceeded. (c) Using the particle detection feature the nucleosomes are then identified as three separate particles within the scan and their center positions are displayed in a table. The center positions are used to calculate the radius of gyration (R_g). (d) The nucleosomes are labeled N_1 , N_2 , and N_3 following the DNA strand from short to long arm. For analysis we determine the N_1N_3 -distance (blue) and the angle between the outer nucleosome centers and the center of the middle nucleosome (green).



Supplementary Figure 5.13: DNA exit angles for mononucleosomes. (a) Example AFM image of mononucleosomes selected from the AFM images of our tri-nucleosomes constructs. The traced DNA exit angles is indicated in the image. (b) Distribution of exit angles for unmodified nucleosomes (N = 133). (c) Distribution of exit angles for H3K36me3 nucleosomes (N = 160). (d) Distribution of exit angles for H4K5/8/12/16ac nucleosomes (N = 120). (e) Mean exit angles for the three different mononucleosome populations. Error bars indicate the standard error of the mean. The stars indicate significance based on two-tail two-sample *t*-tests: ~ not significant, **p* < 0.05, ***p* < 0.01, ****p* < 0.001.



Supplementary Figure 5.14: Influence of Mg²⁺ on tri-nucleosome conformations probed by AFM imaging. Probability distributions as kernel density estimates for radii of gyration, N₁N₃-distances, and inner angles for two different salt conditions for unmodified and H4K5/8/12/16ac nucleosomes obtained from AFM imaging. (a-c) Unmodified (d-f) H4K5/8/12/16ac. (a-f) show the kernel density estimates of the unmodified nucleosome with different types of salt co-plotted for each parameter. (g-l) show analysis of distributions from panels (a-f). ~ not significant, *p < 0.05, **p < 0.01, based on two-tail two-sample proportion-test (g-i) and two-tail two-sample *t*-tests (j-l).

6. Bibliography

- [1] E. Chargaff, "Chemical specificity of nucleic acids and mechanism of their enzymatic degradation," *Experientia*, vol. 6, no. 6, pp. 201-209, 1950/06/01 1950, doi: 10.1007/BF02173653.
- [2] J. D. Watson and F. H. C. Crick, "Molecular Structure of Nucleic Acids: A Structure for Deoxyribose Nucleic Acid," *Nature*, vol. 171, no. 4356, pp. 737-738, 1953/04/01 1953, doi: 10.1038/171737a0.
- [3] R. E. Franklin and R. G. Gosling, "Molecular structure of nucleic acids. Molecular configuration in sodium thymonucleate. 1953," *Ann N Y Acad Sci*, vol. 758, pp. 16-7, Jun 30 1995. [Online]. Available: <https://www.ncbi.nlm.nih.gov/pubmed/7625691>.
- [4] R. E. Franklin and R. G. Gosling, "The structure of sodium thymonucleate fibres. I. The influence of water content," *Acta Crystallographica*, vol. 6, no. 8, pp. 673-677, 1953, doi: 10.1107/s0365110x53001939.
- [5] S. Minchin and J. Lodge, "Understanding biochemistry: structure and function of nucleic acids," *Essays Biochem*, vol. 63, no. 4, pp. 433-456, Oct 16 2019, doi: 10.1042/EBC20180038.
- [6] D. A. Koster, A. Crut, S. Shuman, M.-A. Bjornsti, and N. H. Dekker, "Cellular Strategies for Regulating DNA Supercoiling: A Single-Molecule Perspective," *Cell*, vol. 142, no. 4, pp. 519-530, 2010, doi: 10.1016/j.cell.2010.08.001.
- [7] S. M. Mirkin, "DNA Topology: Fundamentals," in *Encyclopedia of Life Sciences*, 2001.
- [8] T. Brouns *et al.*, "Free Energy Landscape and Dynamics of Supercoiled DNA by High-Speed Atomic Force Microscopy," *ACS Nano*, vol. 12, no. 12, pp. 11907-11916, Dec 26 2018, doi: 10.1021/acsnano.8b06994.
- [9] K. Luger, A. W. Mäder, R. K. Richmond, D. F. Sargent, and T. J. Richmond, "Crystal structure of the nucleosome core particle at 2.8 Å resolution," *Nature*, vol. 389, no. 6648, pp. 251-260, 1997, doi: 10.1038/38444.
- [10] G. Arents, R. W. Burlingame, B. C. Wang, W. E. Love, and E. N. Moudrianakis, "The nucleosomal core histone octamer at 3.1 Å resolution: a tripartite protein assembly and a left-handed superhelix," (in eng), *Proc Natl Acad Sci U S A*, vol. 88, no. 22, pp. 10148-52, Nov 15 1991, doi: 10.1073/pnas.88.22.10148.
- [11] G. Arents and E. N. Moudrianakis, "The histone fold: a ubiquitous architectural motif utilized in DNA compaction and protein dimerization," (in eng), *Proc Natl Acad Sci U S A*, vol. 92, no. 24, pp. 11170-4, Nov 21 1995, doi: 10.1073/pnas.92.24.11170.
- [12] R. K. McGinty and S. Tan, "Nucleosome structure and function," *Chem Rev*, vol. 115, no. 6, pp. 2255-73, Mar 25 2015, doi: 10.1021/cr500373h.
- [13] T. J. Richmond, J. T. Finch, B. Rushton, D. Rhodes, and A. Klug, "Structure of the nucleosome core particle at 7 Å resolution," *Nature*, vol. 311, no. 5986, pp. 532-537, 1984/10/01 1984, doi: 10.1038/311532a0.
- [14] J. T. Finch *et al.*, "X-ray diffraction study of a new crystal form of the nucleosome core showing higher resolution," *Journal of Molecular Biology*, vol. 145, no. 4, pp. 757-769, 1981, doi: [https://doi.org/10.1016/0022-2836\(81\)90313-2](https://doi.org/10.1016/0022-2836(81)90313-2).

- [15] K. Luger, T. J. Rechsteiner, and T. J. Richmond, "Preparation of nucleosome core particle from recombinant histones," *Methods Enzymol*, vol. 304, pp. 3-19, 1999, doi: 10.1016/s0076-6879(99)04003-3.
- [16] R. T. Simpson and D. W. Stafford, "Structural features of a phased nucleosome core particle," (in eng), *Proc Natl Acad Sci U S A*, vol. 80, no. 1, pp. 51-5, Jan 1983, doi: 10.1073/pnas.80.1.51.
- [17] P. T. Lowary and J. Widom, "New DNA sequence rules for high affinity binding to histone octamer and sequence-directed nucleosome positioning," *J Mol Biol*, vol. 276, no. 1, pp. 19-42, Feb 13 1998, doi: 10.1006/jmbi.1997.1494.
- [18] V. Dileep, Y. D. C. Eugene, and A. D. Curt, "Crystal Structures of Nucleosome Core Particles Containing the '601' Strong Positioning Sequence," *Journal of Molecular Biology*, vol. 403, no. 1, pp. 1-10, 2010, doi: <https://doi.org/10.1016/j.jmb.2010.08.039>.
- [19] E. Y. D. Chua, D. Vasudevan, G. E. Davey, B. Wu, and C. A. Davey, "The mechanics behind DNA sequence-dependent properties of the nucleosome," *Nucleic Acids Research*, vol. 40, no. 13, pp. 6338-6352, 2012, doi: 10.1093/nar/gks261 %J Nucleic Acids Research.
- [20] A. J. Andrews, X. Chen, A. Zevin, L. A. Stargell, and K. Luger, "The histone chaperone Nap1 promotes nucleosome assembly by eliminating nonnucleosomal histone DNA interactions," (in eng), *Molecular cell*, vol. 37, no. 6, pp. 834-42, Mar 26 2010, doi: 10.1016/j.molcel.2010.01.037.
- [21] A. J. Andrews and K. Luger, "Nucleosome Structure(s) and Stability: Variations on a Theme," vol. 40, no. 1, pp. 99-117, 2011, doi: 10.1146/annurev-biophys-042910-155329.
- [22] Y. Chen *et al.*, "Asymmetric unwrapping of nucleosomal DNA propagates asymmetric opening and dissociation of the histone core," (in eng), *Proc Natl Acad Sci U S A*, vol. 114, no. 2, pp. 334-339, Jan 10 2017, doi: 10.1073/pnas.1611118114.
- [23] M. A. Hall, A. Shundrovsky, L. Bai, R. M. Fulbright, J. T. Lis, and M. D. Wang, "High-resolution dynamic mapping of histone-DNA interactions in a nucleosome," *Nat Struct Mol Biol*, vol. 16, no. 2, pp. 124-9, Feb 2009, doi: 10.1038/nsmb.1526.
- [24] S. F. Konrad *et al.*, "High-throughput AFM analysis reveals unwrapping pathways of H3 and CENP-A nucleosomes," *Nanoscale*, vol. 13, no. 10, pp. 5435-5447, Mar 18 2021, doi: 10.1039/d0nr08564b.
- [25] B. Fierz and M. G. Poirier, "Biophysics of Chromatin Dynamics," vol. 48, no. 1, pp. 321-345, 2019, doi: 10.1146/annurev-biophys-070317-032847.
- [26] G. D. Bowman and M. G. Poirier, "Post-translational modifications of histones that influence nucleosome dynamics," *Chem Rev*, vol. 115, no. 6, pp. 2274-95, Mar 25 2015, doi: 10.1021/cr500350x.
- [27] B. Dorigo, T. Schalch, K. Bystricky, and T. J. Richmond, "Chromatin fiber folding: requirement for the histone H4 N-terminal tail," *J Mol Biol*, vol. 327, no. 1, pp. 85-96, Mar 14 2003, doi: 10.1016/s0022-2836(03)00025-1.
- [28] M. Garcia-Ramirez, F. Dong, and J. Ausio, "Role of the histone "tails" in the folding of oligonucleosomes depleted of histone H1," *J Biol Chem*, vol. 267, no. 27, pp. 19587-95, Sep 25 1992. [Online]. Available: <https://www.ncbi.nlm.nih.gov/pubmed/1527076>.
- [29] K. Maeshima, S. Hihara, and M. Eltsov, "Chromatin structure: does the 30-nm fibre exist in vivo?," *Current Opinion in Cell Biology*, vol. 22, no. 3, pp. 291-297, 2010/06/01/ 2010, doi: <https://doi.org/10.1016/j.ceb.2010.03.001>.
- [30] O. Perisic, R. Collepardo-Guevara, and T. Schlick, "Modeling studies of chromatin fiber structure as a function of DNA linker length," *J Mol Biol*, vol. 403, no. 5, pp. 777-802, Nov 12 2010, doi: 10.1016/j.jmb.2010.07.057.
- [31] J. T. Finch and A. Klug, "Solenoidal model for superstructure in chromatin," *Proc Natl Acad Sci U S A*, vol. 73, no. 6, pp. 1897-901, Jun 1976, doi: 10.1073/pnas.73.6.1897.

- [32] J. D. McGhee, J. M. Nickol, G. Felsenfeld, and D. C. Rau, "Higher order structure of chromatin: orientation of nucleosomes within the 30 nm chromatin solenoid is independent of species and spacer length," *Cell*, vol. 33, no. 3, pp. 831-41, Jul 1983, doi: 10.1016/0092-8674(83)90025-9.
- [33] P. J. Butler, "A defined structure of the 30 nm chromatin fibre which accommodates different nucleosomal repeat lengths," *EMBO J*, vol. 3, no. 11, pp. 2599-604, Nov 1984, doi: 10.1002/j.1460-2075.1984.tb02180.x.
- [34] J. R. Daban and A. Bermudez, "Interdigitated solenoid model for compact chromatin fibers," *Biochemistry*, vol. 37, no. 13, pp. 4299-304, Mar 31 1998, doi: 10.1021/bi973117h.
- [35] T. Schalch, S. Duda, D. F. Sargent, and T. J. Richmond, "X-ray structure of a tetranucleosome and its implications for the chromatin fibre," *Nature*, vol. 436, no. 7047, pp. 138-41, Jul 7 2005, doi: 10.1038/nature03686.
- [36] R. A. Horowitz, A. J. Koster, J. Walz, and C. L. Woodcock, "Automated electron microscope tomography of frozen-hydrated chromatin: the irregular three-dimensional zigzag architecture persists in compact, isolated fibers," *J Struct Biol*, vol. 120, no. 3, pp. 353-62, Dec 1997, doi: 10.1006/jsbi.1997.3921.
- [37] B. A. Gibson *et al.*, "Organization of Chromatin by Intrinsic and Regulated Phase Separation," *Cell*, vol. 179, no. 2, pp. 470-484 e21, Oct 3 2019, doi: 10.1016/j.cell.2019.08.037.
- [38] A. Valouev, S. M. Johnson, S. D. Boyd, C. L. Smith, A. Z. Fire, and A. Sidow, "Determinants of nucleosome organization in primary human cells," *Nature*, vol. 474, no. 7352, pp. 516-20, May 22 2011, doi: 10.1038/nature10002.
- [39] S. J. Correll, M. H. Schubert, and S. A. Grigoryev, "Short nucleosome repeats impose rotational modulations on chromatin fibre folding," *EMBO J*, vol. 31, no. 10, pp. 2416-26, May 16 2012, doi: 10.1038/emboj.2012.80.
- [40] K. Maeshima, R. Imai, S. Tamura, and T. Nozaki, "Chromatin as dynamic 10-nm fibers," *Chromosoma*, vol. 123, no. 3, pp. 225-237, 2014/06/01 2014, doi: 10.1007/s00412-014-0460-2.
- [41] K. Maeshima, S. Ide, K. Hibino, and M. Sasai, "Liquid-like behavior of chromatin," *Curr Opin Genet Dev*, vol. 37, pp. 36-45, Apr 2016, doi: 10.1016/j.gde.2015.11.006.
- [42] P. J. Robinson, L. Fairall, V. A. Huynh, and D. Rhodes, "EM measurements define the dimensions of the '30-nm' chromatin fiber: evidence for a compact, interdigitated structure," *Proc Natl Acad Sci U S A*, vol. 103, no. 17, pp. 6506-11, Apr 25 2006, doi: 10.1073/pnas.0601212103.
- [43] P. J. Robinson and D. Rhodes, "Structure of the '30 nm' chromatin fibre: a key role for the linker histone," *Curr Opin Struct Biol*, vol. 16, no. 3, pp. 336-43, Jun 2006, doi: 10.1016/j.sbi.2006.05.007.
- [44] C. L. Woodcock, "Chromatin fibers observed in situ in frozen hydrated sections. Native fiber diameter is not correlated with nucleosome repeat length," *J Cell Biol*, vol. 125, no. 1, pp. 11-9, Apr 1994, doi: 10.1083/jcb.125.1.11.
- [45] C. Bouchet-Marquis, J. Dubochet, and S. Fakan, "Cryoelectron microscopy of vitrified sections: a new challenge for the analysis of functional nuclear architecture," *Histochem Cell Biol*, vol. 125, no. 1-2, pp. 43-51, Jan 2006, doi: 10.1007/s00418-005-0093-x.
- [46] E. Fussner *et al.*, "Open and closed domains in the mouse genome are configured as 10-nm chromatin fibres," *EMBO Rep*, vol. 13, no. 11, pp. 992-6, Nov 6 2012, doi: 10.1038/embor.2012.139.
- [47] M. A. Ricci, C. Manzo, M. F. Garcia-Parajo, M. Lakadamyali, and M. P. Cosma, "Chromatin fibers are formed by heterogeneous groups of nucleosomes in vivo," *Cell*, vol. 160, no. 6, pp. 1145-58, Mar 12 2015, doi: 10.1016/j.cell.2015.01.054.
- [48] D. E. Olins and A. L. Olins, "Chromatin history: our view from the bridge," *Nat Rev Mol Cell Biol*, vol. 4, no. 10, pp. 809-14, Oct 2003, doi: 10.1038/nrm1225.

- [49] A. L. Olins and D. E. Olins, "Spheroid chromatin units (v bodies)," *Science*, vol. 183, no. 4122, pp. 330-2, Jan 25 1974, doi: 10.1126/science.183.4122.330.
- [50] J. Sedat and L. Manuelidis, "A direct approach to the structure of eukaryotic chromosomes," *Cold Spring Harb Symp Quant Biol*, vol. 42 Pt 1, pp. 331-50, 1978, doi: 10.1101/sqb.1978.042.01.035.
- [51] J. Dubochet and N. Sartori Blanc, "The cell in absence of aggregation artifacts," *Micron*, vol. 32, no. 1, pp. 91-9, Jan 2001, doi: 10.1016/s0968-4328(00)00026-3.
- [52] S. Fakan and R. van Driel, "The perichromatin region: a functional compartment in the nucleus that determines large-scale chromatin folding," *Semin Cell Dev Biol*, vol. 18, no. 5, pp. 676-81, Oct 2007, doi: 10.1016/j.semcdb.2007.08.010.
- [53] S. Ide, S. Tamura, and K. Maeshima, "Chromatin behavior in living cells: Lessons from single-nucleosome imaging and tracking," *Bioessays*, vol. 44, no. 7, p. e2200043, Jul 2022, doi: 10.1002/bies.202200043.
- [54] J. J. Parmar, M. Woringer, and C. Zimmer, "How the Genome Folds: The Biophysics of Four-Dimensional Chromatin Organization," *Annu Rev Biophys*, vol. 48, pp. 231-253, May 6 2019, doi: 10.1146/annurev-biophys-052118-115638.
- [55] C. L. Woodcock, L. L. Frado, and J. B. Rattner, "The higher-order structure of chromatin: evidence for a helical ribbon arrangement," *J Cell Biol*, vol. 99, no. 1 Pt 1, pp. 42-52, Jul 1984, doi: 10.1083/jcb.99.1.42.
- [56] K. Maeshima *et al.*, "Nucleosomal arrays self-assemble into supramolecular globular structures lacking 30-nm fibers," *EMBO J*, vol. 35, no. 10, pp. 1115-32, May 17 2016, doi: 10.15252/embj.201592660.
- [57] K. Maeshima, S. Ide, and M. Babokhov, "Dynamic chromatin organization without the 30-nm fiber," *Curr Opin Cell Biol*, vol. 58, pp. 95-104, Jun 2019, doi: 10.1016/j.ceb.2019.02.003.
- [58] S. L. Berger, "Histone modifications in transcriptional regulation," *Curr Opin Genet Dev*, vol. 12, no. 2, pp. 142-8, Apr 2002, doi: 10.1016/s0959-437x(02)00279-4.
- [59] G. Millan-Zambrano, A. Burton, A. J. Bannister, and R. Schneider, "Histone post-translational modifications - cause and consequence of genome function," *Nat Rev Genet*, vol. 23, no. 9, pp. 563-580, Sep 2022, doi: 10.1038/s41576-022-00468-7.
- [60] G. Fudenberg, N. Abdennur, M. Imakaev, A. Goloborodko, and L. A. Mirny, "Emerging Evidence of Chromosome Folding by Loop Extrusion," *Cold Spring Harb Symp Quant Biol*, vol. 82, pp. 45-55, 2017, doi: 10.1101/sqb.2017.82.034710.
- [61] E. Lieberman-Aiden *et al.*, "Comprehensive mapping of long-range interactions reveals folding principles of the human genome," *Science*, vol. 326, no. 5950, pp. 289-93, Oct 9 2009, doi: 10.1126/science.1181369.
- [62] J. R. Dixon *et al.*, "Topological domains in mammalian genomes identified by analysis of chromatin interactions," *Nature*, vol. 485, no. 7398, pp. 376-80, Apr 11 2012, doi: 10.1038/nature11082.
- [63] I. Solovei *et al.*, "Nuclear architecture of rod photoreceptor cells adapts to vision in mammalian evolution," *Cell*, vol. 137, no. 2, pp. 356-68, Apr 17 2009, doi: 10.1016/j.cell.2009.01.052.
- [64] I. Solovei, K. Thanisch, and Y. Feodorova, "How to rule the nucleus: divide et impera," *Current Opinion in Cell Biology*, vol. 40, pp. 47-59, 2016/06/01/ 2016, doi: <https://doi.org/10.1016/j.ceb.2016.02.014>.
- [65] A. G. Matera, "Nuclear bodies: multifaceted subdomains of the interchromatin space," *Trends Cell Biol*, vol. 9, no. 8, pp. 302-9, Aug 1999, doi: 10.1016/s0962-8924(99)01606-2.

- [66] S. Kemeny *et al.*, "Spatial organization of chromosome territories in the interphase nucleus of trisomy 21 cells," *Chromosoma*, vol. 127, no. 2, pp. 247-259, Jun 2018, doi: 10.1007/s00412-017-0653-6.
- [67] T. Cremer and M. Cremer, "Chromosome territories," *Cold Spring Harb Perspect Biol*, vol. 2, no. 3, p. a003889, Mar 2010, doi: 10.1101/cshperspect.a003889.
- [68] A. Bolzer *et al.*, "Three-dimensional maps of all chromosomes in human male fibroblast nuclei and prometaphase rosettes," *PLoS Biol*, vol. 3, no. 5, p. e157, May 2005, doi: 10.1371/journal.pbio.0030157.
- [69] Q. Szabo, F. Bantignies, and G. Cavalli, "Principles of genome folding into topologically associating domains," (in eng), *Sci Adv*, vol. 5, no. 4, p. eaaw1668, Apr 2019, doi: 10.1126/sciadv.aaw1668.
- [70] T. Jenuwein and C. D. Allis, "Translating the histone code," *Science*, vol. 293, no. 5532, pp. 1074-80, Aug 10 2001, doi: 10.1126/science.1063127.
- [71] B. M. Turner, "Cellular memory and the histone code," *Cell*, vol. 111, no. 3, pp. 285-91, Nov 1 2002, doi: 10.1016/s0092-8674(02)01080-2.
- [72] P. B. Becker and J. L. Workman, "Nucleosome remodeling and epigenetics," *Cold Spring Harb Perspect Biol*, vol. 5, no. 9, Sep 1 2013, doi: 10.1101/cshperspect.a017905.
- [73] G. E. Zentner and S. Henikoff, "Regulation of nucleosome dynamics by histone modifications," *Nat Struct Mol Biol*, vol. 20, no. 3, pp. 259-66, Mar 2013, doi: 10.1038/nsmb.2470.
- [74] T. Kouzarides, "Chromatin modifications and their function," *Cell*, vol. 128, no. 4, pp. 693-705, Feb 23 2007, doi: 10.1016/j.cell.2007.02.005.
- [75] C. M. Rivera and B. Ren, "Mapping human epigenomes," *Cell*, vol. 155, no. 1, pp. 39-55, Sep 26 2013, doi: 10.1016/j.cell.2013.09.011.
- [76] T. Agalioti, G. Chen, and D. Thanos, "Deciphering the transcriptional histone acetylation code for a human gene," *Cell*, vol. 111, no. 3, pp. 381-92, Nov 1 2002, doi: 10.1016/s0092-8674(02)01077-2.
- [77] R. Blossey and H. Schiessel, "The Latest Twists in Chromatin Remodeling," *Biophys J*, vol. 114, no. 10, pp. 2255-2261, May 22 2018, doi: 10.1016/j.bpj.2017.12.008.
- [78] M. Shogren-Knaak, H. Ishii, J. M. Sun, M. J. Pazin, J. R. Davie, and C. L. Peterson, "Histone H4-K16 acetylation controls chromatin structure and protein interactions," *Science*, vol. 311, no. 5762, pp. 844-7, Feb 10 2006, doi: 10.1126/science.1124000.
- [79] M. S. Cosgrove, J. D. Boeke, and C. Wolberger, "Regulated nucleosome mobility and the histone code," *Nat Struct Mol Biol*, vol. 11, no. 11, pp. 1037-43, Nov 2004, doi: 10.1038/nsmb851.
- [80] H. Neumann *et al.*, "A method for genetically installing site-specific acetylation in recombinant histones defines the effects of H3 K56 acetylation," *Mol Cell*, vol. 36, no. 1, pp. 153-63, Oct 9 2009, doi: 10.1016/j.molcel.2009.07.027.
- [81] M. F. Dion, S. J. Altschuler, L. F. Wu, and O. J. Rando, "Genomic characterization reveals a simple histone H4 acetylation code," *Proc Natl Acad Sci U S A*, vol. 102, no. 15, pp. 5501-6, Apr 12 2005, doi: 10.1073/pnas.0500136102.
- [82] R. Oliva, D. P. Bazett-Jones, L. Locklear, and G. H. Dixon, "Histone hyperacetylation can induce unfolding of the nucleosome core particle," *Nucleic Acids Res*, vol. 18, no. 9, pp. 2739-47, May 11 1990, doi: 10.1093/nar/18.9.2739.
- [83] M. D. Shahbazian and M. Grunstein, "Functions of site-specific histone acetylation and deacetylation," *Annu Rev Biochem*, vol. 76, pp. 75-100, 2007, doi: 10.1146/annurev.biochem.76.052705.162114.

- [84] X. Wang and J. J. Hayes, "Acetylation mimics within individual core histone tail domains indicate distinct roles in regulating the stability of higher-order chromatin structure," *Mol Cell Biol*, vol. 28, no. 1, pp. 227-36, Jan 2008, doi: 10.1128/MCB.01245-07.
- [85] M. T. Bedford and S. G. Clarke, "Protein arginine methylation in mammals: who, what, and why," *Mol Cell*, vol. 33, no. 1, pp. 1-13, Jan 16 2009, doi: 10.1016/j.molcel.2008.12.013.
- [86] J. C. Black, C. Van Rechem, and J. R. Whetstine, "Histone lysine methylation dynamics: establishment, regulation, and biological impact," *Mol Cell*, vol. 48, no. 4, pp. 491-507, Nov 30 2012, doi: 10.1016/j.molcel.2012.11.006.
- [87] M. Lachner, D. O'Carroll, S. Rea, K. Mechtler, and T. Jenuwein, "Methylation of histone H3 lysine 9 creates a binding site for HP1 proteins," *Nature*, vol. 410, no. 6824, pp. 116-20, Mar 1 2001, doi: 10.1038/35065132.
- [88] A. J. Bannister *et al.*, "Selective recognition of methylated lysine 9 on histone H3 by the HP1 chromo domain," *Nature*, vol. 410, no. 6824, pp. 120-4, Mar 1 2001, doi: 10.1038/35065138.
- [89] K. Plath *et al.*, "Role of histone H3 lysine 27 methylation in X inactivation," *Science*, vol. 300, no. 5616, pp. 131-5, Apr 4 2003, doi: 10.1126/science.1084274.
- [90] A. A. Alekseyenko, A. A. Gorchakov, P. V. Kharchenko, and M. I. Kuroda, "Reciprocal interactions of human C10orf12 and C17orf96 with PRC2 revealed by BioTAP-XL cross-linking and affinity purification," *Proc Natl Acad Sci U S A*, vol. 111, no. 7, pp. 2488-93, Feb 18 2014, doi: 10.1073/pnas.1400648111.
- [91] R. Margueron and D. Reinberg, "The Polycomb complex PRC2 and its mark in life," *Nature*, vol. 469, no. 7330, pp. 343-9, Jan 20 2011, doi: 10.1038/nature09784.
- [92] W. Yuan *et al.*, "Dense chromatin activates Polycomb repressive complex 2 to regulate H3 lysine 27 methylation," *Science*, vol. 337, no. 6097, pp. 971-5, Aug 24 2012, doi: 10.1126/science.1225237.
- [93] A. J. Bannister, R. Schneider, F. A. Myers, A. W. Thorne, C. Crane-Robinson, and T. Kouzarides, "Spatial distribution of di- and tri-methyl lysine 36 of histone H3 at active genes," *J Biol Chem*, vol. 280, no. 18, pp. 17732-6, May 6 2005, doi: 10.1074/jbc.M500796200.
- [94] C. R. Vakoc, M. M. Sachdeva, H. Wang, and G. A. Blobel, "Profile of histone lysine methylation across transcribed mammalian chromatin," *Mol Cell Biol*, vol. 26, no. 24, pp. 9185-95, Dec 2006, doi: 10.1128/MCB.01529-06.
- [95] O. Ordu, A. Lusser, and N. H. Dekker, "Recent insights from in vitro single-molecule studies into nucleosome structure and dynamics," *Biophys Rev*, vol. 8, no. Suppl 1, pp. 33-49, 2016, doi: 10.1007/s12551-016-0212-z.
- [96] H. Miller, Z. Zhou, J. Shepherd, A. J. M. Wollman, and M. C. Leake, "Single-molecule techniques in biophysics: a review of the progress in methods and applications," *Rep Prog Phys*, vol. 81, no. 2, p. 024601, Feb 2018, doi: 10.1088/1361-6633/aa8a02.
- [97] S. Mihardja, A. J. Spakowitz, Y. Zhang, and C. Bustamante, "Effect of force on mononucleosomal dynamics," *Proc Natl Acad Sci U S A*, vol. 103, no. 43, pp. 15871-6, Oct 24 2006, doi: 10.1073/pnas.0607526103.
- [98] Y. Cui and C. Bustamante, "Pulling a single chromatin fiber reveals the forces that maintain its higher-order structure," *Proc Natl Acad Sci U S A*, vol. 97, no. 1, pp. 127-32, Jan 4 2000, doi: 10.1073/pnas.97.1.127.
- [99] M. Kruihof, F. T. Chien, A. Routh, C. Logie, D. Rhodes, and J. van Noort, "Single-molecule force spectroscopy reveals a highly compliant helical folding for the 30-nm chromatin fiber," *Nat Struct Mol Biol*, vol. 16, no. 5, pp. 534-40, May 2009, doi: 10.1038/nsmb.1590.
- [100] M. Kruihof and J. van Noort, "Hidden Markov analysis of nucleosome unwrapping under force," *Biophys J*, vol. 96, no. 9, pp. 3708-15, May 6 2009, doi: 10.1016/j.bpj.2009.01.048.

- [101] H. Meng, K. Andresen, and J. van Noort, "Quantitative analysis of single-molecule force spectroscopy on folded chromatin fibers," *Nucleic Acids Res*, vol. 43, no. 7, pp. 3578-90, Apr 20 2015, doi: 10.1093/nar/gkv215.
- [102] A. Soman *et al.*, "Columnar structure of human telomeric chromatin," *Nature*, vol. 609, no. 7929, pp. 1048-1055, Sep 2022, doi: 10.1038/s41586-022-05236-5.
- [103] A. Kaczmarczyk, H. Meng, O. Ordu, J. V. Noort, and N. H. Dekker, "Chromatin fibers stabilize nucleosomes under torsional stress," *Nat Commun*, vol. 11, no. 1, p. 126, Jan 8 2020, doi: 10.1038/s41467-019-13891-y.
- [104] A. Kaczmarczyk, A. Allahverdi, T. B. Brouwer, L. Nordenskiöld, N. H. Dekker, and J. van Noort, "Single-molecule force spectroscopy on histone H4 tail-cross-linked chromatin reveals fiber folding," *J Biol Chem*, vol. 292, no. 42, pp. 17506-17513, Oct 20 2017, doi: 10.1074/jbc.M117.791830.
- [105] T. R. Strick, J. F. Allemand, D. Bensimon, A. Bensimon, and V. Croquette, "The elasticity of a single supercoiled DNA molecule," *Science*, vol. 271, no. 5257, pp. 1835-7, Mar 29 1996, doi: 10.1126/science.271.5257.1835.
- [106] T. Strick, J. Allemand, V. Croquette, and D. Bensimon, "Twisting and stretching single DNA molecules," *Prog Biophys Mol Biol*, vol. 74, no. 1-2, pp. 115-40, 2000, doi: 10.1016/s0079-6107(00)00018-3.
- [107] C. Gosse and V. Croquette, "Magnetic tweezers: micromanipulation and force measurement at the molecular level," *Biophys J*, vol. 82, no. 6, pp. 3314-29, Jun 2002, doi: 10.1016/S0006-3495(02)75672-5.
- [108] A. J. te Velthuis, J. W. Kerssemakers, J. Lipfert, and N. H. Dekker, "Quantitative guidelines for force calibration through spectral analysis of magnetic tweezers data," (in eng), *Biophys J*, vol. 99, no. 4, pp. 1292-302, Aug 9 2010, doi: 10.1016/j.bpj.2010.06.008.
- [109] B. M. Lansdorp and O. A. Saleh, "Power spectrum and Allan variance methods for calibrating single-molecule video-tracking instruments," *Rev Sci Instrum*, vol. 83, no. 2, p. 025115, Feb 2012, doi: 10.1063/1.3687431.
- [110] O. Kratky and G. Porod, "Diffuse small-angle scattering of X-rays in colloid systems," *J Colloid Sci*, vol. 4, no. 1, pp. 35-70, Feb 1949, doi: 10.1016/0095-8522(49)90032-x.
- [111] S. B. Smith, Y. Cui, and C. Bustamante, "Overstretching B-DNA: the elastic response of individual double-stranded and single-stranded DNA molecules," *Science*, vol. 271, no. 5250, pp. 795-9, Feb 9 1996, doi: 10.1126/science.271.5250.795.
- [112] S. B. Smith, L. Finzi, and C. Bustamante, "Direct mechanical measurements of the elasticity of single DNA molecules by using magnetic beads," *Science*, vol. 258, no. 5085, pp. 1122-6, Nov 13 1992, doi: 10.1126/science.1439819.
- [113] C. Bustamante, J. F. Marko, E. D. Siggia, and S. Smith, "Entropic elasticity of lambda-phage DNA," *Science*, vol. 265, no. 5178, pp. 1599-600, Sep 9 1994, doi: 10.1126/science.8079175.
- [114] C. Bouchiat, M. D. Wang, J. Allemand, T. Strick, S. M. Block, and V. Croquette, "Estimating the persistence length of a worm-like chain molecule from force-extension measurements," *Biophys J*, vol. 76, no. 1 Pt 1, pp. 409-13, Jan 1999, doi: 10.1016/s0006-3495(99)77207-3.
- [115] I. D. Vilfan, J. Lipfert, D. A. Koster, S. G. Lemay, and N. H. Dekker, "Magnetic Tweezers for Single-Molecule Experiments," in *Handbook of Single-Molecule Biophysics*, P. Hinterdorfer and A. Oijen Eds. New York, NY: Springer US, 2009, pp. 371-395.
- [116] J. Lipfert, D. A. Koster, I. D. Vilfan, S. Hage, and N. H. Dekker, "Single-molecule magnetic tweezers studies of type IB topoisomerases," *Methods Mol Biol*, vol. 582, pp. 71-89, 2009, doi: 10.1007/978-1-60761-340-4_7.

- [117] D. J. Clarke and A. Lane, "Introduction: emerging themes in DNA topoisomerase research," *Methods Mol Biol*, vol. 582, pp. 1-9, 2009, doi: 10.1007/978-1-60761-340-4_1.
- [118] F. S. Papini, M. Seifert, and D. Dulin, "High-yield fabrication of DNA and RNA constructs for single molecule force and torque spectroscopy experiments," *Nucleic Acids Res*, vol. 47, no. 22, p. e144, Dec 16 2019, doi: 10.1093/nar/gkz851.
- [119] D. H. Paik, V. A. Roskens, and T. T. Perkins, "Torsionally constrained DNA for single-molecule assays: an efficient, ligation-free method," *Nucleic Acids Res*, vol. 41, no. 19, p. e179, Oct 2013, doi: 10.1093/nar/gkt699.
- [120] S. Gruber, A. Lof, S. M. Sedlak, M. Benoit, H. E. Gaub, and J. Lipfert, "Designed anchoring geometries determine lifetimes of biotin-streptavidin bonds under constant load and enable ultra-stable coupling," *Nanoscale*, vol. 12, no. 41, pp. 21131-21137, Nov 7 2020, doi: 10.1039/d0nr03665j.
- [121] S. M. Sedlak, L. C. Schendel, H. E. Gaub, and R. C. Bernardi, "Streptavidin/biotin: Tethering geometry defines unbinding mechanics," *Sci Adv*, vol. 6, no. 13, p. eaay5999, Mar 2020, doi: 10.1126/sciadv.aay5999.
- [122] A. Lof *et al.*, "Multiplexed protein force spectroscopy reveals equilibrium protein folding dynamics and the low-force response of von Willebrand factor," *Proc Natl Acad Sci U S A*, vol. 116, no. 38, pp. 18798-18807, Sep 17 2019, doi: 10.1073/pnas.1901794116.
- [123] G. Neuert, C. Albrecht, E. Pamir, and H. E. Gaub, "Dynamic force spectroscopy of the digoxigenin-antibody complex," *FEBS Lett*, vol. 580, no. 2, pp. 505-9, Jan 23 2006, doi: 10.1016/j.febslet.2005.12.052.
- [124] R. Janissen, B. A. Berghuis, D. Dulin, M. Wink, T. van Laar, and N. H. Dekker, "Invincible DNA tethers: covalent DNA anchoring for enhanced temporal and force stability in magnetic tweezers experiments," *Nucleic Acids Res*, vol. 42, no. 18, p. e137, Oct 2014, doi: 10.1093/nar/gku677.
- [125] M. Grandbois, M. Beyer, M. Rief, H. Clausen-Schaumann, and H. E. Gaub, "How strong is a covalent bond?," *Science*, vol. 283, no. 5408, pp. 1727-30, Mar 12 1999, doi: 10.1126/science.283.5408.1727.
- [126] C. K. Riener *et al.*, "Heterobifunctional crosslinkers for tethering single ligand molecules to scanning probes," *Analytica Chimica Acta*, vol. 497, no. 1, pp. 101-114, 2003/11/14/ 2003, doi: <https://doi.org/10.1016/j.aca.2003.08.041>.
- [127] J. L. Zimmermann, T. Nicolaus, G. Neuert, and K. Blank, "Thiol-based, site-specific and covalent immobilization of biomolecules for single-molecule experiments," *Nature Protocols*, vol. 5, no. 6, pp. 975-985, 2010/06/01 2010, doi: 10.1038/nprot.2010.49.
- [128] J. M. Eeftens, J. van der Torre, D. R. Burnham, and C. Dekker, "Copper-free click chemistry for attachment of biomolecules in magnetic tweezers," *BMC Biophys*, vol. 8, p. 9, 2015, doi: 10.1186/s13628-015-0023-9.
- [129] M. T. Woodside, W. M. Behnke-Parks, K. Larizadeh, K. Travers, D. Herschlag, and S. M. Block, "Nanomechanical measurements of the sequence-dependent folding landscapes of single nucleic acid hairpins," *Proc Natl Acad Sci U S A*, vol. 103, no. 16, pp. 6190-5, Apr 18 2006, doi: 10.1073/pnas.0511048103.
- [130] J. Zhou, V. Schweikhard, and S. M. Block, "Single-molecule studies of RNAPII elongation," *Biochim Biophys Acta*, vol. 1829, no. 1, pp. 29-38, Jan 2013, doi: 10.1016/j.bbagr.2012.08.006.
- [131] I. V. Dobrovolskaia and G. Arya, "Dynamics of forced nucleosome unraveling and role of nonuniform histone-DNA interactions," *Biophys J*, vol. 103, no. 5, pp. 989-98, Sep 5 2012, doi: 10.1016/j.bpj.2012.07.043.

- [132] F. Rico, L. Gonzalez, I. Casuso, M. Puig-Vidal, and S. Scheuring, "High-speed force spectroscopy unfolds titin at the velocity of molecular dynamics simulations," *Science*, vol. 342, no. 6159, pp. 741-3, Nov 8 2013, doi: 10.1126/science.1239764.
- [133] E. Herrero-Galan *et al.*, "Mechanical identities of RNA and DNA double helices unveiled at the single-molecule level," *J Am Chem Soc*, vol. 135, no. 1, pp. 122-31, Jan 9 2013, doi: 10.1021/ja3054755.
- [134] D. E. Smith, S. J. Tans, S. B. Smith, S. Grimes, D. L. Anderson, and C. Bustamante, "The bacteriophage straight phi29 portal motor can package DNA against a large internal force," *Nature*, vol. 413, no. 6857, pp. 748-52, Oct 18 2001, doi: 10.1038/35099581.
- [135] D. Dulin, T. J. Cui, J. Clossen, M. W. Docter, J. Lipfert, and N. H. Dekker, "High Spatiotemporal-Resolution Magnetic Tweezers: Calibration and Applications for DNA Dynamics," *Biophys J*, vol. 109, no. 10, pp. 2113-25, Nov 17 2015, doi: 10.1016/j.bpj.2015.10.018.
- [136] A. Huhle *et al.*, "Camera-based three-dimensional real-time particle tracking at kHz rates and Angstrom accuracy," *Nat Commun*, vol. 6, p. 5885, Jan 7 2015, doi: 10.1038/ncomms6885.
- [137] J. F. Marko and E. D. Siggia, "Fluctuations and supercoiling of DNA," *Science*, vol. 265, no. 5171, pp. 506-8, Jul 22 1994, doi: 10.1126/science.8036491.
- [138] Y. M. Lo, W. Z. Mehal, and K. A. Fleming, "Rapid production of vector-free biotinylated probes using the polymerase chain reaction," *Nucleic Acids Res*, vol. 16, no. 17, p. 8719, Sep 12 1988, doi: 10.1093/nar/16.17.8719.
- [139] J. Lipfert, X. Hao, and N. H. Dekker, "Quantitative modeling and optimization of magnetic tweezers," *Biophys J*, vol. 96, no. 12, pp. 5040-9, Jun 17 2009, doi: 10.1016/j.bpj.2009.03.055.
- [140] J. Lipfert *et al.*, "Double-stranded RNA under force and torque: similarities to and striking differences from double-stranded DNA," *Proc Natl Acad Sci U S A*, vol. 111, no. 43, pp. 15408-13, Oct 28 2014, doi: 10.1073/pnas.1407197111.
- [141] J. van Mameren *et al.*, "Unraveling the structure of DNA during overstretching by using multicolor, single-molecule fluorescence imaging," *Proc Natl Acad Sci U S A*, vol. 106, no. 43, pp. 18231-6, Oct 27 2009, doi: 10.1073/pnas.0904322106.
- [142] E. L. Florin, V. T. Moy, and H. E. Gaub, "Adhesion forces between individual ligand-receptor pairs," (in eng), *Science*, vol. 264, no. 5157, pp. 415-7, Apr 15 1994, doi: 10.1126/science.8153628.
- [143] F. Kriegel, N. Ermann, and J. Lipfert, "Probing the mechanical properties, conformational changes, and interactions of nucleic acids with magnetic tweezers," *J Struct Biol*, vol. 197, no. 1, pp. 26-36, Jan 2017, doi: 10.1016/j.jsb.2016.06.022.
- [144] T. R. Strick, V. Croquette, and D. Bensimon, "Homologous pairing in stretched supercoiled DNA," *Proc Natl Acad Sci U S A*, vol. 95, no. 18, pp. 10579-83, Sep 1 1998, doi: 10.1073/pnas.95.18.10579.
- [145] W. Vanderlinden, E. Skoruppa, P. Kolbeck, E. Carlon, and J. Lipfert, "DNA fluctuations reveal the size and dynamics of topological domains," *PNAS Nexus*, 2022, doi: 10.1093/pnasnexus/pgac268.
- [146] J. W. J. Kerssemakers, E. Laura Munteanu, L. Laan, T. L. Noetzel, M. E. Janson, and M. Dogterom, "Assembly dynamics of microtubules at molecular resolution," *Nature*, vol. 442, no. 7103, pp. 709-712, 2006/08/01 2006, doi: 10.1038/nature04928.
- [147] J. P. Anderson, B. Angerer, and L. A. Loeb, "Incorporation of reporter-labeled nucleotides by DNA polymerases," *Biotechniques*, vol. 38, no. 2, pp. 257-64, Feb 2005, doi: 10.2144/05382RR02.

- [148] H. Hoshino *et al.*, "Consecutive incorporation of functionalized nucleotides with amphiphilic side chains by novel KOD polymerase mutant," *Bioorg Med Chem Lett*, vol. 26, no. 2, pp. 530-533, Jan 15 2016, doi: 10.1016/j.bmcl.2015.11.079.
- [149] M. Kuwahara *et al.*, "Systematic characterization of 2'-deoxynucleoside- 5'-triphosphate analogs as substrates for DNA polymerases by polymerase chain reaction and kinetic studies on enzymatic production of modified DNA," *Nucleic Acids Res*, vol. 34, no. 19, pp. 5383-94, 2006, doi: 10.1093/nar/gkl637.
- [150] M. Kuwahara *et al.*, "Study on suitability of KOD DNA polymerase for enzymatic production of artificial nucleic acids using base/sugar modified nucleoside triphosphates," *Molecules*, vol. 15, no. 11, pp. 8229-40, Nov 12 2010, doi: 10.3390/molecules15118229.
- [151] N. Paul and J. J. B. Yee, "PCR incorporation of modified dNTPs: the substrate properties of biotinylated dNTPs," vol. 48, pp. 333-334, 2010.
- [152] T. Tasara *et al.*, "Incorporation of reporter molecule-labeled nucleotides by DNA polymerases. II. High-density labeling of natural DNA," *Nucleic Acids Research*, vol. 31, no. 10, pp. 2636-2646, 2003, doi: 10.1093/nar/gkg371.
- [153] Y. Y. Lin, T. Brouns, P. J. Kolbeck, W. Vanderlinden, and J. Lipfert, "High-yield ligation-free assembly of DNA constructs with nucleosome positioning sequence repeats for single-molecule manipulation assays," *J Biol Chem*, vol. 299, no. 7, p. 104874, Jul 2023, doi: 10.1016/j.jbc.2023.104874.
- [154] F. J. Solis, R. Bash, J. Yodh, S. M. Lindsay, and D. Lohr, "A statistical thermodynamic model applied to experimental AFM population and location data is able to quantify DNA-histone binding strength and internucleosomal interaction differences between acetylated and unacetylated nucleosomal arrays," *Biophys J*, vol. 87, no. 5, pp. 3372-87, Nov 2004, doi: 10.1529/biophysj.103.034744.
- [155] B. D. Brower-Toland, C. L. Smith, R. C. Yeh, J. T. Lis, C. L. Peterson, and M. D. Wang, "Mechanical disruption of individual nucleosomes reveals a reversible multistage release of DNA," *Proc Natl Acad Sci U S A*, vol. 99, no. 4, pp. 1960-5, Feb 19 2002, doi: 10.1073/pnas.022638399.
- [156] S. G. Mochrie, A. H. Mack, D. J. Schlingman, R. Collins, M. Kamenetska, and L. Regan, "Unwinding and rewinding the nucleosome inner turn: force dependence of the kinetic rate constants," *Phys Rev E Stat Nonlin Soft Matter Phys*, vol. 87, no. 1, p. 012710, Jan 2013, doi: 10.1103/PhysRevE.87.012710.
- [157] A. H. Mack, D. J. Schlingman, R. P. Ilagan, L. Regan, and S. G. Mochrie, "Kinetics and thermodynamics of phenotype: unwinding and rewinding the nucleosome," *J Mol Biol*, vol. 423, no. 5, pp. 687-701, Nov 9 2012, doi: 10.1016/j.jmb.2012.08.021.
- [158] D. Spakman, G. A. King, E. J. G. Peterman, and G. J. L. Wuite, "Constructing arrays of nucleosome positioning sequences using Gibson Assembly for single-molecule studies," *Sci Rep*, vol. 10, no. 1, p. 9903, Jun 18 2020, doi: 10.1038/s41598-020-66259-4.
- [159] M. J. McCauley *et al.*, "Human FACT subunits coordinate to catalyze both disassembly and reassembly of nucleosomes," (in eng), *Cell Rep*, vol. 41, no. 13, p. 111858, Dec 27 2022, doi: 10.1016/j.celrep.2022.111858.
- [160] C. Claudet, D. Angelov, P. Bouvet, S. Dimitrov, and J. Bednar, "Histone octamer instability under single molecule experiment conditions," *J Biol Chem*, vol. 280, no. 20, pp. 19958-65, May 20 2005, doi: 10.1074/jbc.M500121200.
- [161] F. T. Chien and J. van Noort, "10 years of tension on chromatin: results from single molecule force spectroscopy," *Curr Pharm Biotechnol*, vol. 10, no. 5, pp. 474-85, Aug 2009, doi: 10.2174/138920109788922128.

- [162] A. Kaczmarczyk, T. B. Brouwer, C. Pham, N. H. Dekker, and J. van Noort, "Probing Chromatin Structure with Magnetic Tweezers," *Methods Mol Biol*, vol. 1814, pp. 297-323, 2018, doi: 10.1007/978-1-4939-8591-3_18.
- [163] B. Brower-Toland, D. A. Wacker, R. M. Fulbright, J. T. Lis, W. L. Kraus, and M. D. Wang, "Specific contributions of histone tails and their acetylation to the mechanical stability of nucleosomes," *J Mol Biol*, vol. 346, no. 1, pp. 135-46, Feb 11 2005, doi: 10.1016/j.jmb.2004.11.056.
- [164] M. Y. Sheinin, M. Li, M. Soltani, K. Luger, and M. D. Wang, "Torque modulates nucleosome stability and facilitates H2A/H2B dimer loss," *Nat Commun*, vol. 4, p. 2579, 2013, doi: 10.1038/ncomms3579.
- [165] S. H. Kim, R. Vlijm, J. van der Torre, Y. Dalal, and C. Dekker, "CENP-A and H3 Nucleosomes Display a Similar Stability to Force-Mediated Disassembly," *PLoS One*, vol. 11, no. 11, p. e0165078, 2016, doi: 10.1371/journal.pone.0165078.
- [166] A. Bancaud *et al.*, "Structural plasticity of single chromatin fibers revealed by torsional manipulation," *Nat Struct Mol Biol*, vol. 13, no. 5, pp. 444-50, May 2006, doi: 10.1038/nsmb1087.
- [167] S. F. Konrad, W. Vanderlinden, and J. Lipfert, "Quantifying epigenetic modulation of nucleosome breathing by high-throughput AFM imaging," *Biophys J*, vol. 121, no. 5, pp. 841-851, Mar 1 2022, doi: 10.1016/j.bpj.2022.01.014.
- [168] L. Chang and S. Takada, "Histone acetylation dependent energy landscapes in tri-nucleosome revealed by residue-resolved molecular simulations," *Sci Rep*, vol. 6, p. 34441, Oct 4 2016, doi: 10.1038/srep34441.
- [169] J. J. Funke, P. Ketterer, C. Lieleg, S. Schunter, P. Korber, and H. Dietz, "Uncovering the forces between nucleosomes using DNA origami," *Sci Adv*, vol. 2, no. 11, p. e1600974, Nov 2016, doi: 10.1126/sciadv.1600974.
- [170] R. Strick, P. L. Strissel, K. Gavrilov, and R. Levi-Setti, "Cation-chromatin binding as shown by ion microscopy is essential for the structural integrity of chromosomes," *J Cell Biol*, vol. 155, no. 6, pp. 899-910, Dec 10 2001, doi: 10.1083/jcb.200105026.
- [171] F. Thoma, T. Koller, and A. Klug, "Involvement of histone H1 in the organization of the nucleosome and of the salt-dependent superstructures of chromatin," *J Cell Biol*, vol. 83, no. 2 Pt 1, pp. 403-27, Nov 1979, doi: 10.1083/jcb.83.2.403.
- [172] A. Allahverdi, Q. Chen, N. Korolev, and L. Nordenskiöld, "Chromatin compaction under mixed salt conditions: opposite effects of sodium and potassium ions on nucleosome array folding," *Sci Rep*, vol. 5, p. 8512, Feb 17 2015, doi: 10.1038/srep08512.
- [173] T. Ohyama, "New Aspects of Magnesium Function: A Key Regulator in Nucleosome Self-Assembly, Chromatin Folding and Phase Separation," *Int J Mol Sci*, vol. 20, no. 17, Aug 29 2019, doi: 10.3390/ijms20174232.
- [174] P. M. Schwarz, A. Felthäuser, T. M. Fletcher, and J. C. Hansen, "Reversible oligonucleosome self-association: dependence on divalent cations and core histone tail domains," *Biochemistry*, vol. 35, no. 13, pp. 4009-15, Apr 2 1996, doi: 10.1021/bi9525684.
- [175] M. Gebala, S. L. Johnson, G. J. Narlikar, and D. Herschlag, "Ion counting demonstrates a high electrostatic field generated by the nucleosome," *Elife*, vol. 8, Jun 11 2019, doi: 10.7554/eLife.44993.
- [176] A. Dwiranti *et al.*, "The effect of magnesium ions on chromosome structure as observed by helium ion microscopy," *Microsc Microanal*, vol. 20, no. 1, pp. 184-8, Feb 2014, doi: 10.1017/S1431927613013792.
- [177] P. Vizjak *et al.*, "ISWI catalyzes nucleosome sliding in condensed nucleosome arrays," *bioRxiv*, Dec 4 2023, doi: 10.1101/2023.12.04.569516.

- [178] M. Engelhardt, "Condensation of chromatin in situ by cation-dependent charge shielding and aggregation," *Biochem Biophys Res Commun*, vol. 324, no. 4, pp. 1210-4, Nov 26 2004, doi: 10.1016/j.bbrc.2004.09.175.
- [179] M. M. van Oene *et al.*, "Quantifying the Precision of Single-Molecule Torque and Twist Measurements Using Allan Variance," *Biophys J*, vol. 114, no. 8, pp. 1970-1979, Apr 24 2018, doi: 10.1016/j.bpj.2018.02.039.
- [180] W. P. Wong and K. Halvorsen, "The effect of integration time on fluctuation measurements: calibrating an optical trap in the presence of motion blur," *Opt Express*, vol. 14, no. 25, pp. 12517-31, Dec 11 2006, doi: 10.1364/oe.14.012517.
- [181] C. M. Van Vliet and P. H. Handel, "A new transform theorem for stochastic processes with special application to counting statistics," *Physica A: Statistical Mechanics and its Applications*, vol. 113, no. 1, pp. 261-276, 1982/07/01/ 1982, doi: [https://doi.org/10.1016/0378-4371\(82\)90019-X](https://doi.org/10.1016/0378-4371(82)90019-X).
- [182] N. Krietenstein, C. J. Wippo, C. Lieleg, and P. Korber, "Genome-wide in vitro reconstitution of yeast chromatin with in vivo-like nucleosome positioning," *Methods Enzymol*, vol. 513, pp. 205-32, 2012, doi: 10.1016/B978-0-12-391938-0.00009-4.
- [183] S. F. Konrad, W. Vanderlinden, and J. Lipfert, "A High-throughput Pipeline to Determine DNA and Nucleosome Conformations by AFM Imaging," *Bio Protoc*, vol. 11, no. 19, p. e4180, Oct 5 2021, doi: 10.21769/BioProtoc.4180.
- [184] M. Bussiek, N. Mucke, and J. Langowski, "Polylysine-coated mica can be used to observe systematic changes in the supercoiled DNA conformation by scanning force microscopy in solution," *Nucleic Acids Res*, vol. 31, no. 22, p. e137, Nov 15 2003, doi: 10.1093/nar/gng137.
- [185] W. Vanderlinden, J. Lipfert, J. Demeulemeester, Z. Debysen, and S. De Feyter, "Structure, mechanics, and binding mode heterogeneity of LEDGF/p75-DNA nucleoprotein complexes revealed by scanning force microscopy," *Nanoscale*, vol. 6, no. 9, pp. 4611-9, May 7 2014, doi: 10.1039/c4nr00022f.
- [186] S. Gruber, A. Löf, S. M. Sedlak, M. Benoit, H. E. Gaub, and J. Lipfert, "Designed anchoring geometries determine lifetimes of biotin–streptavidin bonds under constant load and enable ultra-stable coupling," *Nanoscale*, 10.1039/D0NR03665J vol. 12, no. 41, pp. 21131-21137, 2020, doi: 10.1039/D0NR03665J.
- [187] T. S. Lisitsa *et al.*, "The kinetics of fluorescent DNA labeling using PCR with different Taq polymerases depends on the chemical structures of modified nucleotides," *Biophys J*, vol. 62, no. 3, pp. 366-372, 2017/05/01 2017, doi: 10.1134/S0006350917030095.
- [188] S. Basu, A. Finke, L. Vera, M. Wang, and V. Olieric, "Making routine native SAD a reality: lessons from beamline X06DA at the Swiss Light Source," *Acta Crystallographica Section D*, vol. 75, no. 3, pp. 262-271, 2019, doi: doi:10.1107/S2059798319003103.
- [189] X. J. Janssen, J. Lipfert, T. Jäger, R. Daudey, J. Beekman, and N. H. Dekker, "Electromagnetic torque tweezers: a versatile approach for measurement of single-molecule twist and torque," *Nano Lett*, vol. 12, no. 7, pp. 3634-9, Jul 11 2012, doi: 10.1021/nl301330h.
- [190] J. Lipfert, M. Wiggin, J. W. Kerssemakers, F. Pedaci, and N. H. Dekker, "Freely orbiting magnetic tweezers to directly monitor changes in the twist of nucleic acids," *Nat Commun*, vol. 2, p. 439, Aug 23 2011, doi: 10.1038/ncomms1450.
- [191] J. Lipfert, M. Lee, O. Ordu, J. W. Kerssemakers, and N. H. Dekker, "Magnetic tweezers for the measurement of twist and torque," *J Vis Exp*, no. 87, May 19 2014, doi: 10.3791/51503.
- [192] J. Lipfert, S. Klijnhout, and N. H. Dekker, "Torsional sensing of small-molecule binding using magnetic tweezers," *Nucleic Acids Res*, vol. 38, no. 20, pp. 7122-32, Nov 2010, doi: 10.1093/nar/gkq598.

- [193] M. Simon *et al.*, "Histone fold modifications control nucleosome unwrapping and disassembly," *Proc Natl Acad Sci U S A*, vol. 108, no. 31, pp. 12711-6, Aug 2 2011, doi: 10.1073/pnas.1106264108.
- [194] S. E. Farr, E. J. Woods, J. A. Joseph, A. Garaizar, and R. Collepardo-Guevara, "Nucleosome plasticity is a critical element of chromatin liquid-liquid phase separation and multivalent nucleosome interactions," *Nat Commun*, vol. 12, no. 1, p. 2883, May 17 2021, doi: 10.1038/s41467-021-23090-3.
- [195] A. Sharda and T. C. Humphrey, "The role of histone H3K36me3 writers, readers and erasers in maintaining genome stability," *DNA Repair (Amst)*, vol. 119, p. 103407, Nov 2022, doi: 10.1016/j.dnarep.2022.103407.
- [196] W. Tian *et al.*, "The HRP3 PWWP domain recognizes the minor groove of double-stranded DNA and recruits HRP3 to chromatin," *Nucleic Acids Res*, vol. 47, no. 10, pp. 5436-5448, Jun 4 2019, doi: 10.1093/nar/gkz294.
- [197] J. Fei *et al.*, "NDF, a nucleosome-destabilizing factor that facilitates transcription through nucleosomes," (in eng), *Genes Dev*, vol. 32, no. 9-10, pp. 682-694, May 1 2018, doi: 10.1101/gad.313973.118.
- [198] G. B. Rona, E. C. A. Eleutherio, and A. S. Pinheiro, "PWWP domains and their modes of sensing DNA and histone methylated lysines," *Biophys Rev*, vol. 8, no. 1, pp. 63-74, Mar 2016, doi: 10.1007/s12551-015-0190-6.
- [199] R. T. Simpson, "Structure of chromatin containing extensively acetylated H3 and H4," *Cell*, vol. 13, no. 4, pp. 691-9, Apr 1978, doi: 10.1016/0092-8674(78)90219-2.
- [200] N. Gilbert, S. Boyle, H. Fiegler, K. Woodfine, N. P. Carter, and W. A. Bickmore, "Chromatin architecture of the human genome: gene-rich domains are enriched in open chromatin fibers," *Cell*, vol. 118, no. 5, pp. 555-66, Sep 3 2004, doi: 10.1016/j.cell.2004.08.011.
- [201] V. R. Lobbia, M. C. Trueba Sanchez, and H. van Ingen, "Beyond the Nucleosome: Nucleosome-Protein Interactions and Higher Order Chromatin Structure," *J Mol Biol*, vol. 433, no. 6, p. 166827, Mar 19 2021, doi: 10.1016/j.jmb.2021.166827.
- [202] M. Shvedunova and A. Akhtar, "Modulation of cellular processes by histone and non-histone protein acetylation," *Nat Rev Mol Cell Biol*, vol. 23, no. 5, pp. 329-349, May 2022, doi: 10.1038/s41580-021-00441-y.
- [203] B. Xiao, B. S. Freedman, K. E. Miller, R. Heald, and J. F. Marko, "Histone H1 compacts DNA under force and during chromatin assembly," *Mol Biol Cell*, vol. 23, no. 24, pp. 4864-71, Dec 2012, doi: 10.1091/mbc.E12-07-0518.
- [204] W. Li *et al.*, "FACT Remodels the Tetranucleosomal Unit of Chromatin Fibers for Gene Transcription," *Mol Cell*, vol. 64, no. 1, pp. 120-133, Oct 6 2016, doi: 10.1016/j.molcel.2016.08.024.
- [205] M. Andres, D. Garcia-Gomis, I. Ponte, P. Suau, and A. Roque, "Histone H1 Post-Translational Modifications: Update and Future Perspectives," *Int J Mol Sci*, vol. 21, no. 16, Aug 18 2020, doi: 10.3390/ijms21165941.
- [206] L. Millan-Arino, A. Izquierdo-Bouldstridge, and A. Jordan, "Specificities and genomic distribution of somatic mammalian histone H1 subtypes," *Biochim Biophys Acta*, vol. 1859, no. 3, pp. 510-9, Mar 2016, doi: 10.1016/j.bbagr.2015.10.013.
- [207] J. P. Th'ng, R. Sung, M. Ye, and M. J. Hendzel, "H1 family histones in the nucleus. Control of binding and localization by the C-terminal domain," *J Biol Chem*, vol. 280, no. 30, pp. 27809-14, Jul 29 2005, doi: 10.1074/jbc.M501627200.

- [208] H. Wang, L. Farnung, C. Dienemann, and P. Cramer, "Structure of H3K36-methylated nucleosome-PWWP complex reveals multivalent cross-gyre binding," *Nat Struct Mol Biol*, vol. 27, no. 1, pp. 8-13, Jan 2020, doi: 10.1038/s41594-019-0345-4.
- [209] J. Lipfert, M. M. van Oene, M. Lee, F. Pedaci, and N. H. Dekker, "Torque spectroscopy for the study of rotary motion in biological systems," *Chem Rev*, vol. 115, no. 3, pp. 1449-74, Feb 11 2015, doi: 10.1021/cr500119k.
- [210] Z. Bryant, F. C. Oberstrass, and A. Basu, "Recent developments in single-molecule DNA mechanics," *Curr Opin Struct Biol*, vol. 22, no. 3, pp. 304-12, Jun 2012, doi: 10.1016/j.sbi.2012.04.007.
- [211] Z. Yu *et al.*, "A force calibration standard for magnetic tweezers," *Rev Sci Instrum*, vol. 85, no. 12, p. 123114, Dec 2014, doi: 10.1063/1.4904148.
- [212] J. P. Cnossen, D. Dulin, and N. H. Dekker, "An optimized software framework for real-time, high-throughput tracking of spherical beads," *Rev Sci Instrum*, vol. 85, no. 10, p. 103712, Oct 2014, doi: 10.1063/1.4898178.
- [213] I. De Vlamincq, T. Henighan, M. T. van Loenhout, D. R. Burnham, and C. Dekker, "Magnetic forces and DNA mechanics in multiplexed magnetic tweezers," *PLoS One*, vol. 7, no. 8, p. e41432, 2012, doi: 10.1371/journal.pone.0041432.
- [214] D. Baretino, M. Feigenbutz, R. Valcarcel, and H. G. Stunnenberg, "Improved method for PCR-mediated site-directed mutagenesis," *Nucleic Acids Res*, vol. 22, no. 3, pp. 541-2, Feb 11 1994, doi: 10.1093/nar/22.3.541.
- [215] J. Brons-Poulsen, J. Nohr, and L. K. Larsen, "Megaprimer method for polymerase chain reaction-mediated generation of specific mutations in DNA," *Methods Mol Biol*, vol. 182, pp. 71-6, 2002, doi: 10.1385/1-59259-194-9:071.
- [216] J. Brons-Poulsen, N. E. Petersen, M. Horder, and K. Kristiansen, "An improved PCR-based method for site directed mutagenesis using megaprimers," *Mol Cell Probes*, vol. 12, no. 6, pp. 345-8, Dec 1998, doi: 10.1006/mcpr.1998.0187.

List of publications

Publications included in this work

- **Yi-Yun Lin**, Tine Brouns, Pauline J. Kolbeck, Willem Vanderlinden, and Jan Lipfert. "High-yield ligation-free assembly of DNA constructs with nucleosome positioning sequence repeats for single-molecule manipulation assays." *J Biol Chem*, vol. 299, no. 7, p. 104874, Jul 2023, doi: [10.1016/j.jbc.2023.104874](https://doi.org/10.1016/j.jbc.2023.104874).
- **Yi-Yun Lin**, Peter Müller, Evdoxia Karagianni, Willem Vanderlinden, and Jan Lipfert. "Epigenetic histone modifications H3K36me3 and H4K5/8/12/16ac induce open polynucleosome conformations via different mechanisms." *Under review at Journal of Molecular Biology*, Preprint at bioRxiv: <https://doi.org/10.1101/2024.02.19.580980>

Publications not included in this work

- Sergio Cruz-León, Willem Vanderlinden, Peter Müller, Tobias Forster, Georgina Staudt, **Yi-Yun Lin**, Jan Lipfert, and Nadine Schwierz. "Twisting DNA by salt." *Nucleic Acids Research*, Volume 50, Issue 10, 10 June 2022, Pages 5726–5738, <https://doi.org/10.1093/nar/gkac445>
- **Yi-Yun Lin**, Min-Hsuan Li, Yen-Chan Chang, Peng-Yu Fu, Ryosuke L. Ohniwa, Hung-Wen Li, and Jing-Jer Lin. "Dynamic DNA Shortening by Telomere-Binding Protein Cdc13." *Journal of the American Chemical Society* 2021 143 (15), 5815-5825, <https://doi.org/10.1021/jacs.1c00820>

Acknowledgements

The study was conducted also with the following contributions from other scientists. I want to express my gratitude towards: **Prof. Jan Lipfert** contributed the visualization and analysis depicted in Figure 2.3. **Dr. Willem Vanderlinden** contributed visualization and analysis depicted in Supplementary Figure 5.13. **Peter Müller** carried out, analyzed, investigated, and visualized AFM measurements depicted in Figure 2.7, Figure 2.8, and Supplementary Figures 5.11, 5.12, and 5.14. **Evdoxia Karagianni** performed and analyzed MT experiment on DNA samples depicted in Figure 2.5. **Pauline Kolbeck** assisted “Megaprimer project” and carried out, analyzed, and visualized MT measurements depicted in Supplementary Figure 5.7. **Tine Brouns** helped conceptualize “megaprimer” protocol as well.

Specifically, I want to thank **Jan Lipfert** for giving me a chance to be a doctoral candidate. Jan supports research, supervision, and project administration, and teaches me academic writing. After we moved to the Netherlands, Jan helped us a lot to settle down in a new place and help to build a new lab. Jan is always approachable and always respects our opinions. Besides, Jan always brings positive energy into the office. I enjoy the good vibe he creates in the office and all the fun conversations over lunch break, coffee break, borrel, or group outings.

Similarly, I want to thank **Willem Vanderlinden** who very much helped me conceptualize my project, including supervision and project administration, and provided useful and insightful discussion about science. Thanks for providing useful suggestions while I met the bottleneck during research. And thanks for imparting knowledge, lab skills, and data analysis methods to me.

Thanks to all technicians - **Thomas Nicolaus, Dave van den Heuvel, Relinde van Dijk-Moes, and Elleke van Harten** for laboratory assistance.

Thanks to **Friedrich Förster, Louris Feitsma, Joke Granneman, Mariska Gröllers-Mulderij**, and the entire Structural Biochemistry group at Utrecht University for useful discussion and laboratory use.

Thanks to **Lori van de Cauter, Steven De Feyter, Sebastian Konrad, Tine Brouns, Philipp Kober, and Felix Müller-Planitz** for useful discussions.

Thanks to **Stefanie D. Pritzl, Caroline Körösy, Ivo Vermaire, Pauline Kolbeck, and Diogo Saraiva** for support with measurements.

Thanks to **Hermann Gaub** for the great working environment, and also **Soft Condensed Matter And Biophysics** group at Utrecht University for organizing many fun activities and welcoming me. I enjoy every time lunch break, coffee break, borrel, and group outings with people here.

Also, during my time in Jan’s group, my gratitude goes to my fellow and other people who provided useful discussions and measurement support for my research, and emotional support as well!!

Adina Hausch, Aidin Lak, Alptug Ulugöl, Barbara Müller, Damla Tetiker, Enrico Skoruppa, Ellis Durner, Evdoxia Karagianni, Gerhard Blab, Jan Boltersdorf, Katherine Erlich, Koen Storm, Laura Krumm, Leo Schendel, Lisa Trans, Louis de Gaste, Lukas Milles, Margherita Gallano, Magnus Bauer, Nina Beier, Peter Müller, Samuel Stubhan, Sophia Gruber, Sylvia Kreuzer, Sabine Hohenester, Tine Brouns, Thorben Cordes, Yoldaş Cinemre and any other I may have overlooked.

Curriculum Vitae – Lin, Yi-Yun

EDUCATION

2015/09 -2017/06	National Taiwan University, College of Medicine (NTUCM) <i>Master of Science in Institute of Biochemistry and Molecular Biology</i> Total GPA: 4.17/4.3 Rank: 1/17
2011/09 -2015/06	National Taiwan University, College of BioResources and Agriculture (NTU) <i>Bachelor of Science in Department of Agriculture Chemistry</i> Total GPA: 3.74/4.3 Rank: 9/40

RESEARCH EXPERIENCES

2022/07 -2024/11	Doctoral Program <i>Prof. Jan Lipfert, Department of Physics, Utrecht University, The Netherlands</i>
2018/10 -2022/07	Doctoral Program <i>Prof. Jan Lipfert, Department of Physics, LMU Munich</i>
	Nucleosome Dynamics In Magnetic Tweezers
2017/09 -2018/08	Research Assistant, <i>Prof. Jing-Jer Lin's Lab, Institute of Biochemistry and Molecular Biology, NTUCM</i>
	Applying single-molecule tethered-particle motion (TPM) to investigate Cdc13-dependent capping function on telomere
2015/07 -2017/07	M.S. Program, <i>Prof. Jing-Jer Lin's Lab, Institute of Biochemistry and Molecular Biology, NTUCM</i>
	Investigate the regulatory mechanism of telomere binding proteins on telomerase
2014/01 -2015/05	Undergraduate Research, <i>Prof. Chun-Hua Hsu's Lab, Department of Agriculture Chemistry, NTU</i>
	Structural and Functional Studies of Caffeoyl-CoA-O-Methyltransferase 3 from <i>Arabidopsis thaliana</i>